EXPERIMENTAL AND NUMERICAL STUDY OF SHEAR LOCALIZATION AS AN INITIATION MECHANISM IN ENERGETIC SOLIDS

A Thesis

Submitted to the Graduate School
of the University of Notre Dame
in Partial Fulfillment of the Requirements
for the Degree of

Master of Science
in Mechanical Engineering

by

Richard Joseph Caspar, B.S.

Joseph M. Powers, Director

James J. Mason, Director

Department of Aerospace and Mechanical Engineering
Notre Dame, Indiana
July, 1996

EXPERIMENTAL AND NUMERICAL STUDY OF SHEAR LOCALIZATION AS AN INITIATION MECHANISM IN ENERGETIC SOLIDS

Abstract

by

Richard Joseph Caspar

This thesis considers the behavior of energetic and inert solids subjected to simple shear loading. Data from a torsional split-Hopkinson bar, built for this study, was reduced to determine shear stress and shear strain characteristics of these materials. These results were then used to calibrate a constitutive law for stress, including the effects of strain and strain rate hardening and thermal softening. A one dimensional finite difference study of shear localization was performed, modeling the effects of thermal conductivity, viscoplastic heating and Arrhenius kinetics. Results revealed shear localization and reaction initiation in the explosives simulated. Experimental failure of the inert solids, however, occurred at shear strains significantly lower than those predicted by theory. This has been attributed to the presence of failure mechanisms other than shear localization, which were not included in the theoretical model. It is concluded that the tested energetic materials are not expected to shear localize or initiate under the conditions considered.

TABLE OF CONTENTS

LIST OF TABLES

LIST OF FIGURES

LIST OF SYMBOLS

$\bullet$	A generic quantity used in this list
$d\bullet$	Differential quantity
$\Sigma\bullet$	Symbol indicating a summation
$\Delta\bullet$	Symbol denoting a change in a quantity
$\bullet'$	Accent denoting differentiation with respect to a specific variable
$\bullet^*$	Superscript denoting nondimensional variables
$\hat{\bullet}$	Accent denoting nondimensional parameters
$\bullet_i$	Subscript denoting the i^{th} spatially discretized quantity
$\bullet_r$	Subscript denoting radial direction
$\bullet_s$	Subscript denoting the specimen
$\bullet_z$	Subscript denoting axial direction
$\bullet_I$	Subscript denoting the incident pulse
$\bullet_A$, $\bullet_B$	Subscripts denoting unreacted and reacted material, respectively
$\bullet_R$	Subscript denoting the reflected pulse
$\bullet_T$	Subscript denoting the transmitted pulse
$\bullet_\theta$	Subscript denoting the circumferential direction

c	Elastic wave speed
$\hat{c}$	Ratio of specific heats of the reacted and unreacted material
c_1	Specific heat of the incident bar, for dissimilar bars
c_2	Specific heat of the transmission bar, for dissimilar bars
e	Internal energy
e°	Energy of formation
f, g	Arbitrary functions in D'Alembert's solution
$\hat{h}$	Maximum nondimensional decrease in specimen wall thickness
h_p	Maximum decrease in the specimen wall thickness

k	Thermal conductivity
m	Mass
n	Constant integer in Test Case 3
q_z	Heat flux in the axial direction
r	Radius
r_0	Outer radius of a bar
r_1	Outer radius of the incident bar, for dissimilar bars
r_2	Outer radius of the transmission bar, for dissimilar bars
r_{av}	Average radius of a thin walled tube
s	Constant in Test Case 2
t	Time
t^*	Nondimensional time
$\hat{t}$	Nondimensional rise time
t^*_{loc}	Nondimensional localization onset time
t^*_{react}	Nondimensional reaction initiation time
t_1	Rise time over which the velocity is ramped to v_1
$\bar{t}$	Dummy variable for integration
u^*	Nondimensional circumferential displacement
u_θ	Circumferential displacement
v^*	Nondimensional circumferential velocity
v_e^{*i}	Exact solution of a specified quantity in computing the L_2 norm
v_n^{*i}	Numerically determined solution of a specified quantity in computing the L_2 norm
v_θ	Circumferential velocity
v_0	Initial velocity parameter
v_1	Constant velocity to which v_θ is ramped in the numerical simulations
w	Wall thickness of the specimen
w^*	Nondimensional wall thickness of the specimen
w_0	Wall thickness at the edge of the specimen
$x,\ y$	Cartesian coordinates

$\tilde{y}$	Vector of unknowns
z	Axial position variable
A	Area
$\bar{A}$, $\bar{B}$, $\bar{C}$	Matrix expressions
C_1, C_2	Constants in Test Case 2
D	Diameter of incident and transmitted bars
D_s	Mean diameter of the specimen
E	Activation energy
$\hat{E}$	Nondimensional activation energy
E_0	Output voltage in a Wheatstone bridge
Ec	Eckert number
F	Gage factor
$\tilde{F}$	Solution vector
G	Elastic shear modulus
G_a	Gain of an amplifier
I	Mass moment of inertia
J	Polar moment of inertia
J_1	Polar moment of inertia of the incident bar, for dissimilar bars
J_2	Polar moment of inertia of the transmission bar, for dissimilar bars
J_{rod}	Polar moment of inertia of a rod
J_{tube}	Polar moment of inertia of a thin walled tube
L	Length of a stored pulse
L_2	Norm used to determine convergence of the numerical method
L_s	Length of the specimen
M	Moment
N	Number of discretized spatial increments
N_g	Number of active strain gages in a Wheatstone bridge
Pe	Peclet number

Q	Heat of reaction
$\hat{Q}$	Nondimensional heat of reaction
R	Universal gas constant
$R_1,\ R_2,\ R_3,\ R_4$	Electrical resistances of the corresponding resistors in a Wheatstone bridge
T	Temperature
T^*	Nondimensional temperature
T_0	Initial temperature
T_1	Torque at the specimen/incident bar interface
T_2	Torque at the specimen/transmission bar interface
T_z	Torque in the axial direction
V	Excitation voltage in a Wheatstone bridge
Z	Kinetic rate constant
$\hat{Z}$	Nondimensional kinetic rate constant

α	Stress constant
$\hat{\alpha}$	Nondimensional stress constant
γ	Shear strain
γ_0	Shear strain on the surface of the bar
$\dot{\gamma}$	Shear strain rate
$\dot{\gamma}_o$	A known solution at a given point
ϵ	Nondimensional initial velocity
ζ	Eigenvalues of the model equations
η	Strain hardening exponent
κ	Ratio of the impedance in the Wheatstone bridge resistors
λ	Reaction progress variable
μ	Strain rate hardening exponent
ν	Thermal softening exponent
ρ	Density

ρ_1	Density of the incident bar, for dissimilar bars
ρ_2	Density of the transmission bar, for dissimilar bars
τ	Shear stress
τ_0	Shear stress on the surface of a bar
ϕ	Angle of rotation of a bar
ϕ_1	Angle of rotation of the specimen/incident bar interface
ϕ_2	Angle of rotation of the specimen/transmission bar interface
ω	Constant in Test Case 3
Φ	Term representing the effects of thermal softening
Ψ	Term representing the combined effects of strain and strain rate hardening

ACKNOWLEDGMENTS

I would like to acknowledge the Munitions Division of the Armament Directorate of Wright Laboratories, Eglin Air Force Base, for providing support for my research through the Air Force Office of Scientific Research, Research and Development Laboratories, in the form of a summer internship and extension grant. In addition, I would like to acknowledge the Department of Aerospace and Mechanical Engineering at the University of Notre Dame for its various assistantships.

I would also like to acknowledge my advisors, Dr. Joseph M. Powers and Dr. James J. Mason, for their guidance and instruction throughout my graduate career. I would like to thank Dr. Mason for teaching me through his own example that success comes from a diligent pursuit of one's professional goals, coupled with wit and humor, and necessarily balanced by the loving care and support given to and received by friends and family. I would like to thank Dr. Powers, whose unwavering drive to produce quality research has instilled within me a drive to achieve quality in all respects of my life. Also, for holding his standard high and keeping me striving to go the extra mile. Furthermore, I would like to acknowledge Dr. Edmundo Corona and Dr. Samuel Paolucci for taking the time to be on my masters committee.

I would like to acknowledge Dr. Joe Foster, Mr. Russ Klug, Mr. Thad Wallace, Mr. David Wagnon, Mr. Art Spencer, Mr. Gregg Glynn and all the people at the Advanced Warheads Evaluation Facility (AWEF) and the High Explosives Research and

Development Facility (HERD) at Eglin Air Force Base for their early and continued support and encouragement of my research efforts.

I would like to thank Kevin Peters for his time and efforts at correcting the numerous problems which I encountered. I would also like to thank Bruce Hardy, Mark Stelmac, and the other occasional members of the Tuesday night social club for providing the atmosphere to relax and blow off steam. I would also like to thank Keith Gonthier and Andy Smith for the conversations, advice and encouragement. In addition, many thanks to all my friends at Breen-Phillips Hall for their friendship and keeping me sane and active outside of my studies.

I would also like to thank my parents for instilling within me the desire to continually further my education, and for their unending love, support and advice in helping me conquer life's many challenges. Without their friendship, I would not have been able to achieve my many successes.

Lastly, I would like to thank Emily, for sticking with me through my studies and helping me to keep perspective. For the nourishment that her light and love has brought me, I constantly thank God.

CHAPTER 1

INTRODUCTION

This thesis will address, experimentally and theoretically, the behavior of various metals, solid explosive simulants, and solid explosives subject to simple shear loading. In addition, this thesis will consider reaction initiation in the energetic materials as a result of a mechanism known as shear localization or shear banding. In this chapter, a description and review of the pertinent work is given. Two softening mechanisms which lead to shear banding will be discussed: viscoplastic thermal softening and void nucleation and growth. Pertinent work performed in the study of shear localization in explosives is also discussed.

1.1 Overview

The motivation for this thesis lies in the development of insensitive munitions, which are resistant to accidental detonation. Insensitive munitions are desired for many reasons. First, insensitivity lessens safety risks in the storage and handling of these devices. In addition, it is desired to prevent sympathetic detonation, in which the detonation of one device causes others to detonate. Another motivation for this thesis comes in the field of deep earth penetrators. These devices are designed to travel through tens of feet of rock, concrete and earth; hence, a significant amount

of deformation is inherent within the penetrator. It is thus desired to design these munitions to be insensitive to this deformation.

In order to develop insensitive munitions, it is necessary to more fully understand the behavior of explosives. As full scale tests on explosives are often costly and time consuming, it is desirable to develop computer models and simple bench-top experiments which predict the deformation and initiation of these materials. There are numerous finite-element packages, such as EPIC and ABAQUS, which have been designed to predict material deformation. To date, limited data exists to develop constitutive models for explosives to use as input into these packages. One of the foci of this study is thus to determine the material properties of various explosive simulants and explosives. These properties are determined through the use of an experimental apparatus known as the torsional split Hopkinson bar (TSHB), which was built by this author. This apparatus is capable of deforming materials in simple shear at shear strain rates of 10^2 to 10^4 s^{-1}. Results obtained using this apparatus reveal the shear stress-shear strain properties for the tested material. In addition, photographs of the deformation are taken with an ultra-high speed camera, capable of framing at a rate of 2 million frames per second, to observe the failure mechanism.

The TSHB has previously been used to determine material characteristics for metals, in which failure often occurs due to a mechanism known as shear localization. Shear localization is also known to be one of the initiation mechanisms in solid explosives [Field *et al.*, 1982], also, it is one of the least understood mechanisms. Much of the studies on initiation, however, have been performed under shock and impact conditions, in which the stresses within the explosives are much greater than the

yield stress, thus making the effect of the strength of the materials insignificant [Frey (1981), Boyle *et al.* (1989), Chou *et al.* (1991)]. As a result, little is known about the sensitivity of explosives under lower stress deformations, where the strength of the material becomes significant. In deep earth penetrators, it is surmised that explosives undergo significant deformation at high strain rates and relatively low stresses (on the order of the yield stress of the material) and low pressures, in which the material strength is thought to affect the deformation of explosives. One of the detonation mechanism expected to dominate under such conditions is shear localization. An additional goal of the experimental tests is thus an attempt at observing shear localization in explosives deforming in simple shear.

Figure 1.1 describes the mechanism of shear localization. In Figure 1.1a, a portion of an undeformed material is sketched with thin lines inscribed on its surface. When this material is sheared, the scribe lines begin to slant at a uniform angle, as seen in Figure 1.1b. This form of deformation is known as homogeneous deformation.

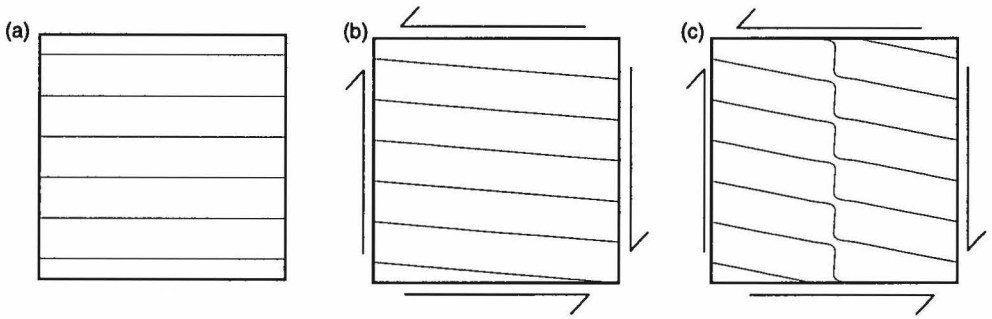

Figure 1.1: Schematic of the shear localization process. (a) Undeformed grid lines, (b) Homogeneous deformation, (c) Shear localization

Increased straining into the plastic range results in hardening of the material. In addition, if there is a geometric discontinuity, void, scratch or some other material

weakness, straining near that discontinuity will occur at a higher strain rate, which also hardens the material. This increased local deformation, however, also causes plastic heating of the material. If the straining occurs at high strain rates (typically greater than $10^2\ s^{-1}$), there is not enough time for the generated heat to be conducted away. The local increase in heat results in thermal softening of the material. If this process dominates over the hardening due to strain and strain rate effects, the material strength decreases. As a result of this local softening of the material, deformation is localized into a thin planar region, as depicted by the scribe line deformation of Figure 1.1c. This final process is known as shear localization or shear banding.

In addition to the experimental tests that were performed in this thesis, a numerical model was developed to predict the deformation of a material in simple shear. The governing equations of conservation of momentum and energy are used in this model. In the discussion of shear localization in the following section, two softening mechanisms will been discussed which are known to lead to shear banding: thermal softening and microvoid nucleation and growth. In this thesis, a constitutive law for the shear stress is utilized, in which the effects of strain and strain rate hardening, and thermal softening are included; microvoid nucleation is neglected. Since it has been shown that the choice of a particular constitutive law does not significantly effect the results [Wright (1987), and Batra and Kim (1991)], a simplified power law will be implemented. Also included in the model is the effect of thermal conductivity due to its importance in achieving accurate temperature predictions [Batra and Kim, 1991]. Finally, exothermic reaction is modeled by an Arrhenius kinetic law. Despite results attesting to the fact that localization is a multidimensional process [Marchand and

Duffy (1988) and Giovanola (1988 a,b)], a one dimensional model will be developed, since this model is sufficient in yielding important information about the shear band temperature profile in solid explosives. The pertinence of these effects is discussed in the following sections.

The novelty of this thesis first lies in the testing of explosive simulants with the torsional split-Hopkinson bar and the determination of their shear stress and shear strain characteristics. Also, the implementation of Arrhenius kinetics in the study of simple shear deformation of explosives is new. In addition, most researchers studying simple shear deformation have used a finite-element formulation for solving the governing equations. In this thesis, the equations are solved by a finite-difference method.

1.2 General Reviews

This section presents a brief review of works on the high strain rate behavior of materials as well as the initiation mechanisms in solid explosives. A compilation of works on shock wave and high strain rate phenomena in materials is presented by Meyers *et al.* (1992). Meyers (1994) also discusses these dynamic events in materials. These books discuss various failure mechanisms occurring at high strain rate in materials, including shear localization. In addition, works studying high strain rate effects in explosives are discussed.

Bowden and Yoffe (1985) performed an extensive review of experimental works on explosive mechanics in order to categorize the various mechanisms of initiation in solid explosives. They conclude that initiation could occur by the adiabatic compression

of small entrapped bubbles of gas; the formation of hot spots on confining surfaces, extraneous grit particles and intercrystalline friction of the explosive particles; and the viscous heating of rapidly flowing explosive as it escapes impacting surfaces. Many authors, however, have discounted gas compression as the controlling mechanism for hot spot formation [Frey, 1985 and Kang *et al.*, 1992].

Field *et al.* (1982) performed impact tests on thin layers of several explosives, reporting photographic evidence for the formation of initiation due to many of the previously stated mechanisms, as well as some additional mechanisms. In these tests, the explosives were subject to stresses significantly larger than the yield stresses of the materials. They concluded that the following mechanisms contributed to ignition of explosives: adiabatic shear banding, adiabatic heating of gas spaces, viscous flow, frictional rubbing, hot spots at crack tips and triboluminescence. The authors found that viscous heating could play an important role in liquids, but could only lead to significant heating in solids when considered in conjunction with the other mechanisms listed. They also determined that the propagation of cracks alone would not lead to ignition. Instead, they proposed that fracture of an explosive crystal would produce a gaseous void which could in turn lead to adiabatic heating and hot spot generation. In conclusion, the authors note that no one mechanism is the dominant means of ignition, and that small changes in the experimental conditions can lead to the formation of hot spots due to different mechanisms. For detailed reference on detonation theory with discussion of experiments, see Ficket and Davis (1979).

1.3 Adiabatic Shear Banding in Metals

Shear banding, as an initiation mechanism in explosives, is only simply understood. It is known that metals subject to high strain rate loading in association with high speed machining, cutting and forming, as well as in impact and penetration, often experience highly localized plastic deformation, known as shear bands. The thickness of these shear bands is typically on the order of micrometers, and they have been known to develop in times on the order of microseconds [Marchand and Duffy (1988), Giovanola (1988 a,b)]. Due to the significant amount of localized viscoplastic work on such a short time scale, highly localized temperatures of about 1000°C are observed. Although formation of these shear bands is typically followed by fracture, failure in any accepted sense of the word occurs with formation of the shear band since the material has lost its load carrying capacity [Marchand and Duffy, 1988]. Hence, a significant amount of research has been performed on shear banding as a failure mechanism in structural materials.

1.3.1 Experimental Observations

It is generally understood that adiabatic shear localization begins because thermal softening dominates over strain and strain rate hardening in the deformation process. When a material is plastically strained, dislocations begin to slip within the material, accumulating at grain boundaries. As these dislocations coalesce, there becomes less room for dislocations to slip. With further straining, the material becomes increasingly more resistant to dislocation motion, thus resulting in strain hardening of

the material [Lubliner, 1990]. In addition, if the rate at which this straining increases, viscous stress will further resist deformation, which contributes to a process known as strain rate hardening. An important result of dislocation slip is the generation of heat. Rogers (1979) has concluded that approximately 90% of this plastic work is converted into heat, while the remaining is stored in the generation and arrangement of dislocations. This increase in heat tends to free the motion of dislocations, resulting in thermal softening of the material. The generation of heat thus results in further plastic strain, which causes a further increase in temperature. At high enough strain rates, there is not enough time for the heat generated to be conducted away; the deformation is thus considered adiabatic. If a material is experiencing high strain rate adiabatic deformation, and there is a material or geometric weakness, such as a void or scratch, straining will increase locally, causing a blow-up phenomenon in temperature, shear strain, shear stress and velocity. This blow-up is commonly termed an instability; formally, it represents a rapid acceleration in a fundamentally unsteady process. If the properties of a given material are such that the mechanism of thermal softening dominates over strain and strain rate hardening, deformation will localize into a planar region of shear, known as a shear band.

The first person to observe localized temperature increases in a deforming metal was Tresca in 1878, as reported by Johnson (1987). Tresca observed red hot lines in the shape of the letter X, directly under a forging hammer and immediately following the forging of a platinum bar. An occurrence of this phenomenon is schematically represented in Figure 1.2 for a lead bar. Tresca concluded that these were the lines of greatest sliding and, hence, of greatest development of heat. He also realized that

platinum was an excellent material in which to observe these lines due to its relatively low thermal conductivity and low specific heat and due to the large amounts of energy required to deform it. Through a comparison of the heat generated by the experiment and the work done by the fall of the hammer, Tresca concluded that 70% of the plastic work was converted to heat, but that this number was not yet verified.

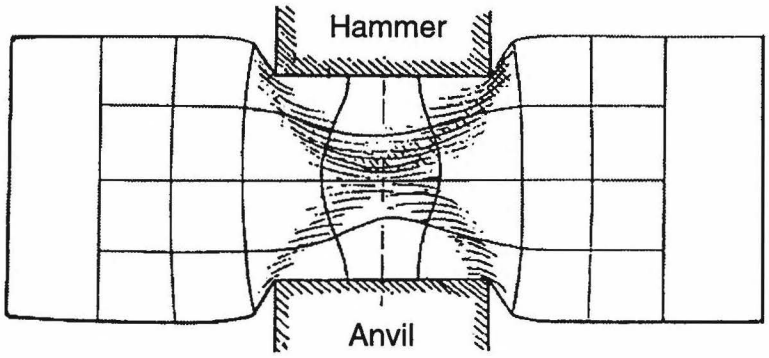

Figure 1.2: Schematic of a lead bar stamped by a hammer [Johnson, 1987].

Zener and Hollomon (1944) were among the first to describe the process of shear localization in detail. They state that a necessary condition for shear localization is when a maximum in the homogeneous, adiabatic stress strain curve exists, beyond which deformation cannot be homogeneous and strength decreases with increasing strain. When the strain at this maximum is surpassed, an instability will then arise, in which a region deforms at a greater rate than the surrounding material, causing it to weaken and further strain, while the surrounding material is no longer strained. Zener and Hollomon demonstrate this instability in shear with a punch test, in which the material was deformed at a strain rate of 2000 s^{-1}. The result of this test is seen in Figure 1.3. The white band of metal separating the plate and the plug is a

transformed martensitic band, which is characteristic of steel being quenched from a high temperature phase. The width of this band was about 32 μm. The authors concluded that a shear strain of 5 would raise the temperature 1000°C and that the material in this transformed band suffered a shear strain of 100.

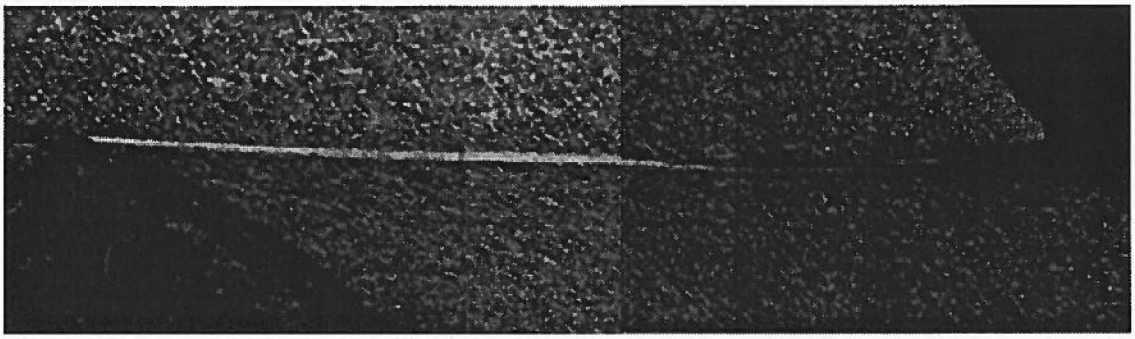

Figure 1.3: Martensitic transformed band produced by a punch on a $\frac{1}{4}''$ plate of 363 Brinell hardness [Zener and Hollomon, 1944].

In order to further study the deformation and temperature distribution across a shear band, Marchand and Duffy (1988) performed tests in simple shear on a thin tubular specimen of HY-100, a low alloy structural steel, by means of a torsional split-Hopkinson Bar (this apparatus will be discussed in detail in this thesis). Previous applications of this device only resulted in average values of shear stress and shear strain, determined by the rotations of the ends of the specimens. Marchand and Duffy were of the first researchers to perform detailed measurements of the shear band formation. They used high speed photographs to study the deformation of fine lines etched on the specimen's surface in order to determine the local shear strain. From an analysis of their photographs, they concluded that shear banding occurs in three distinct stages. In the first stage, the material is undergoing homogeneous

deformation, in which the grid lines are inclined at a constant angle, see Figure 1.4a. In the second stage, the material undergoes inhomogeneous deformation, in which the etched lines are curved, as seen in Figure 1.4b. As deformation continues in this stage, there is a continuous increase in the localized strain, while the width of the inhomogeneity decreases. It is important to note that, in this stage, the deformation remains uniform in the circumferential direction. The decrease in the stress, however, is never large over this region. The third stage begins at the value of nominal strain where the stress first starts to drop severely. As can be seen in Figure 1.4c, the deformation becomes severely localized in a thin plane. It is at this time that the one dimensional assumption of localization breaks down. Marchand and Duffy observed that the axial position of the maximum local strain is not the same for all points in the circumferential direction, differing by 100 μm, indicating that the shear band originates in several locations or that it originates in one location and propagates around the circumference of the specimen.

The maximum shear strain reached in the shear band, with an applied shear strain rate of 1600 s^{-1}, is 1900%, with a shear band width found to be 20 μm. These large strains demonstrate the weakening effect of shear banding. For dynamic loadings, deformation is often localized to a small region, which is forced to absorb the majority of the deformation. As a result, the strength of the whole specimen is not utilized, causing failure at much lower nominal strains than in quasi-static experiments.

Marchand and Duffy also performed temperature measurements across the shear band with infra-red radiation detectors. Results for an applied strain rate of 1400 s^{-1}

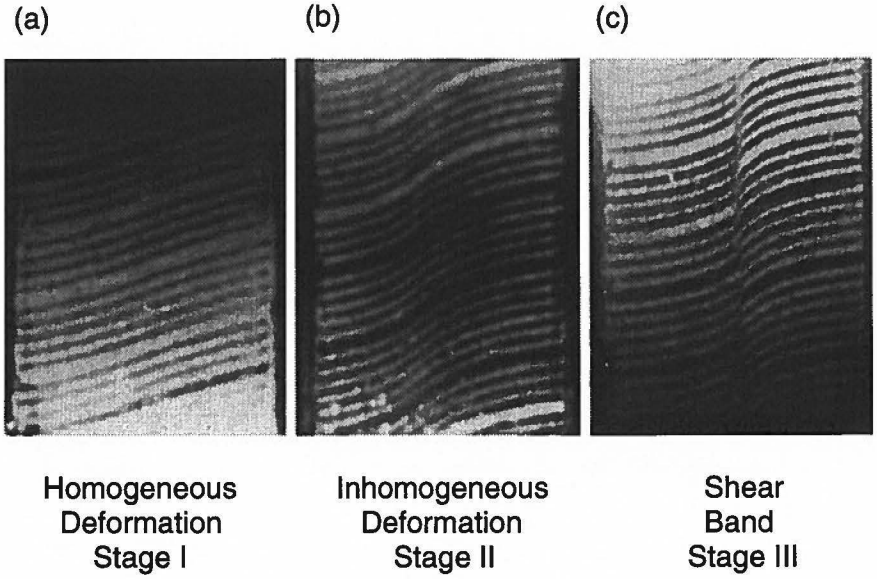

Figure 1.4: Photographs of the grid deposited on the surface of a deforming specimen of HY-100 steel in a torsional Hopkinson bar test, representing the three stages of deformation [Marchand and Duffy, 1988].

revealed a temperature spike at the location of maximum shear, with a maximum recorded temperature of 590°C. This value represents an average temperature over a region which is greater than the width of the shear band; from a calculation taking into account the width of the shear band, temperatures as high as 1000°C are surmised.

In a similar study, Giovanola (1988,a) performed tests on VAR 4340 steel. He used high speed photography to observe the deformation and infrared detection to determine temperature measurements. Using a similar method as Marchand and Duffy (1988), the author determined a local shear strain distribution, as can be seen in Figure 1.5. In accord with Marchand and Duffy, Giovanola determined a maximum shear strain at failure of 2000%. In addition, Giovanola found that shear banding occurred in two stages. In this paper, he reports the shear band widths to be 60 μm and 20 μm, with the second stage commencing within 5 μs from the start of the first

stage. The author also states that the strength of the material is virtually unaffected by the first stage, and that the localization in temperature occurs in the second stage, reaching values as high as 1100°C. It is also pertinent to note that Giovanola observed inhomogeneous deformation prior to shear banding, as was observed by Marchand and Duffy (1988).

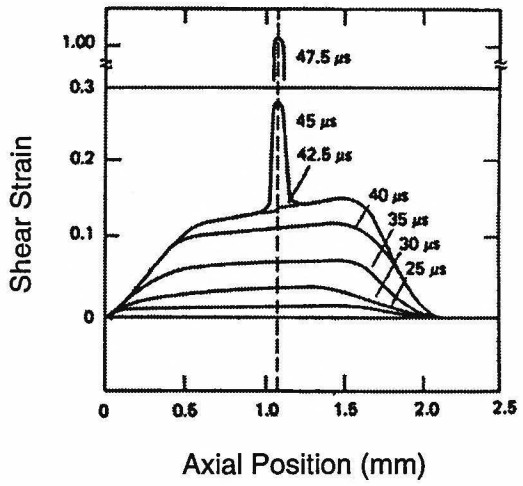

Figure 1.5: Strain profiles at different times obtained from photographic measurements of a deforming grid [Giovanola, 1988 a].

In a companion paper, Giovanola (1988,b) performs fractographic and metallographic observations of the failure surface to determine that the first stage corresponds to thermoplastic instability and the second stage corresponds to microvoid nucleation and growth. He also observed transformed material in the second band, interpreting that the martensitic material is produced by frictional heating resulting from the contact between the two failure surfaces after cracking had begun in the band. The importance of studying the phase change in the transformed band is thus deemphasized since the phase change occurs after the initiation of failure. In addition,

Giovanola notes that failure occurred on a number of parallel planes connected by well defined steps. This observation supports the claim that shear bands nucleate at a number of locations in the softened region and propagate around the specimen.

1.3.2 Theoretical Predictions

As a result of the significant amount of experimental data related to dynamic simple shear, determined from the torsional Hopkinson bar, and due to the mathematical ease in its modeling, much of the analytical work in the study of shear localization has been performed in connection with thermoviscoplastic simple shear deformation. In order to theoretically model the problem, governing equations are developed to model the relevant physical conservation principles. These principles do not form a complete set and are hence supplemented by constitutive equations, through which specific materials are modeled. A review of past works in the field of adiabatic shear localization is presented by Rogers (1979).

In the development of a constitutive model for stress, there are two schools of thought as to the method by which the strength is softened. The first theory is that the stress is reduced as a result of heat being generated from viscoplastic deformation. This process results in thermal softening, which dominates over strain and strain rate hardening. Alternatively, many researchers have studied the softening of the stress as a result of microvoid nucleation and growth. This theory is typically formulated to state that at some critical strain, voids begin to nucleate in the material, thus reducing the cross sectional area, and hence the strength of the material. Microvoid nucleation and growth is generally presented in conjunction with thermal softening,

microvoid nucleation being the trigger for thermal softening. Meyer (1992) gives a review of some of the constitutive relations which have been used for high strain rate applications. In the present thesis, a numerical model will be developed which takes into account softening due to viscoplastic work alone; microvoid formation will be neglected. Both mechanisms will, however, be discussed.

Thermoplastic Softening

In existing studies of thermal softening induced shear localization, there is a significant amount of discrepancy in the choice of the constitutive equation. In order to address this issue, Wright (1987) compared the results of four commonly used viscoplastic constitutive relations. In this study, Wright considered one dimensional simple shearing in a thermoviscoplastic material with elasticity, thermal softening, strain and strain rate hardening and heat conduction. The constitutive laws used were 1) an Arrhenius stress law, 2) the Bodner-Partom-Merzer law, 3) a simple power law, and 4) the Litonski law, which were all calibrated over the same data. He found that the results were both qualitatively and quantitatively similar, with the results within 5% of each other for shear strain rates up to $10^4\ s^{-1}$, a value far in excess of the calibration conditions. For even larger values of shear strain rate and high temperatures, the Bodner-Partom-Merzer law begins to diverge from the other solutions. Figures 1.6a and 1.6b demonstrate the similarity of the laws by comparing the stress with the strain rate and temperature at the center of the shear band. Wright states that since there is a significant difference between the strain rate and temperature at the center of the shear band from those of the calibration conditions,

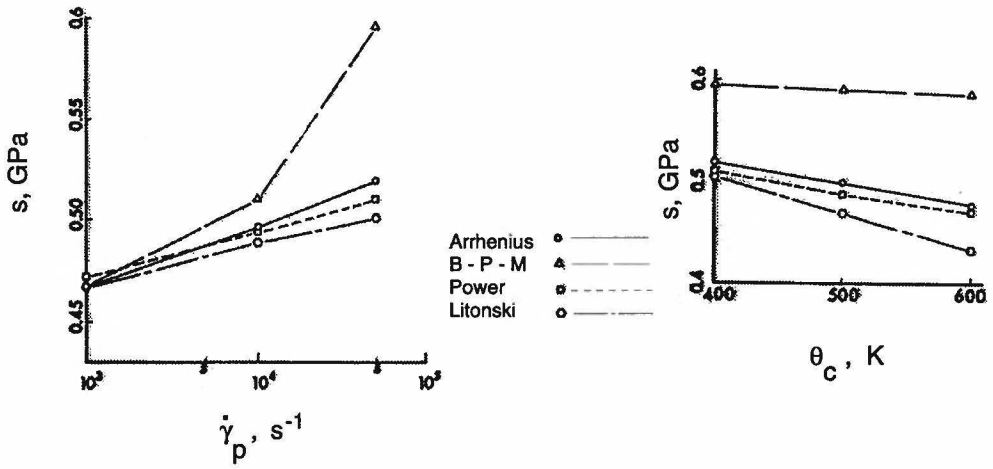

Figure 1.6: Comparison of various flow laws. (a) Driving stress versus central plastic strain rate when the central temperature is 400 K, (b) Driving stress versus central temperature when the central plastic strain rate is $5 \times 10^4 s^{-1}$ [Wright, 1987].

the actual structure of a real shear band would be expected to be somewhat different from that predicted by any given constitutive law. He thus thought it surprising that the trends predicted by the constitutive laws were as similar as found.

Another source of discrepancy in previous researchers is in the role of thermal conductivity. To clarify this issue, Batra and Kim (1991) compared the results of three different constitutive relations, while varying the thermal conductivity. In this study, the researchers considered a thermoviscoplastic block undergoing one dimensional simple shearing deformations, with strain and strain rate hardening and thermal softening. The thickness of the block was taken to vary smoothly with a 5% decrease in thickness at the center. The constitutive laws considered were the Litonski law, the Bodner-Partom law, and the Johnson-Cook law. From Figure 1.7, it is seen that the results of the three constitutive laws are extremely similar, both qualitatively and

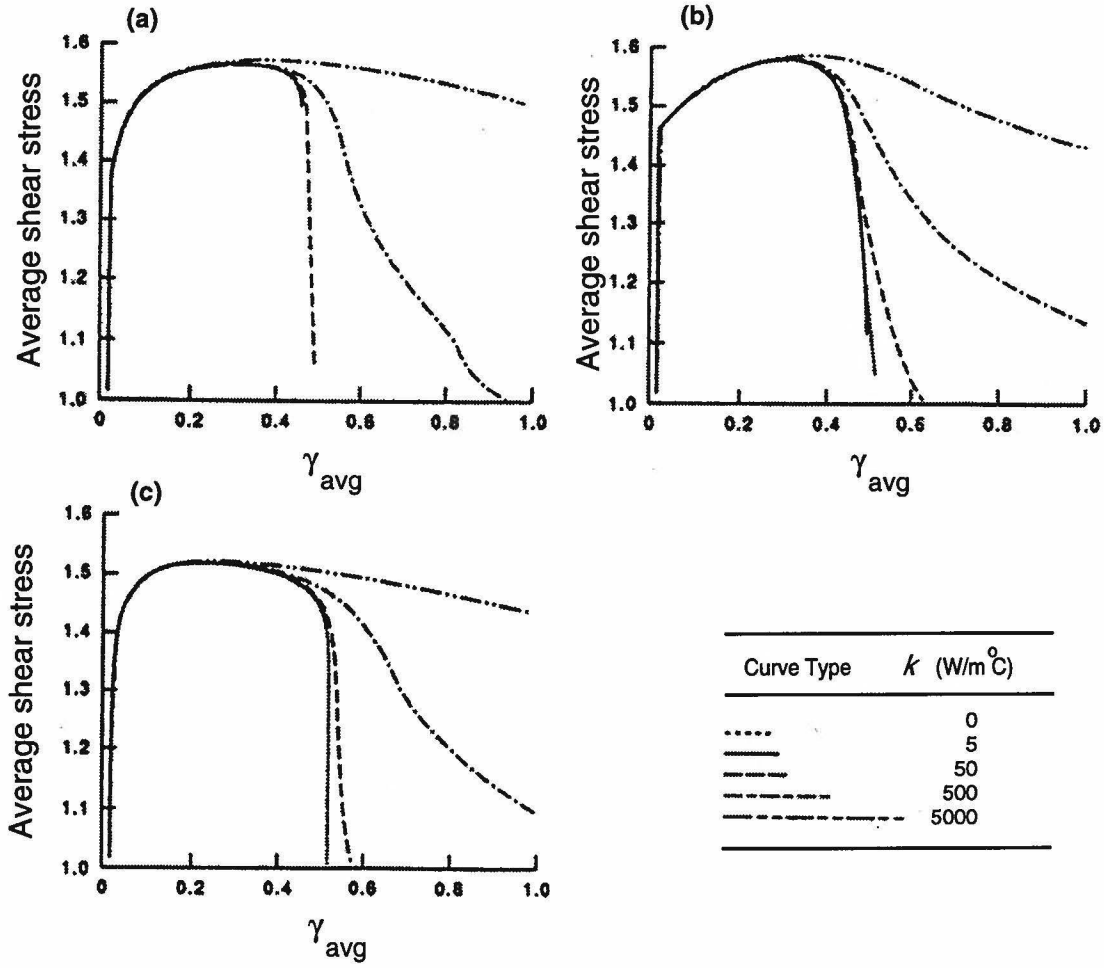

Figure 1.7: Comparison of the shear stress and shear strain distribution for various flow laws and thermal conductivities. (a) Litonski, (b) Bodner-Partom, (c) Johnson-Cook [Batra and Kim, 1991].

quantitatively, verifying the results achieved by Wright (1987). As a result of these studies, this researcher has determined that the use of a simple power law will be adequate in the study of high speed deformation.

By examining Figure 1.7, it can also be seen that large increases in the value of the thermal conductivity delay the initiation of stress collapse and slow down the development of the shear band. However, for realistic values of thermal conductivity there is little effect on the value of nominal strain at which stress collapses, and hence localization occurs. In contrast, by considering Figure 1.8, it can be seen that

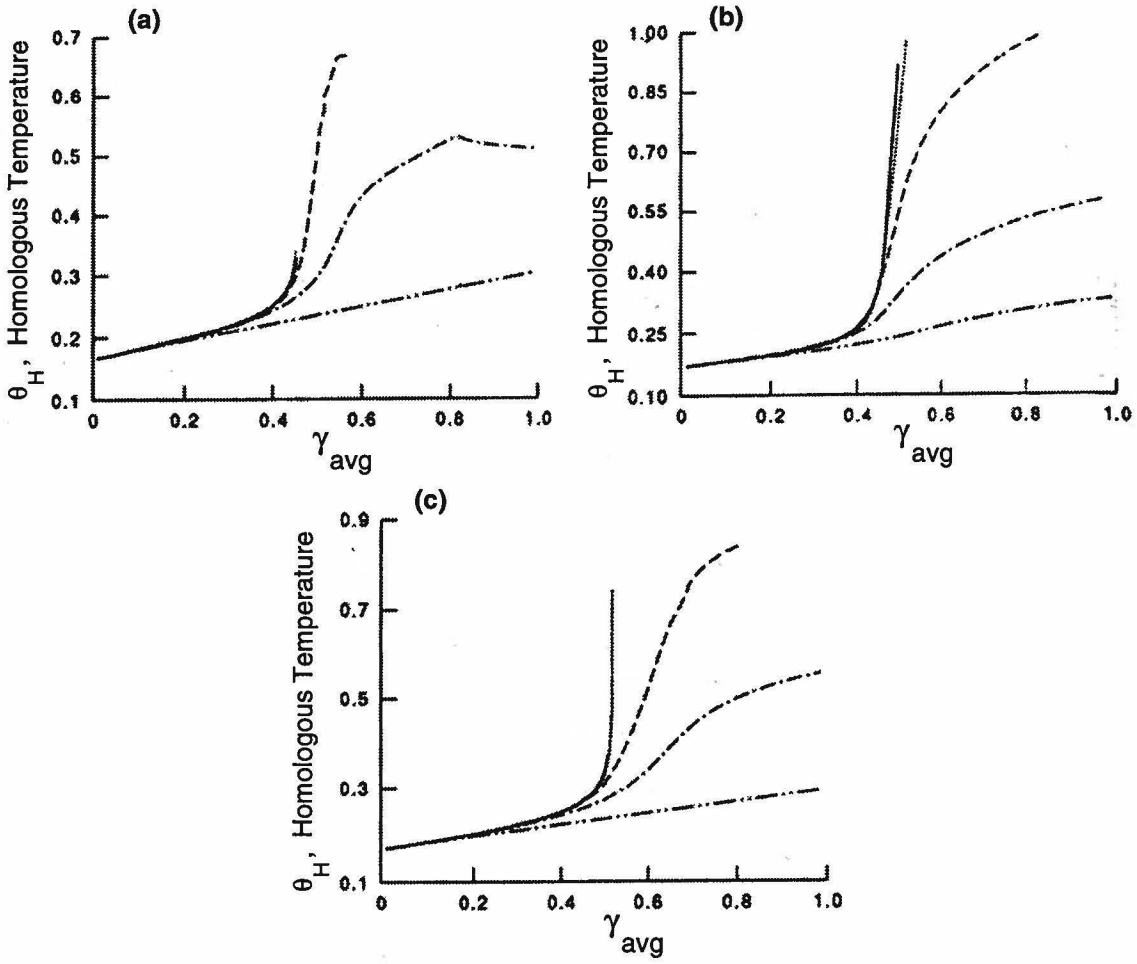

Figure 1.8: Comparison of the homologous temperature and shear strain distribution for various flow laws and thermal conductivities. The homologous temperature is the ratio of the material temperature to the melting temperature. (a) Litonski, (b) Bodner-Partom, (c) Johnson-Cook [Batra and Kim, 1991].

the rate of evolution of the temperature at the center of the specimen decreases with increasing thermal conductivity, resulting in significant changes in temperature for realistic values of thermal conductivity. It is therefore concluded that thermal conductivity can be neglected when one is only considered with the timing of stress collapse, but it proves to be crucial when considering shear band temperatures. Since this current thesis is studying thermal reaction initiation in explosives, conductivity will play an important role.

Motivated by this study, Batra *et al.* (1995) performed a thermoviscoplastic analysis neglecting thermal conductivity in order to rank twelve materials according to the critical strain necessary to reach localization in tubular specimens loaded in simple shear. A finite-element method with the Johnson-Cook constitutive law was used in these calculations. The thickness of the tube was taken to vary smoothly with a 10% decrease at the center. Batra *et al.* assumed that the shear band initiates when there is a catastrophic drop in torque, and ranked the materials according to the corresponding nominal shear strain. The results of this study are seen in Figure 1.9, where shear bands were found to initiate in the following order: tungsten, S-7 tool steel, depleted uranium, 2024-T351 aluminum, 7039 aluminum, 4340 steel, armco iron, carpenter electric iron, 1006 steel, cartridge brass, nickel 200 and OFHC copper, when tested with a shear strain rate of 5000 s^{-1}. It is relevant to note that the critical strain was dependent on the size of the initial defect as well as the finite element mesh used. The relative ranking of the materials, however, was independent of these parameters.

In order to study the early time behavior of shear localization, Wright and Walter (1987) performed a perturbation analysis on their full nonlinear system by means of a first order linearization about the homogeneous solution. The authors use a simplified constitutive law in which strain rate hardening and thermal softening are included, but elasticity and work hardening are excluded. They find that although the perturbation analysis does correctly predict the early time growth of small perturbations even past the point where peak stress is reached, it fails to predict anything about the later

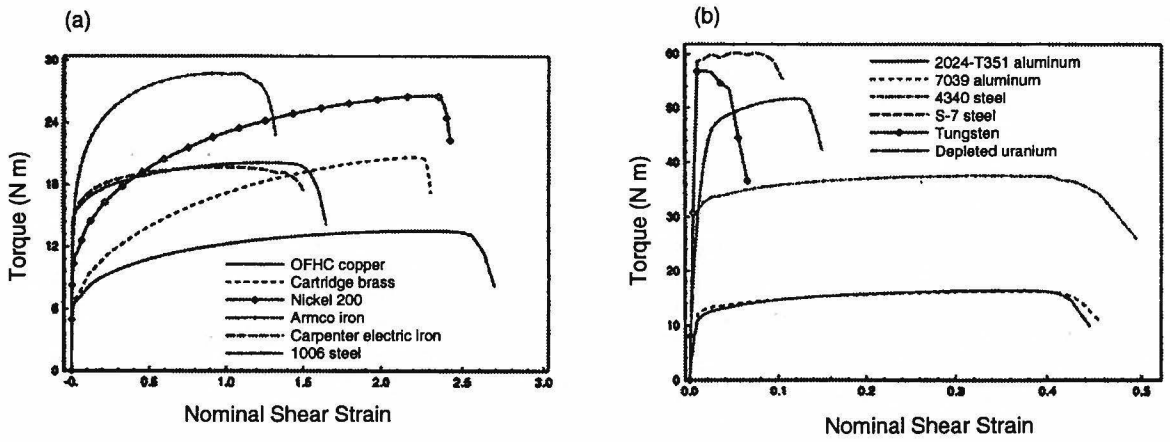

Figure 1.9: Relationship between applied torque and nominal shear strain for 13 materials [Batra *et al.*, 1995].

rapid growth in temperature and strain rate and the subsequent collapse in stress. This shows the limitation of linearized equations: once stability is lost, their results are unreliable at predicting the solution to the full nonlinear system. This analysis does, however, give a condition for absolute stability under which initial perturbations will decay. The authors conclude that localization is a multi-stage process. The first stage, which is described by their perturbation analysis, represents slow growth of initial inhomogeneities. This stage only represents a precursor to localization. Following this stage is a rapid transition into full shear banding, in which most of the localization occurs. The multi-stage process described by Wright and Walter (1987) is essentially the same as the three stage process described by Marchand and Duffy (1988), the only difference being that Wright and Walter failed to point out the initial stage of homogeneous deformation. This is due to the fact that they linearized about the homogeneous solution, assuming that the initial homogeneous stage existed at the start.

Batra and Kim (1992) observed similar results when they solved the full nonlinear system of equations for a thermoviscoplastic block with the Johnson-Cook constitutive law, including strain and strain rate hardening, thermal softening and thermal conductivity. They used a continuous variation in the thickness to instigate localization. The authors found the same three stage localization process as Marchand and Duffy (1988) with transition to stage two occurring at the time the stress reached its maximum value, and stage three occurring much later, when the stress has dropped to about 90-95% of its maximum value. Figure 1.10 is a plot of the velocity distribution in space, varying as a function of strain. By studying the slope of the velocity vs. position lines, one observes the three stage localization for S-7 tool steel when deformed at a strain rate of 1500 s^{-1} with the thickness of the center of the block being 5% less than that at the edge. Batra and Kim also observed the effects of varying the thickness of the block. They found that the defect size has a stronger influence on ductile materials than on less ductile materials, but in all cases, it has a significant effect on the critical strain to reach localization.

In a similar study, Clifton *et al.* (1984) used a simple power law including strain and strain rate hardening and thermal softening but neglected thermal conductivity to perform a study on the critical conditions for shear band formation. They concluded that the primary factor affecting initiation of the shear band is the strain hardening, whereas the strain rate hardening is the primary factor affecting the rate of growth of the shear band. Supplementing these observations, Wright and Batra (1985) used the Litonski flow law to explore the critical strain at collapse. Their results can be summarized through Figure 1.11, where case B represents a decrease in the strain

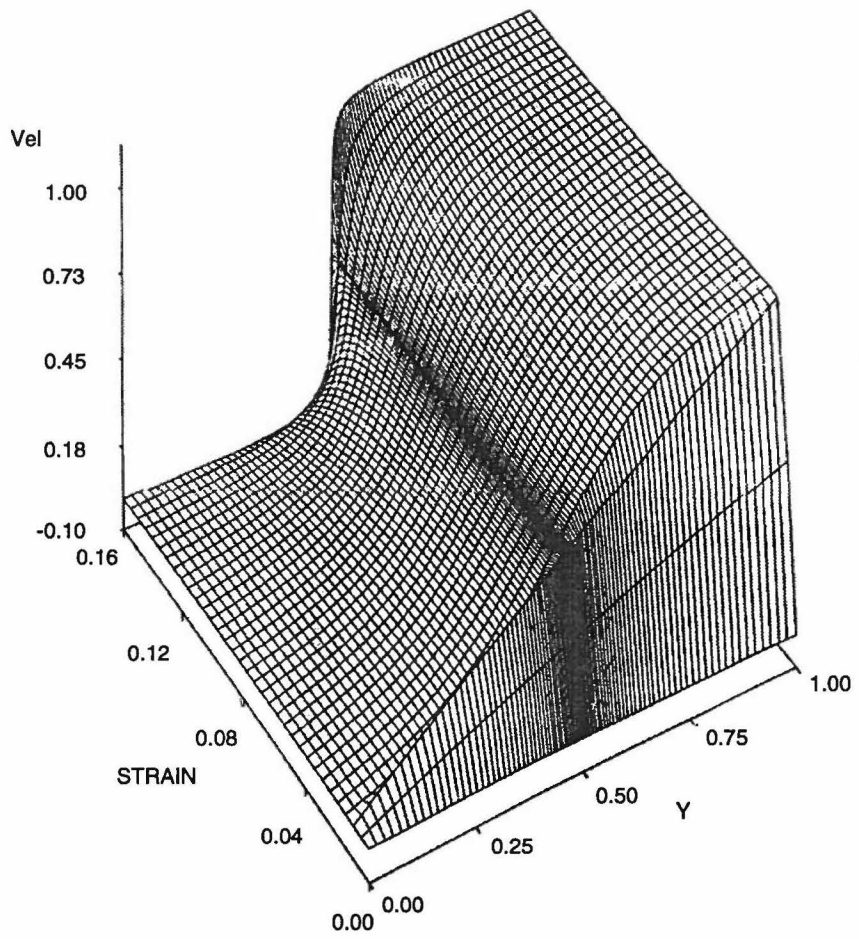

Figure 1.10: Evolution of the velocity field of a viscoplastic block of S-7 tool steel when deformed at a strain rate of 1500 s^{-1} [Batra and Kim, 1992].

rate susceptibility as compared to case A. In accord with Clifton *et al.* (1984), it can be seen that strain rate plays little role on the critical strain at localization, since the variation in the strain rate, when considering a small temperature perturbation, produces no change in the strain at localization. In contrast, the size of the temperature perturbation is seen to play a significant role, with the larger perturbation causing localization to occur at a smaller critical strain, as was observed by Batra and Kim (1992).

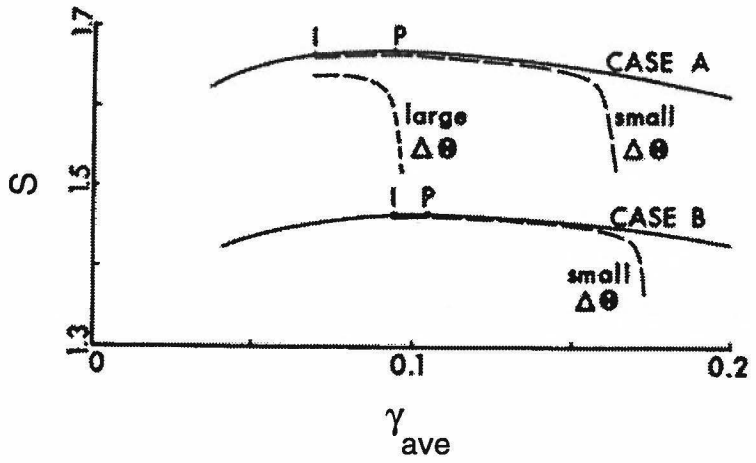

Figure 1.11: Stress, average strain distribution. Homogeneous and perturbed responses for Cases A and B [Wright and Batra, 1985].

It would thus seem that the determination of a critical strain is not the appropriate method to quantify shear band susceptibility, since the critical strain is affected by other parameters. Much research has been performed in attempts at determining a shear band susceptibility criterion. A few of these works will be briefly summarized here. In searching for a susceptibility parameter, Wright (1990) studies perfectly plastic materials and suggests that it may be more accurate to refer to a critical temperature than to a critical strain. He concludes that for materials with small strain rate dependencies, the early behavior of the softening function determines when localization will occur. In addition, Wright develops a shear band susceptibility parameter as a scaled ratio of the thermal softening function to the strain rate sensitivity parameter, thus not including strain hardening effects in his susceptibility. In a later article, Wright (1994) attempts to determine a defect invariant basis for susceptibility to shear banding. He postulates that collapse strain is only dependent on a linear combination of initial perturbations, and that there is a functional relationship be-

tween this scaled defect and the scaled collapse strain. Based upon this work, he includes a first estimate of a susceptibility parameter.

In another study of shear band susceptibility, Grady (1994) provides a shear band toughness criterion. As motivation for this work, Grady discusses the work by Marchand and Duffy (1988), where they found that shear bands propagate circumferentially with well defined fronts and finite velocities along the plane of shear. In a series of articles, Grady (1991, 1992, 1994) neglects strain hardening and viscous effects, using a simplified constitutive model with linear thermal softening to study the two dimensional shear band tip process zone. Anand, Kim and Shawki (1987) present a three dimensional generalization of a linear perturbation stability analysis for the onset of shear localization. The authors consider a thermoviscoplastic material exhibiting strain and strain rate hardening, thermal softening and pressure hardening. Anand *et al.* state that this method does not attempt to determine a critical strain at localization; it predicts the critical conditions for the onset of shear banding. In addition, they conclude that shear banding can initiate in two directions, in contrary with previous research which predicts shear banding only in the direction of shear. They conclude that for pressure insensitive materials, shear bands are expected to develop in directions parallel and perpendicular to the direction of shear. In pressure sensitive materials, shear bands are expected at angles of $\pm 45°$ from the direction of shear. Finally, Shawki (1994, a and b) and Cherukuri and Shawki (1995, a and b) discuss an energy based criterion for the onset of shear localization.

Microvoid Nucleation and Growth

In the study of the formation of shear bands, it has been found that in a number of cases, thermoplastic theory has over-estimated the magnitude of the shear strain at the instance of localization. To explain this, a number of researchers have focused their attention on a microstructural geometric instability concerned with the nucleation and growth of microvoids.

In an explanation of the peak load on load displacement graphs, Dodd (1993) discusses three mechanisms by which an instability, which causes this peak stress, may occur: 1) a process instability due to the material geometry, 2) a microstructural instability due to the nucleation and growth of voids, and 3) thermoplastic shear instability due to thermal softening. Dodd summarizes the works of previous researchers to describe the sequence by which void nucleation leads to the ductile fracture of metals. In the first stage, voids nucleate at second-phase particles, or inclusions, often at a critical local strain. Secondly, with increasing plastic strain, the volume fraction of the voids increases. In the third stage, after a critical applied strain or mean free path between voids, plastic deformation is localized along shear bands between voids. Finally, fracture occurs along the shear bands, forming "void sheets." These void sheets are demonstrated schematically in Figure 1.12.

Dodd also discusses the interplay between shear band formation due to thermoplastic instability and due to void nucleation and growth, in terms of critical strains. He states that if the void nucleation strain is sufficiently large, shear band formation and eventual fracture occurs due to thermoplastic instability. If, however, the void nu-

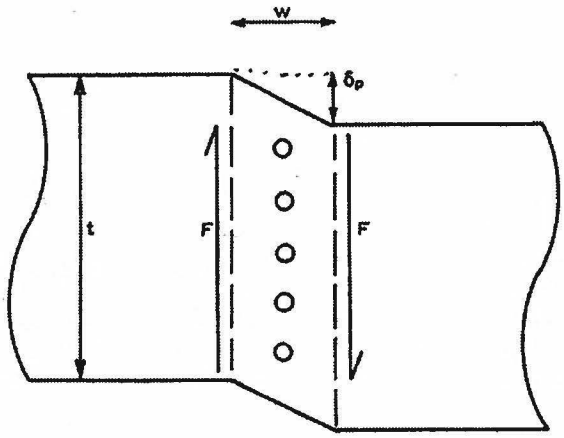

Figure 1.12: Schematic diagram of the formation of void sheets [Dodd, 1993].

cleation strain is lower than the thermal softening strain, voids will form and thermal softening will occur in the ligaments between the voids. If the two instability strains are equal, failure occurs by an interplay of the two methods. It is thus seen that thermoplastic instability always plays a role in shear banding, but void nucleation is often the triggering event for its onset. Dodd also states that for dynamic loading, the void nucleation strain is generally increased above the thermoplastic instability strain. Dodd concludes that the peak in the load displacement diagram typically results from an instability due to process instability, or microvoid nucleation; but, for materials with low density and specific heat, thermoplastic instability could be the cause of the peak.

Dodd and Atkins (1983) and Osakada *et al.* (1977) discuss the significance of hydrostatic stress on the void nucleation strain. They conclude that increasing the hydrostatic compression tends to raise the void nucleation strain, this is demonstrated in Figure 1.13. In fact, a large enough hydrostatic compression will suppress void

nucleation completely. However, once thermoplastic instability occurs, voids may begin to nucleate within the shear band. Dodd and Atkins also state that hydrostatic tension tends to decrease the void nucleation instability strain. In the limit of large hydrostatic tension, voids will nucleate immediately at the onset of plastic straining.

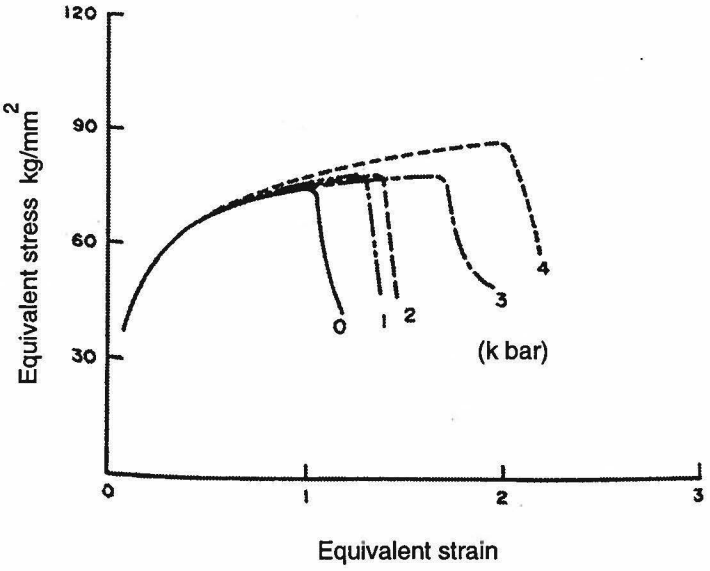

Figure 1.13: The effect of superimposed hydrostatic compression on instability in sheer for a carbon steel [Osakada, 1977].

A numerical analysis for the formation of adiabatic shear bands due to the combined effects of void nucleation and thermoplastic deformation is later performed by Kobayashi and Dodd (1989). In considering the deformation of a thin tubular specimen deformed in simple shear, they develop a three stage model in which initial softening is controlled by thermal softening. At a critical strain, voids begin to nucleate at a uniform rate throughout the specimen. At some instability strain, additional voids begin to nucleate at a certain point in the gauge section. Numerically, void nucleation is implemented through a decrease in the cross sectional area of the spec-

imen. The authors state that during deformation in the uniform nucleation zone, shear banding is equally possible at any point. Non-central shear banding is thus possible, providing there is a trigger for localization, such as a void, crack or geometric imperfection. It is thus concluded that the nucleation and/or pre-existence of geometrical imperfections is critical in locating shear bands, while thermal softening is an important factor in their growth.

More recently, Batra and Jin (1994) performed a study on the initiation and growth of shear bands in a geometrically and thermally softening viscoplastic block deformed in plane strain tension. They performed a two dimensional study in which an initial defect is modeled by weakening the material in a region surrounding the centroid of the cross-section. Void growth was modeled through the growth of their volume fraction due to plastic dilatation and plastic strain controlled nucleation, occurring at a critical plastic strain. They found that an increase in the strain rate delayed the initiation of localization due to the effect of inertia forces. In addition, it was concluded that, for the material parameters involved, softening due to the increase in porosity is more than that induced by the rise in temperature.

1.4 Detonation Mechanisms in Explosives

As was stated previously, shear localization is understood to be one of the mechanism which can lead to ignition in solid explosives subject to high strain rates and relatively low pressures. Traditional studies of shear localization in explosives have been performed in conjunction with high pressures, representing the conditions undergone in shock and impact loading. Frey (1981) developed a model to describe

heating in high explosives due to shear banding. He used a linear viscoplastic constitutive law, neglecting the effects of strain rate hardening. The strength was decreased over a 30°C range after the melting point, the melting point increased linearly with pressure, and the viscosity was dependent on both temperature and pressure. In addition, Frey used Arrhenius kinetics to model the thermal explosion. This material was then deformed in shear, stimulating localization by setting the strength to zero over a small region within the deformation. Without reaction, Frey's model achieved a maximum temperature which turned out to be independent of strength of the material and thickness of the initial weakness. These parameters did, however, affect the rate of growth of the shear band. The author found that the factors which did affect the temperature were the pressure, strain rate, and viscosity. To demonstrate the pressure dependence, Figure 1.14 reveals the shear velocity required to achieve thermal explosion in 1 μs as a function of pressure. Since an equivalent amount of energy must be required to set off thermal explosion, it is determined that at high pressures, lower shear velocities result in higher temperatures. It is thus seen how temperature is strongly affected by the pressure, due to the strong dependence of viscosity and melting temperature on pressure. This result would lead to the assumption that under low pressures, it would be very difficult to reach the temperatures in a shear band required to instigate thermal explosion.

Frey also demonstrates the importance of thermal conductivity when modeling explosives. Figure 1.15 shows a plot of temperature as a function of time. Here, it is seen that when shearing is stopped just prior to thermal explosion, the heat is conducted away and no reaction occurs. This observation is in accord with the study

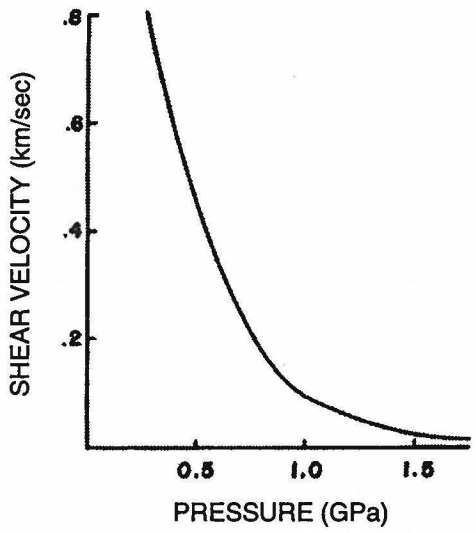

Figure 1.14: Shear velocity required to achieve thermal explosion in 1 μs as a function of pressure [Frey, 1981].

by Batra and Kim (1991), reaffirming the conclusion that, in order to accurately model detonation in shear bands, thermal conduction must be included.

In experiments performed on explosives subject to lower pressures and shear deformation, such as in drop weight tests, Boyle, Frey and Blake (1989) confirm the numerical observations of Frey (1981). They find that pressure and velocity do indeed have a strong effect on the initiation of solid explosives. Due to a comparison of explosive materials, they also verify that higher viscosities increase the sensitivity to explosion. In a more recent study, Chou *et al.* (1991) studies two theories for the impact initiation of explosives: shock initiation, a pressure dependent theory, and shear initiation, a temperature dependent theory. Chou *et al.* state that there are three means by which heat can be generated in explosives: shock compression energy, plastic work and viscous work. They state, in accord with previous researchers, that plastic work, in the absence of high pressures, would not generate enough heat

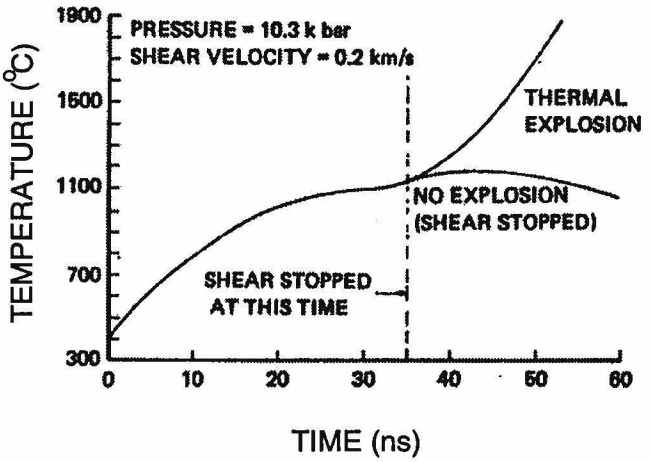

Figure 1.15: A demonstration of the effect of thermal conductivity. Temperature as a function of time when shearing is arrested prior to explosion [Frey, 1981].

to produce thermal explosion, since failure occurs before a significant amount of straining occurs. Chou *et al.* further state that once a material has reached its melting temperature, the effect of plastic work becomes negligible; heating then results from viscous work, which is capable of increasing the temperature well above the melting point. It is known, though, that brittle materials become more ductile under pressure; in fact, Chou *et al.* state that pressure can raise the stress and strain to as much as ten times as high as a material's uniaxial value. This effect thus increases the importance of considering heating by plastic work, when considering a material under hydrostatic pressure.

In order to compare the effect of shock and shear initiation in impacted explosives, Chou *et al.* developed a numerical model similar to that of Frey (1981) and simulated the impact of bare and covered explosives subject to impact. In the first case, an uncovered explosive is impacted with a projectile. Chou *et al.* found that with a constant yield stress and at an impact velocity of 600 m/s, the temperature at the

edge of the impact zone reaches its maximum value of 522 K after about 3 μs, see Figure 1.16a. In addition, they report pressures reaching a maximum of 3.4 GPa over a large region at 1 μs following impact. When the explosive is covered with a

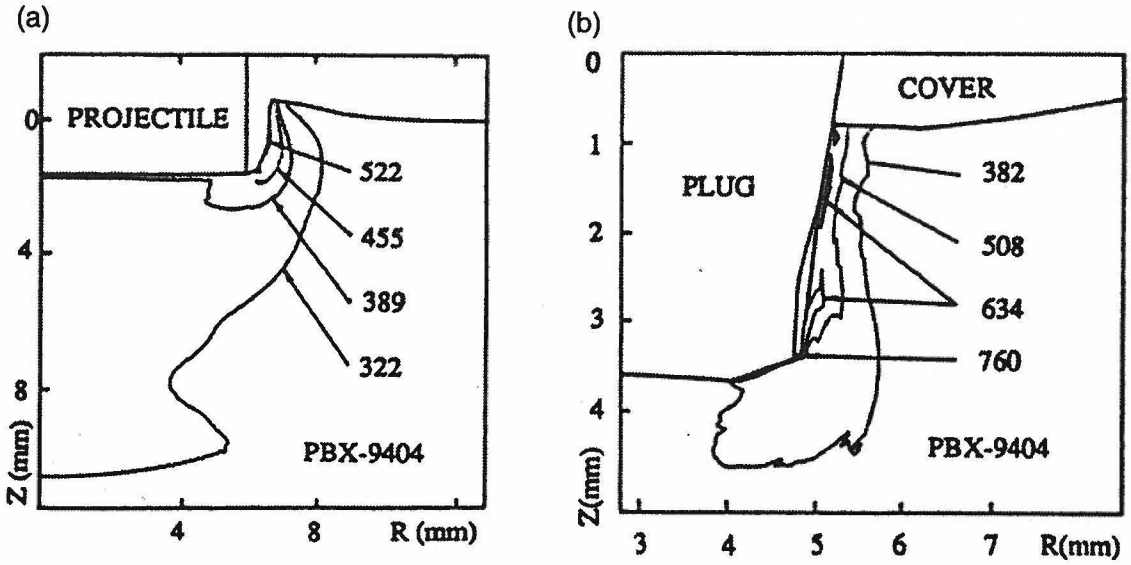

Figure 1.16: Temperature contours (K) in a PBX 9404 charge. (a) Bare charge at 3 μs after impact by a steel projectile at 600 m/s, (b) Covered charge at 10 μs after impact by a steel projectile at 1500 m/s[Chou *et al.*, 1991].

steel plate and impacted, there is a considerable decrease in the shock intensity in the explosive, with a maximum of 1.4 GPa reached in a very small region 1 μs following impact, hence reducing the possibility of shock initiation. Temperature results reveal higher temperatures at the edge of the plug than in the uncovered explosive, thus increasing the possibility of shear initiation. As the plug penetrates the explosive, temperatures increase due to viscoplastic heating and continue to increase with time. Results of the temperature profiles seen in Figure 1.16b show a maximum temperature of 760 K after 10 μs. Chou *et al.* thus conclude that for bare explosives impacted by a projectile, shock initiation is dominant and the shear effect is negligible. For

covered explosives impacted by a projectile, viscoplastic heating is of importance and shear initiation at the edge of the plug is probable.

In this thesis, Chapter 2 will discuss the design and analysis of the TSHB, built by this researcher. Chapter 3 will present the analytical modeling of the deformation to which the TSHB specimen is subject. In Chapter 4, results from the experiments as well as the analytical model will be presented and compared with each other. Finally, Chapter 5 will give the conclusions.

CHAPTER 2

EXPERIMENTAL METHOD

This chapter discusses an experimental apparatus, known as the torsional split Hopkinson bar (TSHB), which was used to test metals, solid explosive simulants and solid explosives in simple shear. An analysis of the data determined from this apparatus produces average shear stress and shear strain characteristics of the tested material, for a range of shear strain rates ($10^2 - 10^4\ s^{-1}$). High speed photographs are taken of the deformation and failure of the specimens, in order to determine their failure mechanism. The data will be used to determine constitutive parameters for input into the numerical model which is presented in the next section. This data can also be used to calibrate the various constitutive laws used in finite element packages such as EPIC and ABAQUS, which can be used in the modeling of explosive mechanics.

The torsional Hopkinson bar is a modification of an apparatus originally discussed by Kolsky (1949, 1953). In his device, thin cylindrical wafer-like specimens were placed between two long elastic bars, aligned along a common axis. The specimen was loaded by propagating a compressive pulse, generated by impacting the bar with a cylindrical projectile of the same material and equal diameter, down one of the bars toward the specimen. This technique has also been discussed by Lindholm (1964) and Follansbee (1985). A similar device was used by Harding *et al.* (1960) and Nicholas

and Bless (1985) for material testing in tension. The Hopkinson bar was first adapted for tests in torsion by Baker and Yew (1966) and is also discussed by Duffy *et al.* (1971), Lewis and Campbell (1972), Hartley *et al.* (1985), and Weerasooriya (1990).

There are several reasons why the TSHB is appropriate for the current experiments performed on solid explosives. First of all, in torsional loading, the maximum stress in the specimen occurs on the exterior surface of the material. The largest deformation will thus occur on the exterior surface, making the probability of hot spot formation greatest, where it can easily be observed. Also, the TSHB can be designed to produce a torsional pulse of almost any desired length, and hence, large amounts of deformation in the specimen are possible. The apparatus can easily be designed to produce more deformation than the specimen can withstand. In addition, shear is the main form of deformation present in high rate deformation events such as penetration; hence, it is desired to determine stress-strain characteristics in shear, as opposed to compression or tension. Compression and tension test results can be converted into shear data by using a criterion such as the von Mises equivalence relation, but this is not valid for strains above 20% [Hartley and Duffy, 1985]. Further disadvantages of compressive testing result from the Poisson's ratio effect, which causes radial expansion of materials loaded in compression, resulting in a radial stress component superposed on the axial component. Additional radial stresses in compressive tests occur due to frictional effects between the specimen and bar. In torsional tests, there is no Poisson's ratio effect, and hence no radial contraction or expansion.

There are, however, some drawbacks to the TSHB. First, tests may only be run on a limited range of strain rates ($10^2 - 10^4\ s^{-1}$). The lower limit is due to an increase

in the noise to signal ratio, while the upper limit is due to the elastic limit of the TSHB. A further drawback is if fracture occurs in the explosive specimen too soon, localization, and hence initiation, is less likely. In addition, the data analysis for this apparatus assumes homogeneous deformation. Hartley *et al.* (1985) have shown that it takes a few reflections of the loading pulse from the ends of the specimen before a state of homogeneous deformation is reached, thus rendering the early time results of the TSHB inaccurate.

2.1 Description of Apparatus

The TSHB, seen in Figure 2.1, consists of two elastic cylindrical bars: an incident and transmission bar; a torsional pulley; a clamp; and a specimen. A schematic of

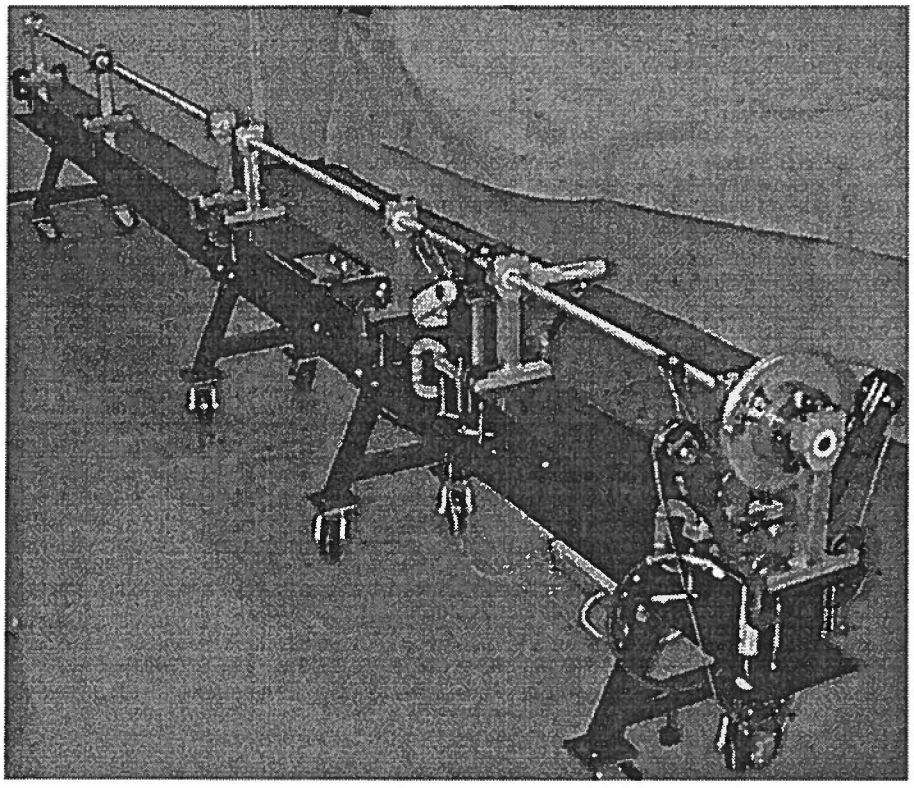

Figure 2.1: Photograph of the TSHB used in this research.

this apparatus is included in Figure 2.2. The two bars are aligned along a common axis, with a thin walled cylindrical specimen of known geometry joining them. The end of each bar in contact with the specimen is milled to produce a hexagonal socket, into which the specimen or an adaptor is inserted. The adaptor is used for cases in which it is desirable to glue the specimen in place, rather than grip it with the hexagonal socket. The torsional pulley is attached to the end of the incident bar far from the specimen, and the clamp is placed at a variable distance from the pulley, typically several feet. The clamp is used to prevent rotation of the incident bar while the torsional pulley is rotated, thus storing a torsional pulse in the bar between the pulley and clamp. The sudden release of the clamp propagates an incident shear strain pulse down the incident bar. The incident pulse reaches the specimen, transmitting some shear strain through the specimen into the transmission bar and reflecting some back into the incident bar.

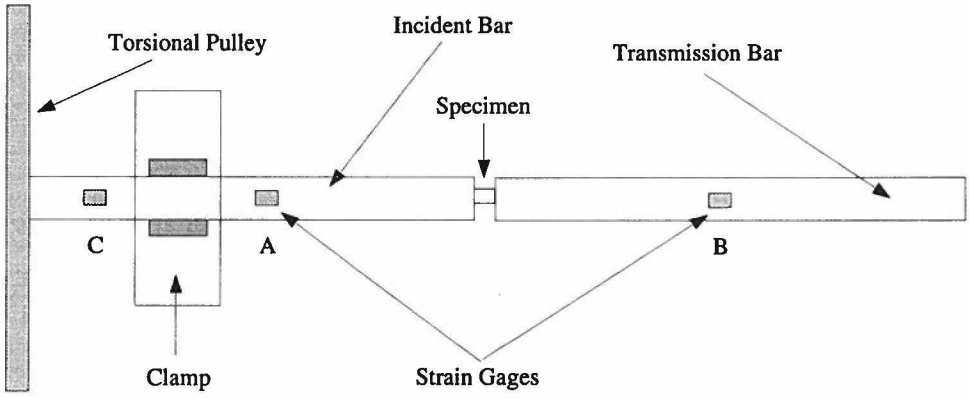

Figure 2.2: Schematic of the TSHB (not to scale).

The two elastic bars are constructed of 1 *in* diameter aluminum 7075-T6, 111 *in* in length. At the ends joining the specimen, a hexagonal socket, of width 0.5625 *in* and depth 0.25 *in*, is milled into the bars. Into these sockets, one inserts either

a hexagonal specimen or an adaptor machined from 7075-T6 aluminum, to which cylindrical specimens are glued. The hexagonal specimen (see Figure 2.3) or adaptor (see Figure 2.4 is fixed to the bar with 12 set screws, two on each face of the hexagon. Figure 2.5 shows a photograph of the bars with a hexagonal specimen inserted into the socket. The dimensions of the specimens that were used in this study and adaptor are given in Figures 2.3, and 2.4, respectively. In Figure 2.3, the central part of

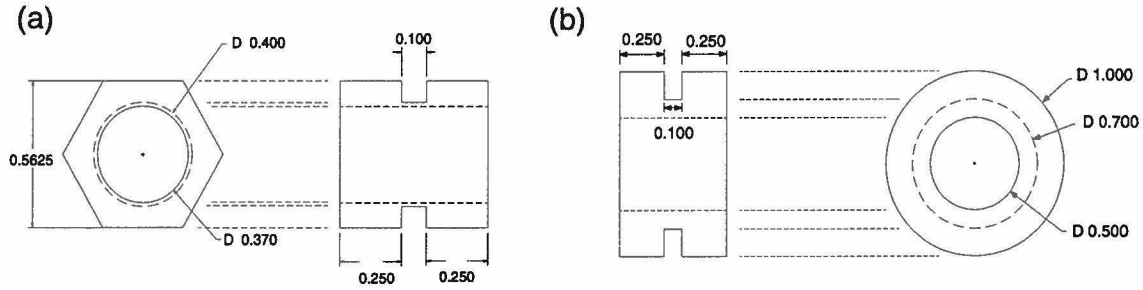

Figure 2.3: Scaled diagram of the specimens used in the TSHB tests: (a) hexagonal specimen, (b) cylindrical specimen (all dimensions in inches).

the specimen is commonly referred to as the gage length, while the ends are termed flanges. The hexagonal specimen is used to test metals and the cylindrical specimen, due to its ease in machining, is used to test the explosive simulants and explosives. The ratio of the wall thickness of the gage length to the mean diameter of the gage length for the hexagonal and cylindrical specimens are 0.04 and 0.17, respectively. The

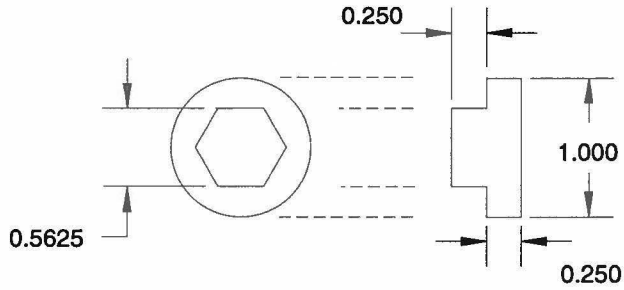

Figure 2.4: Scaled diagram of the adaptor (all dimensions in inches).

elastic bars are supported along their length by delrin bearings, which are mounted on adjustable bearing supports. These bearing supports are then fixed to a steel I-beam which supports the whole TSHB apparatus.

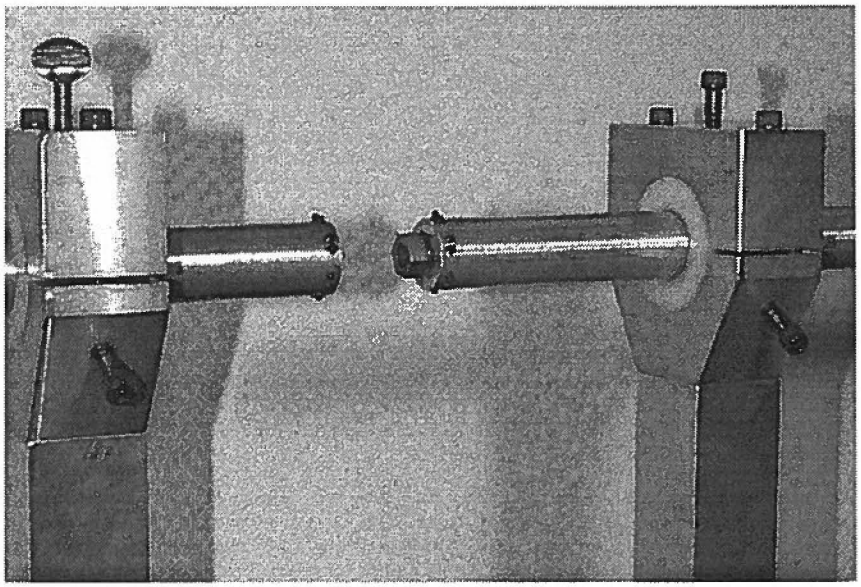

Figure 2.5: Photograph of a hexagonal specimen inserted into the socket of the incident bar.

A photograph of the torque generating mechanism is seen in Figure 2.6, and a schematic of this mechanism is included in Figure 2.7. The torsional pulley is clamped to the incident bar by means of a frictional fit. A hydraulic hand pump is used to pressurize the rams, which lengthen, transferring force into the cable, which in turn rotates the torsional pulley. When the clamp is engaged, this action stores torsional elastic energy in the incident bar.

Integral in the operation of the TSHB is the clamp which stores the torsional pulse. Figure 2.8 shows a photograph of the clamp used in this research. The key to constant strain rate tests is rapid release of the clamp, which propagates an incident torsional pulse towards the specimen. In order to more fully understand the operation

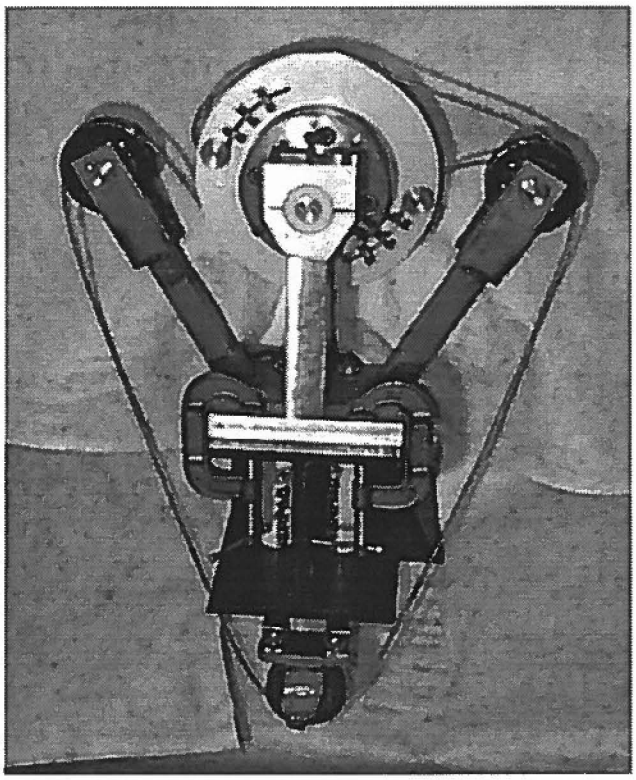

Figure 2.6: Photograph of the torque generating mechanism.

and design of the TSHB, the author spent the summer of 1995 at Eglin AFB in the Advanced Warheads Evaluation Facility (AWEF) making modifications to the design of their TSHB. With the knowledge gained through these efforts, this author modified previous clamp designs resulting in the design shown in Figure 2.9. The clamp is engaged by pumping a second hydraulic hand pump, which pressurizes a hydraulic C-clamp, which in turn clamps the base of the two clamp faces, as is seen in Figure 2.8. This action transmits pressure through the clamp faces onto the Hopkinson bar. In order to release the clamp, the hydraulic pressure is increased until the break element, as seen in Figure 2.9, fractures, causing the release of the clamp faces. Ideally, the incident pulse would be a square pulse of torsion, with instantaneous rise and fall time and constant magnitude, thus producing deformation in the specimen at a constant

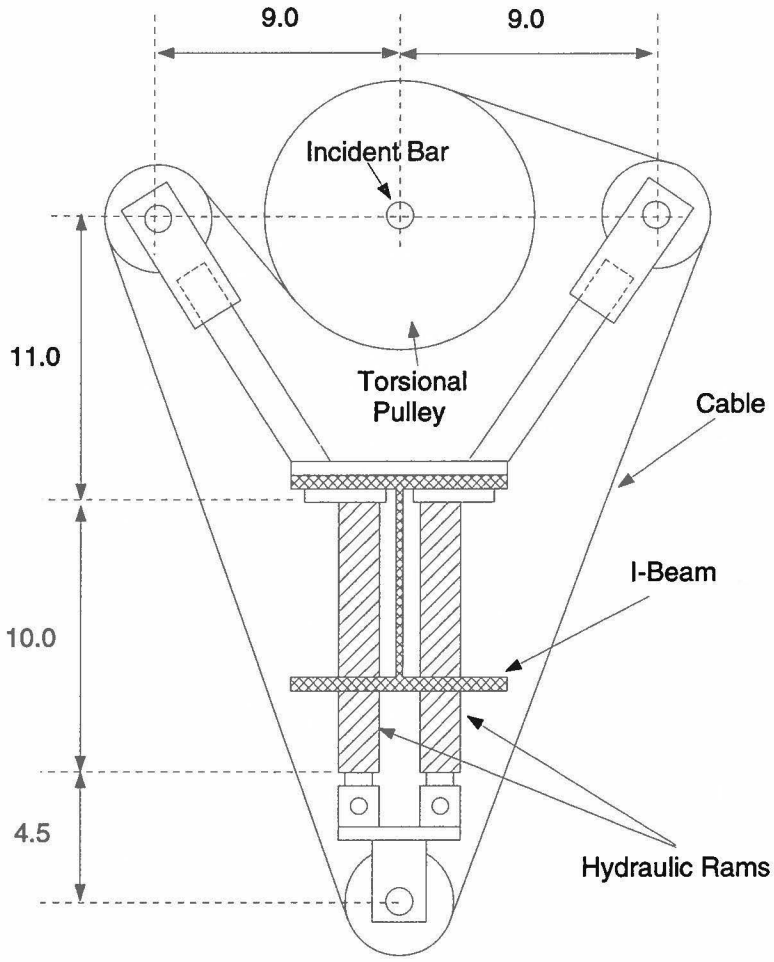

Figure 2.7: Scaled schematic of the torque generating mechanism (all dimensions in inches).

strain rate. For optimum functioning of the clamp, it is desired to store large amounts of elastic energy in the clamp in order to achieve quick fracture of the break element and consequently, sudden release of the clamp. This sudden release will produce a pulse with a short rise time and relatively constant magnitude.

In designing a break element, it is desired to use a material with minimum ductility, but not so brittle that it will fail before the clamp is tight enough to store the desired torque. Hartley *et al.* (1985) state that functional pin materials include aluminum 6061-T6 and 2024-T6. In order to determine the effect of the break element

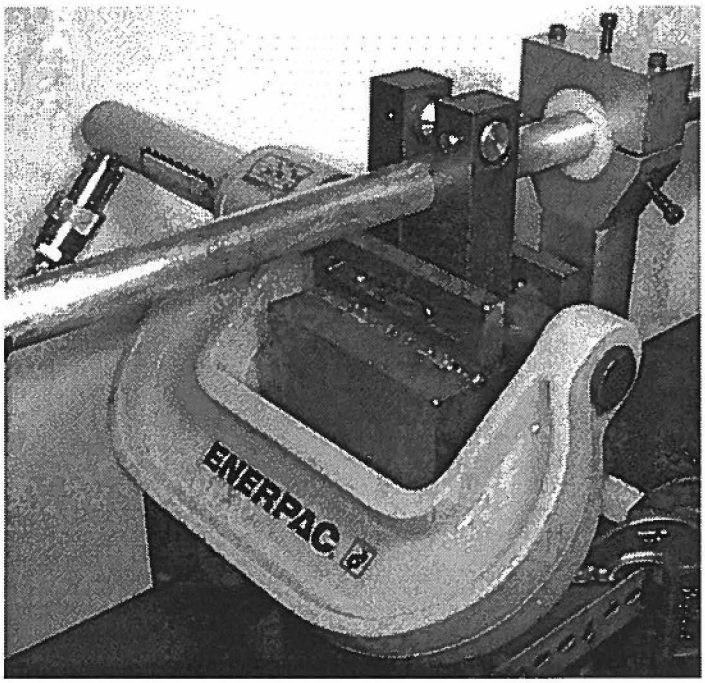

Figure 2.8: Photograph of the clamp for the TSHB.

notch geometry on the release of the clamp, the author performed quasi-static uniaxial tension tests with V-notched and square-notched elements. The break element is secured to the clamp faces with a pin, hence, the clamp faces are free to rotate relative to the break element. The break element thus experiences almost pure tension, validating the uniaxial notch geometry tests. The results of these tests on a 0.75 *in* diameter aluminum 2024-T3 elements, with an inner notch diameter of 0.425 *in*, are presented in Figure 2.10. From this figure, it is seen that the V-notched specimens exhibited a more elastic deformation, evident from the linear load-displacement relationship seen in the graph, whereas the square notched specimens went through a significant amount of plastic deformation before failure. In plastic deformation, mechanical energy is being transformed irreversibly to thermal energy; elastic energy is thus more desirable as it is fully recoverable. In addition, Figure 2.10 shows that the

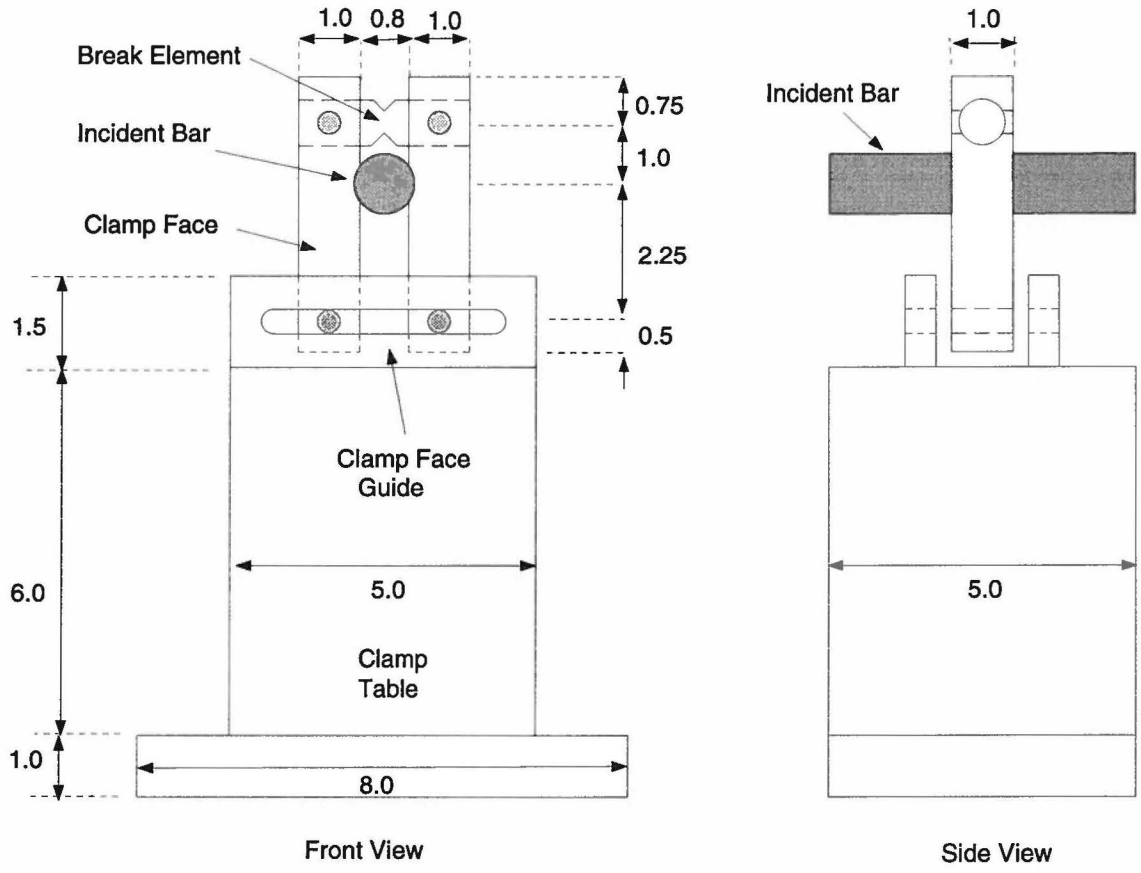

Figure 2.9: Schematic of the clamp for the TSHB (all dimensions in inches).

square notched specimens displace a longer distance during deformation. This will result in more rotation of the clamp faces before release, thus providing a mechanism for the incident bar to slip in the clamp. Upon analysis of the failure surface of the break elements, it was noticed that the V-notch had a planar failure surface, while the square notch had a more irregular failure surface. The V-notched break element tests were also very repeatable.

As a result of these tests, a V-notch was deemed more effective in achieving the desired clamp release qualities and was implemented into the break element design. The final break element was machined from 0.75 *in* diameter aluminum 6061-T6 rod,

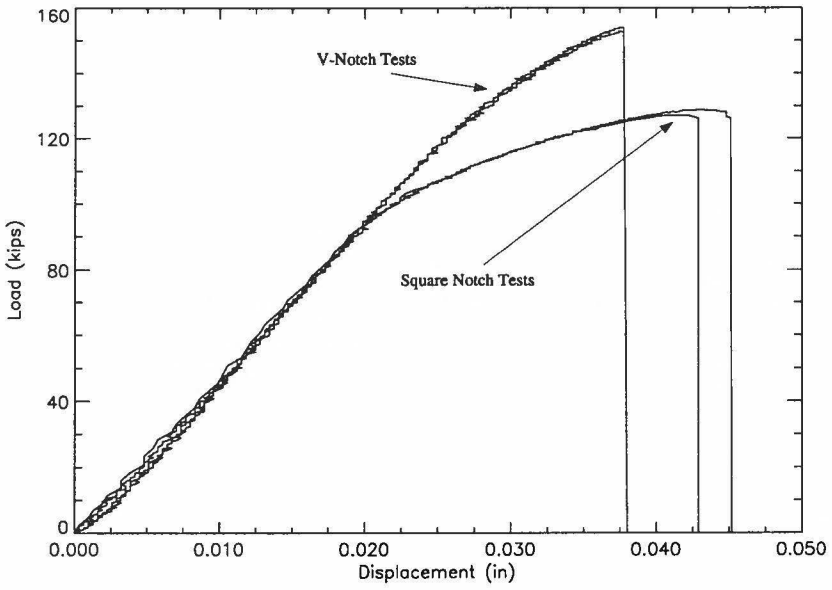

Figure 2.10: Break element notch geometry tension test.

with the diameter at the center of the notch reduced to approximately 0.360 *in*. The clamp faces are machined from 4340 steel hardened to about 45 on the Rockwell-C scale. In clamping, application of vertical forces that would cause bending and axial pulses, which could result in erroneous data, are avoided by allowing the clamp to move relative to the incident bar. This is accomplished by horizontal slots in the clamp face guides, as seen in Figure 2.9. In addition, the clamp faces are joined to the guides by pins, allowing the clamp faces to rotate relative to the guide, and hence further eliminating axial and bending pulses by establishing flush contact between the clamp faces and the incident bar.

A typical record of the shear strain pulses recorded with the strain gages at locations A and B (see Figure 2.2) can be found in Figure 2.11. The rise time from 10% to 90% of the maximum strain is determined from this data and subsequent tests to be range from $30 - 50$ μs. In this figure, it can be seen that the reflected

pulse, which will be shown to be proportional to the shear strain rate in the specimen, is essentially constant in magnitude while strain is being transmitted. In addition, since the transmitted pulse is shorter than the reflected pulse, the incident pulse is sufficiently long enough to strain the specimen to failure.

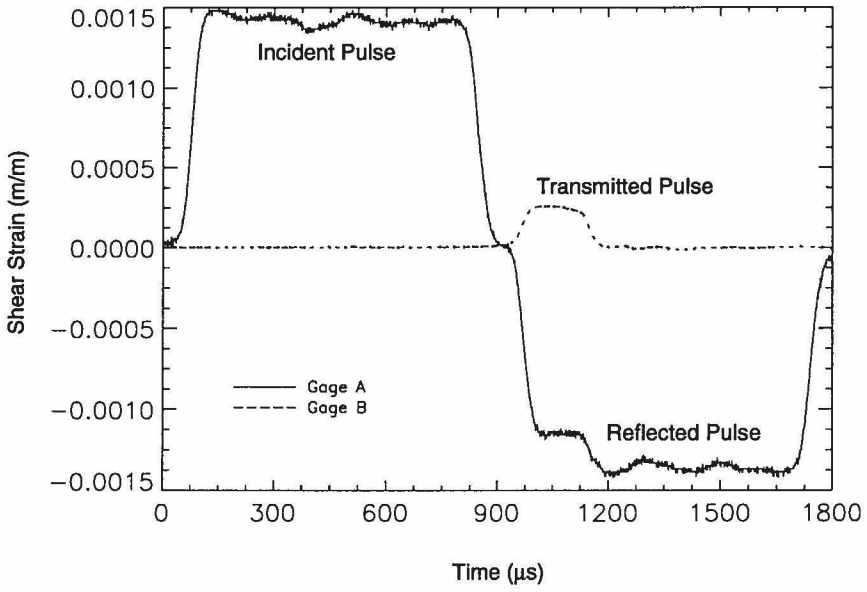

Figure 2.11: Typical shear strain pulses in a TSHB for 1018 CRS (Test 4).

2.2 Theory of One Dimensional Elastic Wave Propagation

This section describes the elastic torsion of a circular member. Popov (1990) states two assumptions which are necessary in understanding the relationship between torque and stress in a circular or tubular member. First, a planar section of material, which is perpendicular to the axis of a circular bar, remains planar after application of a torque. Second, shear strains are linearly increasing from the central axis, reaching a maximum at the exterior surface. Consequently, a radius of the bar that were scribed on the cross-section would remain straight after the member were torqued. In elastic

torsion of a rod, a constitutive theory stating that shear stress is proportional to shear strain is often assumed. This theory will be discussed later. Thus, in combination with Popov's second assumption, it is determined that the shear stress varies linearly with the radius of the rod.

Referring to Figure 2.12, the torque in the axial direction, T_z, in a circular rod or tube is defined as the equivalent moment generated by the shear stress, τ, over

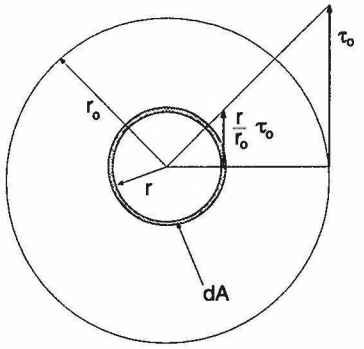

Figure 2.12: Shear stress in a rod elastically loaded in torsion.

the cross-sectional area, A, of a member. A moment is a force acting over a distance; hence, the torque in a rod is the area integral of the shear stress times the radius, r:

$$\begin{aligned} T_z &= \int_A \tau\, r\, dA = \int_A \frac{r}{r_0}\tau_0\, r\, dA\,, \\ &= \frac{\tau_0}{r_0}\int_A r^2 dA\,, \end{aligned} \tag{2.1}$$

where r_0 is the outer radius of the bar, and τ_0 is the corresponding shear stress. The polar moment of inertia, J, is defined as:

$$J = \int_A r^2 dA\,, \tag{2.2}$$

and it is constant over a particular cross-section. The polar moment of inertia for a

circular rod and for a thin walled tube are, respectively [Popov, 1990]:

$$J_{rod} = \frac{\pi r_0^4}{2} , \qquad J_{tube} \approx 2\pi r_{av}^3 t_w , \tag{2.3}$$

where r_{av} is the average radius of the tube, and $t_w \ll 1$ is the wall thickness of the tube. By substituting Equation (2.2) into Equation (2.1), one derives the torsion formula:

$$\tau_0 = \frac{T_z r_0}{J} . \tag{2.4}$$

Now, Figure 2.13 depicts a shaded region in an undeformed element of the bar. As a result of Popov's assumptions, radius OD remains straight and within the same perpendicular plane. After application of the torque, OD rotates through an angle

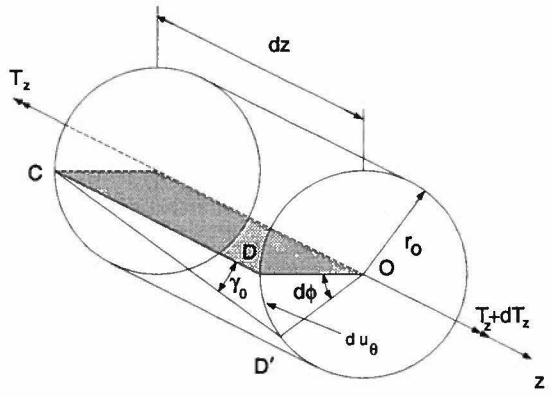

Figure 2.13: An element of a cylindrical bar deformed in torsion.

$d\phi$ to the position OD'. From geometry, there are two expressions for the arc length $|DD'|$, also known as the differential circumferential displacement, du_θ:

$$du_\theta = \gamma_0 dz = r_0 d\phi , \tag{2.5}$$

where γ_0 which is the angle spanning du_θ, is defined as the shear strain and ϕ is the angle of rotation of the bar. Integrating Equation (2.5) gives the following expression

for the circumferential displacement, u_θ:

$$u_\theta = r_0 \phi \ . \tag{2.6}$$

As the element $dz \rightarrow 0$, Equation (2.5), also gives expressions for the shear strain:

$$\gamma_0 = r_0 \frac{\partial \phi}{\partial z} = \frac{\partial u_\theta}{\partial z} \ . \tag{2.7}$$

One now assumes the constitutive relationship relating shear stress to shear strain, known as Hooke's law:

$$\tau_0 = G \gamma_0 \ . \tag{2.8}$$

Combining Equations (2.4), (2.7), and (2.8) yields:

$$T_z = JG \frac{\partial \phi}{\partial z} \ . \tag{2.9}$$

The governing equation used in torsional analysis is the conservation of angular momentum, which states:

$$\Sigma M = I \frac{\partial^2 \phi}{\partial t^2} \ , \tag{2.10}$$

where M are the moments, and I is the mass moment of inertia:

$$I = \int \left(x^2 + y^2 \right) dm \ , \tag{2.11}$$

where x and y are the Cartesian coordinates defining the plane perpendicular to the axis of rotation and m is the mass. If this expression is transformed into polar coordinates by using $x = r \cos \phi$ and $y = r \sin \phi$, and knowing that $dm = \rho dA dz$, where ρ is the density, one finds:

$$I = \rho \ dz \int_A r^2 dA = \rho J dz \ . \tag{2.12}$$

Equation (2.10), with Equation (2.12), is now invoked on the element in Figure 2.13 to yield:

$$[(T_z + dT_z) - T_z] = \rho J dz \frac{\partial^2 \phi}{\partial t^2} \,. \tag{2.13}$$

As $dz \to 0$, this equation reduces to the following:

$$\frac{\partial T_z}{\partial z} = \rho J \frac{\partial^2 \phi}{\partial t^2} \,. \tag{2.14}$$

In order to understand the analysis of shear pulses in a TSHB, it is first necessary to address the dynamics of one dimensional wave propagation in bars, including reflection of the waves at fixed ends and free ends. By substituting Equation (2.9) into Equation (2.14) one obtains:

$$\frac{\partial^2 \phi}{\partial z^2} = \frac{1}{c^2} \frac{\partial^2 \phi}{\partial t^2}, \tag{2.15}$$

where c is defined as follows:

$$c = \sqrt{\frac{G}{\rho}} \,. \tag{2.16}$$

Equation (2.15) is recognized as a linear wave equation with a solution, which can be verified by substitution, known as D'Alembert's solution:

$$\phi = f(z + ct) + g(z - ct), \tag{2.17}$$

where f and g are any arbitrary functions. D'Alembert's solution describes the propagation of a right and left traveling wave, represented by g and f, respectively. It can be easily shown that c is the wave speed of the propagating disturbance. If a torsional pulse were stored in a bar between two clamps, which were simultaneously released, Equation (2.17) predicts that two pulses would propagate in opposite directions (see

Figure 2.14). Symmetry tells us that these pulses would be equal in length to the stored pulse and half of its magnitude.

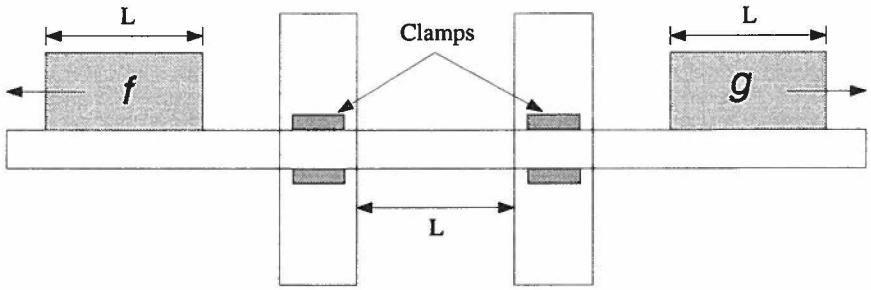

Figure 2.14: Wave Propagation in a Bar

In order to understand the reflection of torsional waves in a circular bar, it is first necessary to determine the relationship between the circumferential velocity, v_θ, and the shear stress, τ_0. One next inserts Equation (2.17) into Equation (2.6) and differentiates with respect to time to find v_θ:

$$v_\theta = r_0 c \left(f' - g'\right) \ , \tag{2.18}$$

where the primes denote differentiation with respect to $(x + ct)$ for f and $(x - ct)$ for g. By applying Equation (2.8) to Equation (2.7) and substituting in from Equation (2.17), one determines:

$$\tau_0 = r_0 G \left(f' + g'\right), \tag{2.19}$$

Now, for a right traveling wave, $f = 0$, and for a left traveling wave, $g = 0$. Equations (2.18) and (2.19) thus reduce to:

$$v_\theta = \begin{cases} +r_0 c f' & \text{left traveling} \\ -r_0 c g' & \text{right traveling} \end{cases} \tag{2.20}$$

$$\tau_0 = \begin{cases} r_0 G f' & \text{left traveling} \\ r_0 G g' & \text{right traveling} \end{cases} . \tag{2.21}$$

Combining Equations (2.20) and (2.21) yields:

$$\tau_0 = \pm \rho c v_\theta \ , \tag{2.22}$$

where the positive sign is for left traveling waves and the negative for right traveling waves.

Now consider transmission through a material interface. At the interface, one must enforce the kinematic condition of velocity continuity and the dynamic condition of a torque balance. Referring to Figure 2.15, it is seen that bar 1 contains both the incident and reflected pulses, while bar 2 contains the transmitted pulse. These pulses

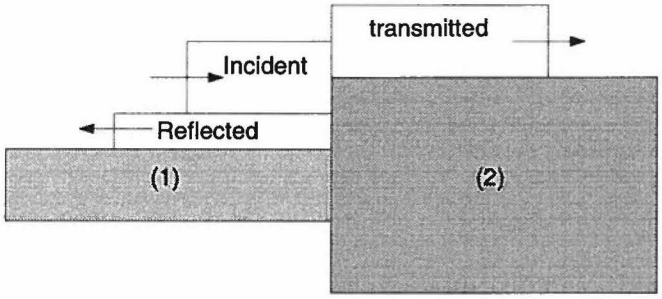

Figure 2.15: Schematic of the reflections of waves in one dimensional bars.

will be referred to with the subscripts "I," "R," and "T," respectively, and material properties will be referred to with subscripts 1 and 2, denoting the bar which they describe. Hence, the torque balance yields:

$$(\tau_I + \tau_R)\frac{J_1}{r_1} = \tau_T \frac{J_2}{r_2} \ , \tag{2.23}$$

and velocity continuity yields

$$v_{\theta I} + v_{\theta R} = v_{\theta T}. \tag{2.24}$$

By applying Equation (2.22), Equation (2.24) becomes:

$$\frac{\tau_R - \tau_I}{\rho_1 c_1} = \frac{-\tau_T}{\rho_2 c_2}. \tag{2.25}$$

Solving Equations (2.23) and (2.25) yields the reflected and transmitted stresses as functions of the incident stress:

$$\tau_T = \frac{2J_1 r_2 \rho_2 c_2}{J_2 r_1 \rho_2 c_2 + J_1 r_2 \rho_1 c_1} \tau_I \tag{2.26}$$

$$\tau_R = \frac{J_2 r_1 \rho_2 c_2 - J_1 r_2 \rho_1 c_1}{J_2 r_1 \rho_2 c_2 + J_1 r_2 \rho_1 c_1} \tau_I. \tag{2.27}$$

There are two limiting cases of these equations which have significance in this thesis. The first case is the reflection at a free end. At a free end, $\rho_2 \to 0$, and hence:

$$\tau_T = 0 \tag{2.28}$$

$$\tau_R = -\tau_I. \tag{2.29}$$

The second case is the reflection at a fixed end. At a fixed end, $J_2 \to \infty$, thus:

$$\tau_T = 0 \tag{2.30}$$

$$\tau_R = \tau_I. \tag{2.31}$$

For the TSHB, the release of the clamp causes right and left traveling torsional pulses. The pulley acts as a rigid wall and immediately reflects the left traveling pulse without changing its sign, joining it with the right traveling pulse. The result is a right traveling pulse of length equal to twice the stored pulse and half the magnitude.

2.3 Analysis

The values of the shear stress, shear strain and shear strain rate experienced in the specimen, when homogeneous deformation in the specimen is assumed, are

determined from an analysis of the strain in the incident and transmission bars. The subscript, s, is used to denote the properties of the specimen. The shear strain rate in the specimen, $\dot{\gamma}_s$, is proportional to the reflected strain in the incident bar, as will be shown. Integration of the shear strain rate then provides the shear strain in the specimen, γ_s.

Assuming that the shear strain is constant throughout the specimen, one can use Equation (2.7) to integrate along the length of the specimen to determine the nominal, or average, shear strain:

$$\gamma_s = \frac{D_s\,(\phi_2 - \phi_1)}{2L_s}, \tag{2.32}$$

where, referring to Figure 2.16, ϕ_1 is the angle of rotation of the specimen/incident bar interface and ϕ_2 is the angle of rotation of the specimen/transmission bar interface; D_s is the mean diameter of the specimen; and L_s is its length.

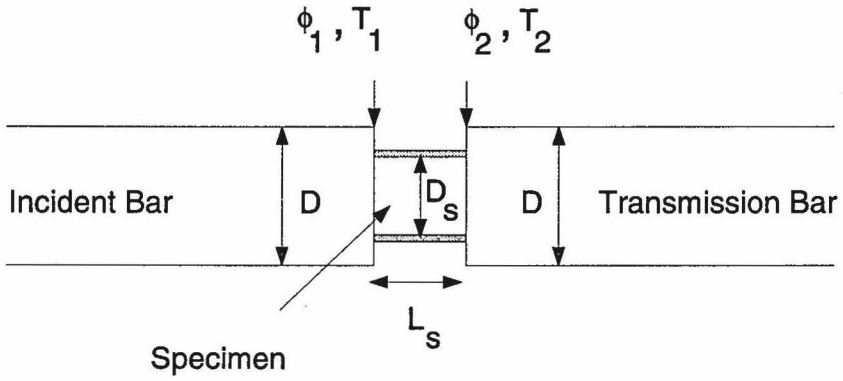

Figure 2.16: Schematic of the specimen-bar interface.

One next seeks expressions for ϕ_1 and ϕ_2 in terms of measurable quantities. Equation (2.7) can be applied to the transmission bar:

$$\gamma_T = \frac{D}{2}\frac{\partial \phi_2}{\partial z}\,, \tag{2.33}$$

where γ_T is the shear strain on the surface of the transmission bar, and D is the diameter of the bar. By performing integrations with respect to time and space on D'Alembert's solution, Equation (2.17), for a right traveling wave, it is seen that:

$$\frac{\partial \phi}{\partial t} = -cg' , \tag{2.34}$$

$$\frac{\partial \phi}{\partial z} = g' . \tag{2.35}$$

From these equations, one determines:

$$\frac{\partial \phi}{\partial t} = -c\frac{\partial \phi}{\partial z} , \tag{2.36}$$

for a right traveling wave. Substituting into Equation (2.33), one finds:

$$\gamma_T = -\frac{D}{2c}\frac{\partial \phi_2}{\partial t} . \tag{2.37}$$

Equation (2.37) is then integrated to determine ϕ_2:

$$\phi_2 = -\frac{2c}{D}\int_0^t \gamma_T\left(\tilde{t}\right)\, d\tilde{t} , \tag{2.38}$$

where $\tilde{t}$ is a dummy variable of integration. In a similar manner, ϕ_1 is determined from the shear strain on the surface of the incident bar at the specimen interface; composed of the right traveling incident strain pulse, $\gamma_I(t)$, and the left traveling reflected strain pulse, $\gamma_R(t)$. Hence,

$$\phi_1 = -\frac{2c}{D}\int_0^t \left[\gamma_I\left(\tilde{t}\right) - \gamma_R\left(\tilde{t}\right)\right]\, d\tilde{t}. \tag{2.39}$$

Equations (2.38) and (2.39) are then substituted into Equation (2.32) to yield:

$$\gamma_s(t) = -\frac{cD_s}{L_s D}\int_0^t \left(\gamma_T\left(\tilde{t}\right) - \left[\gamma_I\left(\tilde{t}\right) - \gamma_R\left(\tilde{t}\right)\right]\right)\, d\tilde{t}. \tag{2.40}$$

Now, for a homogeneous state of strain in the specimen, the torque at the specimen/incident bar interface, T_1, is approximately equal to the torque at the specimen/transmission bar interface, T_2. Since torque is proportional to shear strain during deformation of the bar, the strains at either side of the specimen, are approximately equal:

$$\gamma_T \approx \gamma_I + \gamma_R. \tag{2.41}$$

This relation is then substituted into Equation (2.40) to obtain the expression for the shear strain in the specimen:

$$\gamma_s(t) = -\frac{2cD_s}{L_s D}\int_0^t \gamma_R\left(\tilde{t}\right)\, d\tilde{t}. \tag{2.42}$$

It can also be shown that the transmitted pulse provides a measure of the shear stress in the specimen, τ_s. Equation (2.4) is applied to the specimen and, after substituting in from Equation (2.3) for a thin walled tube, one obtains the following expression for the shear stress in the specimen:

$$\tau_s = \frac{2T_s}{\pi D_s^2 t_s}, \tag{2.43}$$

where T_s is the average torque in the specimen and t_s is the wall thickness of the specimen. The average torque in the specimen can be determined from the average of the torque at the two bar/specimen interfaces:

$$T_s = \frac{T_1 + T_2}{2}\ . \tag{2.44}$$

One next applies Equation (2.4) to the incident and transmission bars and substitutes in from Equation (2.8) and (2.3), to determine these torques:

$$T_1 \ = \ \frac{G\pi D^3}{16}\left(\gamma_I + \gamma_R\right)\ , \tag{2.45}$$

$$T_2 = \frac{G\pi D^3}{16}\gamma_T \,. \tag{2.46}$$

From Equations (2.41), and (2.43) – (2.46), one obtains the final expression for the shear stress in the specimen:

$$\tau_s = \frac{GD^3}{8D_s^2 t_s}\gamma_T. \tag{2.47}$$

2.4 Data Acquisition and Reduction

The shear strain pulses in the incident and transmission bars are recorded by means of electric resistance strain gage Wheatstone bridges, which are extremely sensitive to small changes in strain. The strain gages are attached at the midpoints of each bar, location A and B in Figure 2.2. With the gages mounted at the midpoint of the bar, it is possible to record a pulse without its reflection overlapping in time, as long as the pulse is shorter than the length of the bar. Since the clamp is mounted between the torsional pulley and gage station A, the incident pulse, being twice as long as the stored torque, will always be less than the length of the bar. In addition, since gages A and B are each the same distance from the specimen, it is ensured that the reflected and transmitted pulse will commence at approximately the same instant in time. There is also a strain gage bridge mounted 12 *in* from the torsional pulley, gage station C in Figure 2.2. The purpose for this gage is to record the stored torque, which is used to obtain the expected strain rate incident upon the specimen. Stations A and B consist of four strain gages; one set of 2 torque gages is mounted diametrically opposite another set on the surface of the bar. Each gage is mounted at a 45° angle to the axis of the bar. Strain gages mounted this way will record only

shear strain, cancelling any axial and bending strain which may be present. Gage station C consists of one set of strain gages, also mounted at a 45° angle to the axis of the bar.

A Wheatstone bridge is diagramed in Figure 2.17, where V is the excitation voltage, E_0 is the output voltage, and R_1, R_2, R_3, and R_4 are resistors or strain gages. McConnell and Filey (1993) determine the following equation which calculates the shear strain from the bridge output voltage:

$$\gamma_0 = \frac{2\Delta E_0}{FVG_aN_g}\frac{(1+\kappa)^2}{\kappa}\ , \tag{2.48}$$

where F is the gage factor, G_a is the amplifier gain, N_g is the number of active gages in the Wheatstone bridge, and $\kappa = \frac{R_2}{R_1} = \frac{R_4}{R_3}$ is the ratio of resistance.

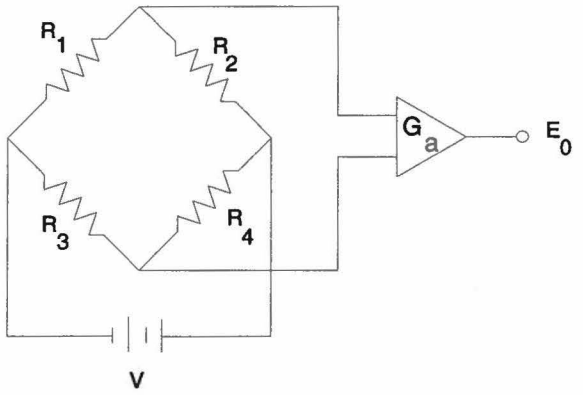

Figure 2.17: Schematic of a Wheatstone bridge circuit.

Each bridge is wired to a Measurements Group model 2311 signal conditioning amplifier, which sets the excitation voltage and gain. The amplifier output from gage station A is split, with one lead, as well as the amplifier output from gage station B, sent to a Tektronix model TDS 420 digitizing oscilloscope, which is downloaded to a personal computer. This data is reduced by Equations (2.48), (2.42), and (2.47), to

determine nominal shear stress and shear strain characteristics of the specimen. The other lead of the amplifier output from gage station A is sent to a Hewlett Packard model 214A pulse generator. The incident pulse triggers the pulse generator, which sends a second pulse, delayed by some specified time, to trigger a Cordin model 607 light source, which illuminates the deformation of the specimen. Photographs of this process, which are used to determine the failure mechanism of the specimen, are recorded with a Cordin model 330A ultra-high speed camera.

2.5 Verification of the TSHB

In order to verify the operation of the TSHB, tests were performed with 1018 cold rolled steel (CRS), a material which has been tested with the TSHB by a number of researchers [Clifton *et al.* (1984), Hartley *et al.* (1987), and Duffy and Chi (1992)]. Duffy and Chi used a smooth variation in the wall thickness of the specimen's gage length as a function of its length, with the value at the center 14.9% less than that at the edges. The specimens used in this thesis had the same variation in wall thickness, except that the thickness at the center was 10% less than at the edge. Figure 2.18 shows a comparison of the results obtained by Duffy and Chi with those determined in this thesis.

The differences in these plots can be attributed to a number of reasons. It is first noticed that there is a significant difference in the slope of the shear stress-shear strain curve prior to yielding of the material. Hartley *et al.* (1985) performed a theoretical quasi-static analysis on the torsional deformation of a thin-walled tube. They concluded that upon application of torque, it would take several reflections

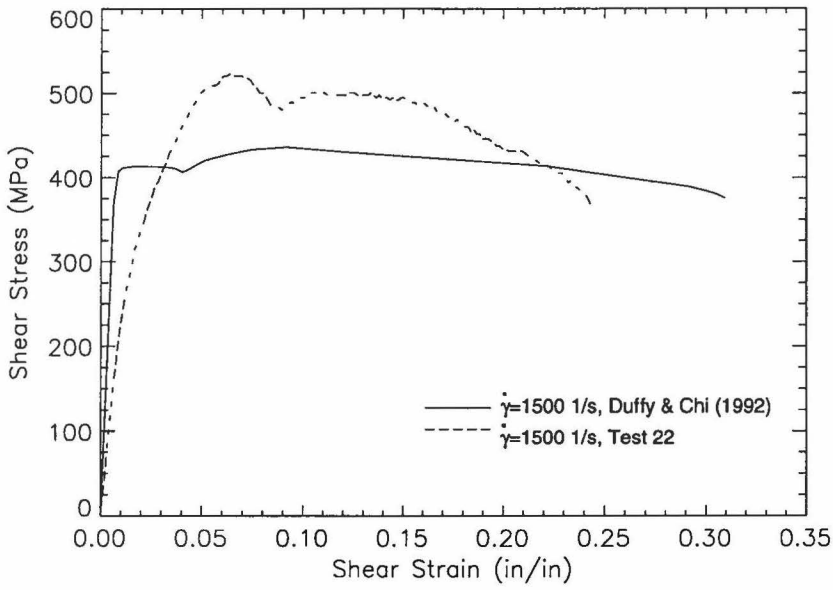

Figure 2.18: Comparison of current TSHB results for 1018 CRS with those from Duffy and Chi (1992).

of the incident pulse from the ends of the specimen gage length before a state of homogeneous deformation is reached. If deformation is initially inhomogeneous, some of the material may be deforming plastically while the rest is deforming elastically. Furthermore, the slope of the shear stress-shear strain curve is significantly lower for plastic deformation, as can be seen by the decrease in slope at higher strains in Figure 4.7. Hence, the initial slope, being an average of elastic and plastic straining, could be significantly lower than that expected for elastic deformation. If the incident and transmitted bars are slightly warped or not perfectly aligned, this inhomogeneous deformation could be increased, causing a further decrease in the initial slope. From observation of the bars, it was noticed that they are slightly warped. In addition, in dynamic deformation, Popov's (1990) second assumption that shear strains in torsion are linearly increasing from the central axis of the bar (see Section 2.2), may not be valid. Strains could have higher order variations along the radius, which would result

in a dispersive pulse, whereas a first order variation is nondispersive. Dispersion effects would cause further decreases in the initial shear stress-shear strain slope. Furthermore, the effect of the rise time of the incident pulse is undetermined and could also result in a decrease in the initial slope. Finally, the attachment of the specimen to the bars may not be secure enough. This would cause slipping in the gripping mechanism, which would result in a decrease in the initial slope.

The differences in the maximum shear stress and shear strain at failure may also be attributed to a number of reasons. First, the exact heat treatment of the steel used by Duffy and Chi is unknown. Changes in the heat treatment can cause microstructural differences in the materials and hence significantly alter the material characteristics, as will be shown in Section 4.2.1. Also, the thickness variation in the tests reported in Figure 2.18 are slightly different. Duffy and Chi have shown that this parameter has an effect on the maximum shear stress and shear strain at failure. Finally, preliminary tests performed with different strain gages mounted on the transmission bar have resulted in transmitted strains 7-8% less in magnitude. It is thus thought that the current strain gages may have been poorly mounted.

Other sources of error come from data acquisition. The oscilloscope used in this research has an error of 0.8% of its full scale resolution. The voltmeter has a resolution of $\pm 0.1\ mV$, and the error of the amplifier is as yet undetermined. Since all sources of error are not fully quantified, the exact error of the TSHB is indeterminate at this time, however, it is expected that results are accurate within 10%.

CHAPTER 3

MODEL EQUATIONS

This chapter introduces the model equations employed in this research. In the first section, the physical problem is described. The assumptions and governing equations are then presented. These equations are scaled and presented in nondimensional form. Finally, the numerical method used to solve the equations is discussed.

3.1 Governing Equations

The current theoretical study of localization is being used to compare with tests performed on the deformation of specimens in the TSHB. Tests have been performed on metals, solid explosive simulants and solid explosives. In the TSHB, a thin walled circular cylinder is dynamically loaded in torsion; the model is thus designed to simulate these conditions. A schematic of the specimen described by the model is included in Figure 3.1. In this specimen, which has length L_s, z is the axial distance variable, θ is the circumferential distance variable, and r is the radial distance variable. This specimen is loaded by linearly increasing the circumferential velocity, v_θ, over time, t, at $z = L_s$ to some constant value, v_1, while holding the velocity fixed at $z = 0$. The following assumptions are made in developing the model:

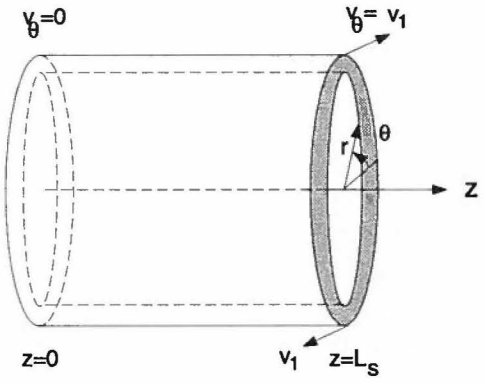

Figure 3.1: Specimen used for numerical simulation.

- The specimen is initially unreacted, unstressed, and at ambient temperature.

- As we are dealing with a pure torsional problem, there is no component of velocity or displacement in the radial or axial direction: $v_r = v_z = u_r = u_z = 0$.

- Due to axisymmetry and the thin walled geometry, there is no variation in the circumferential or radial direction: $\frac{\partial}{\partial \theta} = \frac{\partial}{\partial r} = 0$.

- In order to induce localization, we allow the specimen wall thickness to vary with axial position z. We make the *ad hoc* assumption that this perturbation is sufficiently small so as not to introduce gradients in the radial or circumferential directions. It is noted that alternative methods of perturbation which do not require such *ad hoc* assumptions, such as perturbation in initial velocity, temperature, displacement or strain, could also induce localization.

- In pure torsion, the stress tensor reduces to one component, $\sigma_{z\theta}$, the stress on the axial face in the circumferential direction, which will be referred to as the shear stress, τ.

- The shear strain is restricted to positive values.
- Plastic deformation is completely converted to heat.
- Heat is only transferred in the axial direction.
- The material undergoes a one-step chemical reaction, with A denoting the unreacted material, and B denoting the reacted material.
- The density, ρ, and the thermal conductivity, k, are equal in the unreacted and reacted material and, along with the specific heats, c_A and c_B, they are constant.

Under these assumptions, the governing equations are stated below:

$$\rho w \frac{\partial v_\theta}{\partial t} = \frac{\partial}{\partial z}(w\tau) \ , \tag{3.1}$$

$$\rho w \frac{\partial e}{\partial t} = w\tau \frac{\partial v_\theta}{\partial z} - \frac{\partial}{\partial z}(w q_z) \ , \tag{3.2}$$

$$\frac{\partial u_\theta}{\partial z} = \gamma \ , \tag{3.3}$$

$$\frac{\partial u_\theta}{\partial t} = v_\theta \ , \tag{3.4}$$

$$\frac{\partial \lambda}{\partial t} = Z(1-\lambda)\exp\left(-\frac{E}{RT}\right), \tag{3.5}$$

where e is the internal energy, q_z is the heat flux in the axial direction, u_θ is the displacement in the circumferential direction, γ is the shear strain, λ is the reaction progress variable, and T is the temperature. The parameters w, Z, E, and R are, respectively, the thickness of the specimen wall thickness, the kinetic rate constant, the reaction activation energy, and the universal gas constant. Equation (3.1) models the conservation of linear momentum. Equation (3.2) models the conservation of

energy. Equation (3.3) is the definition of strain. Equation (3.4) defines velocity as the time derivative of displacement. Finally, Equation (3.5) is an Arrhenius kinetics law.

The constitutive equations used in this model are:

$$\tau = \alpha\, T^{\nu}\, \gamma^{\eta} \left|\frac{\partial \gamma}{\partial t}\right|^{\mu-1} \frac{\partial \gamma}{\partial t}\,, \tag{3.6}$$

$$q_z = -k\frac{\partial T}{\partial z}\,, \tag{3.7}$$

$$e = m_A e_A + m_B e_B\,, \tag{3.8}$$

$$e_A = c_A T + e_A^o\,, \tag{3.9}$$

$$e_B = c_B T + e_B^o\,, \tag{3.10}$$

$$m_A = 1 - \lambda\,, \tag{3.11}$$

$$m_B = \lambda\,, \tag{3.12}$$

where α is the stress constant; subscripts A and B refer to the unreacted and reacted material, respectively; e_A and e_B are the internal energies; m_A and m_B are the mass fractions; c_A and c_B are the specific heats; and e_A° and e_B° are the energies of formation. Equation (3.6) is a constitutive law for stress, proposed by Clifton, *et al.* (1984) where ν, η, and μ are the exponents which characterize the thermal softening, the strain and strain rate hardening, respectively. Equation (3.7) is Fourier's law of heat conduction. Equation (3.8) is a mixture law. Equations (3.9) and (3.10) are the constitutive laws for energy. Lastly, Equations (3.11) and (3.12) define the mass fractions.

The following boundary conditions are used in this model:

$$v_\theta(t,0) = 0\,, \qquad v_\theta(t,L_s) = \begin{cases} (v_1 - v_0)\frac{t}{t_1} + v_0 & t < t_1 \\ v_1 & t \geq t_1 \end{cases}$$

$$u_\theta(t,0) = 0\ , \quad u_\theta(t,L_s) = \begin{cases} (v_1 - v_0)\frac{t^2}{2t_1} + v_0 t & t < t_1 \\ (v_1 - v_0)\frac{t_1}{2} + v_0 t_1 + v_1(t - t_1) & t \geq t_1 \end{cases} \tag{3.13}$$

$$\frac{\partial T}{\partial z}(t,0) = 0\ , \quad \frac{\partial T}{\partial z}(t,L_s) = 0 \qquad t \geq 0\ .$$

That is, v_θ is fixed at one side of the specimen and ramped over a time t_1 from some arbitrarily small velocity, v_0, to a constant value v_1. The boundary conditions on displacement are determined by integrating over time the boundary conditions on velocity. Finally, the boundary conditions on temperature are such that the ends of the specimen are insulated. The initial conditions are:

$$v_\theta(0,z) = v_0\frac{z}{L_s}\ , \qquad u_\theta(0,z) = 0\ , \qquad T(0,z) = T_0\ , \qquad \lambda(0,z) = 0, \tag{3.14}$$

where the velocity is initially sloped to v_0, and the specimen is initially stress free, unreacted and at a uniform temperature, T_0.

In order to induce localization at the center of the specimen, the thickness of the tube is perturbed so that it is thinner in the center than at the edges. The exact form of this perturbation is as follows:

$$w = w_0 - \frac{h_p}{2}\left[1 - \cos\left(\frac{2\pi z}{L_s}\right)\right]\ . \tag{3.15}$$

In this equation, h_p is the maximum decrease in the specimen wall. Figure 3.2 shows a plot of the thickness as a function of position with h_p/w_0 equaling 0.1.

Next, the governing equations are reduced through insertion of the constitutive laws. First, by differentiating Equation (3.3) with respect to time and Equation (3.4) with respect to space, and equating the results, one determines the following expres-

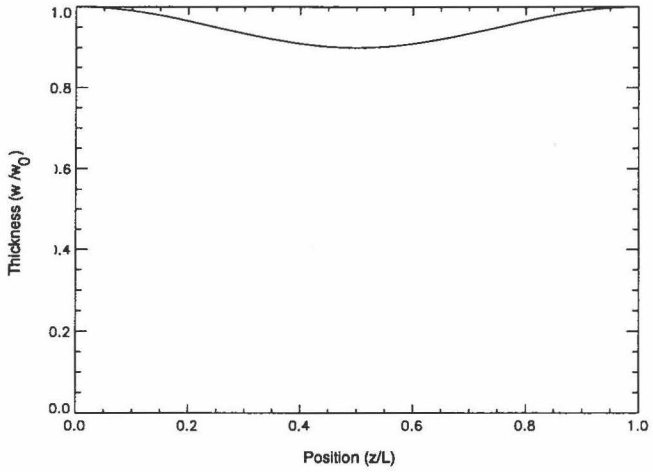

Figure 3.2: Initial perturbation in thickness.

sion relating shear strain rate with velocity gradient:

$$\frac{\partial \gamma}{\partial t} = \frac{\partial v_\theta}{\partial z}. \tag{3.16}$$

Now, Equations (3.3), (3.6), and (3.16), are inserted into the linear momentum equation, Equation (3.1). The energy equation, Equation (3.2), is reduced by substitution of Equations (3.5)–(3.10) and (3.16). Finally, Equations (3.4), (3.5) and (3.15) are restated:

$$\rho w \frac{\partial v_\theta}{\partial t} = \frac{\partial}{\partial z}\left[w\alpha\, T^\nu \left(\frac{\partial u_\theta}{\partial z}\right)^\eta \left|\frac{\partial v_\theta}{\partial z}\right|^{\mu-1} \frac{\partial v_\theta}{\partial z}\right], \tag{3.17}$$

$$\begin{aligned} \frac{\partial T}{\partial t} &= \frac{1}{\rho\left[c_A(1-\lambda)+c_B\lambda\right]}\left[\alpha T^\nu \left(\frac{\partial u_\theta}{\partial z}\right)^\eta \left|\frac{\partial v_\theta}{\partial z}\right|^{\mu+1} + \frac{k}{w}\frac{\partial}{\partial z}\left(w\frac{\partial T}{\partial z}\right)\right. \\ &+ \left. Z\,\rho\left[Q+(c_A-c_B)\,T\right](1-\lambda)\exp\left(-\frac{E}{RT}\right)\right], \end{aligned} \tag{3.18}$$

$$\frac{\partial u_\theta}{\partial t} = v_\theta\,, \tag{3.19}$$

$$\frac{\partial \lambda}{\partial t} = Z(1-\lambda)\exp\left(-\frac{E}{RT}\right), \tag{3.20}$$

$$w = w_0 - \frac{h_p}{2}\left[1-\cos\left(\frac{2\pi z}{L_s}\right)\right], \tag{3.21}$$

where $Q = e_A^o - e_B^o$ is the heat of reaction. One notes that these equations are of the following form:

$$\frac{\partial \tilde{y}}{\partial t} = \tilde{F}\left(\tilde{y}, \frac{\partial \tilde{y}}{\partial z}\right) , \tag{3.22}$$

where $\tilde{y}$ is a vector of unknowns and $\tilde{F}$ is a vector which is functionally dependent on $\tilde{y}$ and $\frac{\partial \tilde{y}}{\partial z}$.

3.2 Shear Localization Susceptibility

In order to numerically determine when localization begins, a localization criterion is developed. Zener and Hollomon (1944) stated that adiabatic shear bands typically initiate at a point after a maximum stress is reached in the shear stress-shear strain relationship for the material at that point. This can be stated symbolically as follows:

$$\left.\frac{\partial \tau}{\partial \gamma}\right|_{\tilde{x}} \leq 0 , \tag{3.23}$$

where $\tilde{x}$ is the vector representation of that point.

One now recalls that shear stress is a function of temperature, shear strain and shear strain rate, $\dot{\gamma} = \frac{\partial \gamma}{\partial t}$:

$$\tau = \tau\left(T, \gamma, \dot{\gamma}\right) . \tag{3.24}$$

Application of the chain rule to Equation (3.24) yields:

$$d\tau = \left.\frac{\partial \tau}{\partial T}\right|_{\gamma,\dot{\gamma}} dT + \left.\frac{\partial \tau}{\partial \gamma}\right|_{T,\dot{\gamma}} d\gamma + \left.\frac{\partial \tau}{\partial \dot{\gamma}}\right|_{T,\gamma} d\dot{\gamma} . \tag{3.25}$$

Now, since T, γ, and $\dot{\gamma}$ are functions of z and t, we can also state:

$$\tau = \tau\left(z, t\right) . \tag{3.26}$$

Application of the chain rule to Equation (3.26) then yields:

$$d\tau = \left.\frac{\partial \tau}{\partial t}\right|_z dt + \left.\frac{\partial \tau}{\partial z}\right|_t dz \ . \tag{3.27}$$

By equating Equations (3.27) and (3.25), and holding z constant, one obtains:

$$\left.\frac{\partial \tau}{\partial t}\right|_z = \left.\frac{\partial \tau}{\partial T}\right|_{\gamma,\dot{\gamma}} \left.\frac{\partial T}{\partial t}\right|_z + \left.\frac{\partial \tau}{\partial \gamma}\right|_{T,\dot{\gamma}} \left.\frac{\partial \gamma}{\partial t}\right|_z + \left.\frac{\partial \tau}{\partial \dot{\gamma}}\right|_{T,\gamma} \left.\frac{\partial \dot{\gamma}}{\partial t}\right|_z \ . \tag{3.28}$$

For adiabatic deformation and neglecting reaction, the conservation of energy principle, Equation (3.18), after inserting Equations (3.6) and (3.16) reduces to:

$$\rho c_A \left.\frac{\partial T}{\partial t}\right|_z = \tau \left.\frac{\partial \gamma}{\partial t}\right|_z \ . \tag{3.29}$$

One next inserts Equation (3.29) into Equation (3.28) to obtain:

$$\left.\frac{\partial \tau}{\partial t}\right|_z = \left.\frac{\partial \gamma}{\partial t}\right|_z \left(\frac{\tau}{\rho c_A} \left.\frac{\partial \tau}{\partial T}\right|_{\gamma,\dot{\gamma}} + \left.\frac{\partial \tau}{\partial \gamma}\right|_{T,\dot{\gamma}} \right) + \left.\frac{\partial \tau}{\partial \dot{\gamma}}\right|_{T,\gamma} \left.\frac{\partial \dot{\gamma}}{\partial t}\right|_z \ . \tag{3.30}$$

Rearranging this expression, one finds:

$$\frac{\partial \tau/\partial t|_z}{\partial \gamma/\partial t|_z} = \frac{\tau}{\rho c_A} \left.\frac{\partial \tau}{\partial T}\right|_{\gamma,\dot{\gamma}} + \left.\frac{\partial \tau}{\partial \gamma}\right|_{T,\dot{\gamma}} + \left.\frac{\partial \tau}{\partial \dot{\gamma}}\right|_{T,\gamma} \frac{\partial \dot{\gamma}/\partial t|_z}{\partial \gamma/\partial t|_z} \ , \tag{3.31}$$

which is equivalent to:

$$\left.\frac{\partial \tau}{\partial \gamma}\right|_z = \frac{\tau}{\rho c_A} \left.\frac{\partial \tau}{\partial T}\right|_{\gamma,\dot{\gamma}} + \left.\frac{\partial \tau}{\partial \gamma}\right|_{T,\dot{\gamma}} + \left.\frac{\partial \tau}{\partial \dot{\gamma}}\right|_{T,\gamma} \frac{\partial \dot{\gamma}/\partial t|_z}{\partial \gamma/\partial t|_z} \ . \tag{3.32}$$

Insertion of Equation (3.32) into Equation (3.23) and rearranging yields:

$$\left.\frac{\partial \tau}{\partial \gamma}\right|_{T,\dot{\gamma}} + \left.\frac{\partial \tau}{\partial \dot{\gamma}}\right|_{T,\gamma} \frac{\partial \dot{\gamma}/\partial t|_z}{\partial \gamma/\partial t|_z} \leq \frac{\tau}{\rho c_A} \left.\frac{\partial \tau}{\partial T}\right|_{\gamma,\dot{\gamma}} \ . \tag{3.33}$$

This expression may be used to determine shear localization susceptibility provided the strain and strain rate are monotonically increasing functions in time.

3.3 Nondimensionalization

In order to simplify the treatment of the governing equations, reduce the number of parameters, and identify relevant scales, the governing equations are nondimensionalized. The following nondimensional variables arise with these scales:

$$\begin{aligned} z^* &= \frac{z}{L_s}, \qquad t^* = \frac{v_1 t}{L_s}, \qquad u^* = \frac{u_\theta}{L_s}, \\ v^* &= \frac{v_\theta}{v_1}, \qquad T^* = \frac{T}{T_0}, \qquad w^* = \frac{w}{w_0}, \end{aligned} \tag{3.34}$$

where the *'s denote nondimensional variables. The following nondimensional parameters are used:

$$\begin{aligned} \hat{\alpha} &= \frac{\alpha T_0^\nu v_1^{\mu-2}}{\rho L_s^\mu}, \qquad \hat{c} = \frac{c_B}{c_A}, \qquad Ec = \frac{v_1^2}{c_A T_o}, \\ Pe &= \frac{c_A}{k}\rho v_1 L_s, \qquad \hat{Q} = \frac{Q}{c_A T_0}, \qquad \hat{Z} = \frac{Z L_s}{v_1}, \\ \hat{E} &= \frac{E}{RT_0}, \qquad \hat{h} = \frac{h_p}{2w_0}, \qquad \epsilon = \frac{v_0}{v_1}, \qquad \hat{t} = \frac{v_1 t_1}{L_s}, \end{aligned} \tag{3.35}$$

where $\hat{\alpha}$ is the nondimensional stress constant, $\hat{c}$ is the ratio of specific heats of the reacted and unreacted material, Ec is the Eckert number, Pe is the Peclet number, $\hat{Q}$ is the nondimensional heat of reaction, $\hat{Z}$ is the nondimensional kinetic rate constant, $\hat{E}$ is the nondimensional activation energy, $\hat{h}$ is the maximum nondimensional decrease in the specimen wall thickness, ϵ is the nondimensional initial velocity, and $\hat{t}$ is the nondimensional rise time. The parameters from Equations (3.34) and (3.35) are then inserted into Equations (3.17)–(3.21) to yield the following nondimensionalized system of equations:

$$\frac{\partial v^*}{\partial t^*} = \frac{\hat{\alpha}}{w^*}\frac{\partial}{\partial z^*}\left[w^*\ (T^*)^\nu \left(\frac{\partial u^*}{\partial z^*}\right)^\eta \left(\left|\frac{\partial v^*}{\partial z^*}\right|\right)^{\mu-1}\frac{\partial v^*}{\partial z^*}\right], \tag{3.36}$$

$$\frac{\partial T^*}{\partial t^*} = \frac{1}{(1-\lambda)+\hat{c}\lambda}\left[\hat{\alpha}Ec\,(T^*)^\nu \left(\frac{\partial u^*}{\partial z^*}\right)^\eta \left(\left|\frac{\partial v^*}{\partial z^*}\right|\right)^{\mu+1} + \frac{1}{w^*Pe}\frac{\partial}{\partial z^*}\left(w^*\frac{\partial T^*}{\partial z^*}\right)\right.$$
$$\left. + \hat{Z}\left[\hat{Q}+(1-\hat{c})\,T^*\right](1-\lambda)\exp\left(-\frac{\hat{E}}{T^*}\right)\right], \tag{3.37}$$

$$\frac{\partial u^*}{\partial t^*} = v^*, \tag{3.38}$$

$$\frac{\partial \lambda}{\partial t^*} = \hat{Z}\,(1-\lambda)\exp\left(-\frac{\hat{E}}{T^*}\right). \tag{3.39}$$

$$w^* = 1-\hat{h}\left[1-\cos\left(2\pi z^*\right)\right], \tag{3.40}$$

The boundary conditions in nondimensional form are listed below:

$$v^*(t^*,0)=0 \qquad v^*(t^*,1) = \begin{cases} (1-\epsilon)\frac{t^*}{\hat{t}}+\epsilon & t^*<\hat{t} \\ 1 & t^*\geq\hat{t} \end{cases}$$

$$u^*(t^*,0)=0 \qquad u^*(t^*,1) = \begin{cases} (1-\epsilon)\frac{t^{*2}}{2\hat{t}}+\epsilon t^* & t^*<\hat{t} \\ (1-\epsilon)\frac{\hat{t}}{2}+\epsilon\hat{t}+\left(t^*-\hat{t}\right) & t^*\geq\hat{t} \end{cases} \tag{3.41}$$

$$\frac{\partial T^*}{\partial z^*}(t^*,0)=0 \qquad \frac{\partial T^*}{\partial z^*}(t^*,1) = 0 \qquad t^*\geq 0\,.$$

The scaled initial conditions are:

$$u^*(0,z^*)=0\,, \qquad v^*(0,z^*)=\epsilon z^*\,, \qquad T^*(0,z^*)=1\,, \qquad \lambda(0,z^*)=0\,. \tag{3.42}$$

3.4 Solution Procedure

In order to solve the final system of equations numerically, a spatial discretization is performed using second order central differences. The result is a system of ordinary differential equations in time:

$$\frac{dv_i^*}{dt^*} = \frac{\hat{\alpha}}{w_i^* \Delta z^*} \left[\frac{w_{i+1}^* + w_i^*}{2} \left(\frac{T_{i+1}^* + T_i^*}{2} \right)^{\nu} \left(\frac{u_{i+1}^* - u_i^*}{\Delta z^*} \right)^{\eta} \left(\left| \frac{v_{i+1}^* - v_i^*}{\Delta z^*} \right| \right)^{\mu-1} \frac{v_{i+1}^* - v_i^*}{\Delta z^*} \right.$$
$$\left. - \frac{w_i^* + w_{i-1}^*}{2} \left(\frac{T_i^* + T_{i-1}^*}{2} \right)^{\nu} \left(\frac{u_i^* - u_{i-1}^*}{\Delta z^*} \right)^{\eta} \left(\left| \frac{v_i^* - v_{i-1}^*}{\Delta z^*} \right| \right)^{\mu-1} \frac{v_i^* - v_{i-1}^*}{\Delta z^*} \right] , \quad (3.43)$$

$$\frac{dT_i^*}{dt^*} = \frac{1}{(1-\lambda_i) + \hat{c}\lambda_i} \left[\hat{\alpha} Ec \left(T_i^* \right)^{\nu} \left(\frac{u_{i+1}^* - u_{i-1}^*}{2\Delta z^*} \right)^{\eta} \left(\left| \frac{v_{i+1}^* - v_{i-1}^*}{2\Delta z^*} \right| \right)^{\mu+1} \right.$$
$$+ \frac{1}{Pe} \left(\frac{T_{i+1}^* - 2T_i^* + T_{i-1}^*}{\Delta z^{*2}} + \frac{w_{i+1}^* - w_{i-1}^*}{2w_i^* \Delta z^*} \frac{T_{i+1}^* - T_{i-1}^*}{2\Delta z^*} \right) \quad (3.44)$$
$$\left. + \hat{Z} \left[\hat{Q} + (1 - \hat{c}) T_i^* \right] (1 - \lambda_i) \exp \left(-\frac{\hat{E}}{T_i^*} \right) \right] ,$$

$$\frac{du_i^*}{dt^*} = v_i^* , \quad (3.45)$$

$$\frac{d\lambda_i}{dt^*} = \hat{Z} (1 - \lambda_i) \exp \left(-\frac{\hat{E}}{T_i^*} \right) , \quad (3.46)$$

$$w_i^* = 1 - \hat{h} \left[1 - \cos \left(2\pi z_i^* \right) \right] . \quad (3.47)$$

As the character of this system is parabolic (see the Appendix), the computer code LSODE [Hindmarsh, 1983], the Livermore Solver for Ordinary Differential Equations, was used to step forward in time to solve this system. LSODE solves initial value problems for stiff or nonstiff systems of first order ordinary differential equations using the Gear (1971) method. A stiff system is one whose ratio of largest to smallest eigenvalues in the locally linearized solution matrix is large. That is, the system has rapidly growing or decaying processes that occur over a time scale much shorter than the overall time scale of interest. This computer code is thus desirable for the model presented herein since the process of shear localization occurs over a much shorter time than the overall time of interest. The Gear method uses backward differencing to solve systems of the form:

$$\frac{\partial \tilde{y}}{\partial t} = \tilde{F} \left(t, \tilde{y} \right) , \quad (3.48)$$

which is the form of Equations (3.43)-(3.47). For further details on the operation of LSODE, see Hindmarsh (1983).

3.5 Code Verification

In order to validate that the numerical method is implemented correctly and to determine its accuracy, several simplifications of the model equations are presented which have exact solutions. To find an exact solution, the effect of thermal softening is removed from the constitutive law for stress, so that the linear momentum and displacement equations will become decoupled from the energy equation. This is achieved by setting $\nu = 0$ in the constitutive law for stress. In addition, reaction is neglected by setting $\hat{Z} = 0$. Equation (3.39) is consequently solved to yield $\lambda = 0$. It is also taken that $\hat{c} = 1$. Finally, the perturbation in thickness is removed by setting $\hat{h} = 1$. The system of equations, Equations (3.36)–(3.40) thus reduces to:

$$\frac{\partial v^*}{\partial t^*} = \hat{\alpha}\frac{\partial}{\partial z^*}\left[\left(\frac{\partial u^*}{\partial z^*}\right)^{\eta}\left(\left|\frac{\partial v^*}{\partial z^*}\right|\right)^{\mu-1}\frac{\partial v^*}{\partial z^*}\right], \tag{3.49}$$

$$\frac{\partial T^*}{\partial t^*} = \hat{\alpha}Ec\left(\frac{\partial u^*}{\partial z^*}\right)^{\eta}\left(\left|\frac{\partial v^*}{\partial z^*}\right|\right)^{\mu+1} + \frac{1}{Pe}\frac{\partial^2 T^*}{\partial z^{*2}}, \tag{3.50}$$

$$\frac{\partial u^*}{\partial t^*} = v^*. \tag{3.51}$$

Through the specification of the boundary conditions, initial conditions and parameter values, three exact solutions to these equations are presented. The values of the parameters used in the proceeding calculations are found in Table 3.1.

α $(MPa \cdot s^{\mu})$	ρ (kg/m^3)	c_A $(J/kg \cdot K)$	k $(W/m \cdot K)$	T_0 (K)	v_1 (m/s)	L_s (mm)
700	7750	477	40	298	6.35	2.5

Table 3.1: Physical constants used in the test cases in Section 3.5.

3.5.1 Test Case 1: Stokes' First Problem

When one sets $\eta = 0$, and $\mu = 1$, a further simplified form of the linear momentum equation, which has an exact solution, known as Stokes' first problem. Equation (3.49) consequently reduces to:

$$\frac{\partial v^*}{\partial t^*} = \hat{\alpha} \frac{\partial^2 v^*}{\partial z^{*2}} \ . \tag{3.52}$$

Stokes' first problem has an exact solution for the velocity profile over a semi-infinite region when an initially motionless material is given a constant velocity boundary condition at one end. In the current formulation, it is necessary to provide an initial condition and boundary conditions on either side of the specimen, hence:

$$v^*(z^*, 0) = 0 \ , \qquad v^*(0, t^*) = 0 \ , \qquad v^*(1, t^*) = 1 \ . \tag{3.53}$$

Since Stokes' problem provides a solution over a semi-infinite domain, the current numerical method is always in error, however, it will yield an accurate solution up to the time when velocity diffusion causes the velocity to reach a significant value at $z^* = 0$. The solution to Equation (3.52), with the conditions $v^*(z^*, 0) = 0$ and $v^*(1, t^*) = 1$, is [Currie, 1993]:

$$v^* = 1 - \operatorname{erf}\left(\frac{1 - z^*}{2\sqrt{\hat{\alpha} t^*}}\right) \ . \tag{3.54}$$

The L_2 norm is a method of measuring the error in a numerical method. The norm is calculated from the following equation:

$$||v_n^* - v_e^*||_{L_2} = \frac{\sqrt{\sum_{i=1}^{N} \left(v_n^{*i} - v_e^{*i}\right)^2}}{N}, \tag{3.55}$$

where v_e^* is the exact solution, v_n^* is the numerically determined solution, the superscripts i refer to specific spatial values, and N is the number of spatial increments. In order to determine the rate of convergence of a numerical method, the L_2 norm can be plotted against the spatial increment, $1/N$, on a log-log plot, with the slope equaling the order of accuracy of the numerical method.

Stokes' problem is then solved numerically with the code described in the previous section; a comparison of the exact and numerically determined solutions can be found for $t^* = 1.5 \times 10^{-10}$, 2.5×10^{-9}, and 7.5×10^{-9} in Figure 3.3, for $\Delta z^* = 0.02$. At $t^* = 2.5 \times 10^{-10}$, the L_2 norm is computed for various Δz^*'s and the rate of

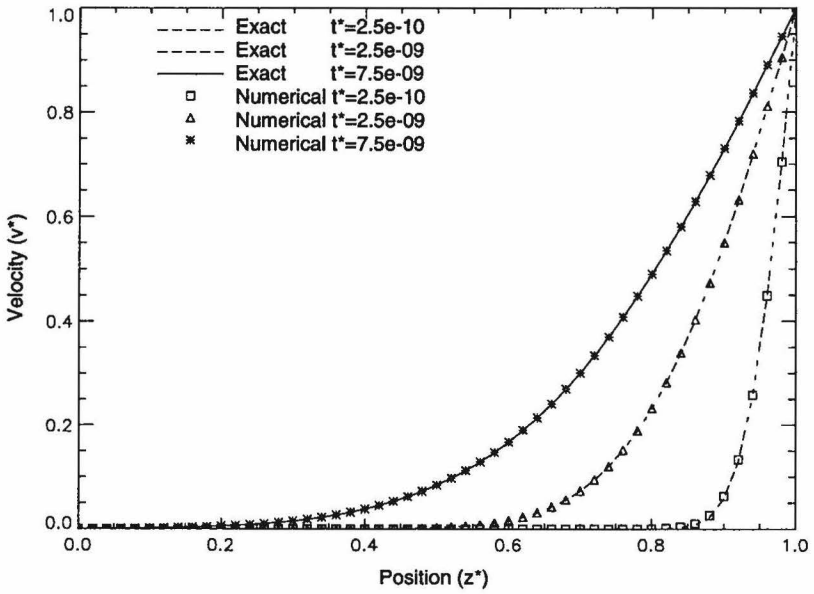

Figure 3.3: Comparison of the exact and numerically determined solutions for test case 1, $\Delta z^* = 0.02$.

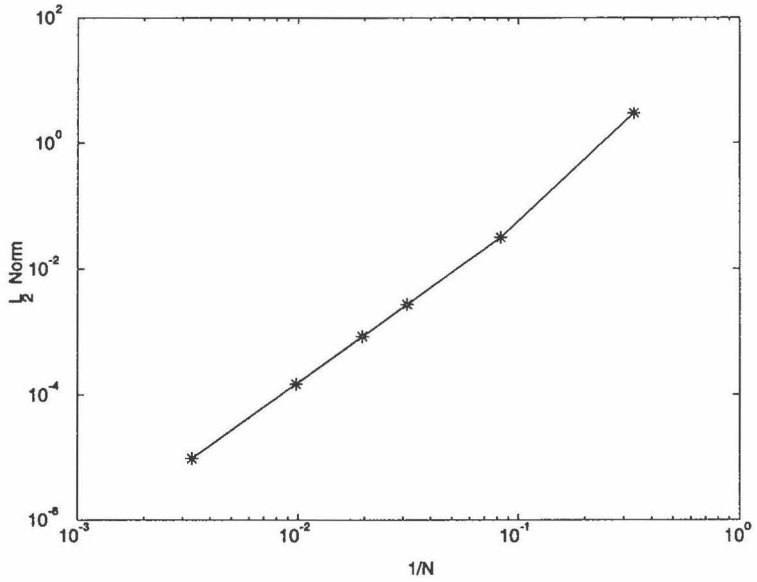

Figure 3.4: Rate of convergence for test case 1, $t^* = 2.5 \times 10^{-10}$.

convergence is determined from Figure 3.4. The slope of this plot is determined by a least squares fit to be 2.51. As was discussed in Section 3.4, a second order accurate spatial discretization procedure was used to solve the governing equations. It would thus be expected that the order of accuracy of the method would be slightly less than two, as a result of machine round off error. The reason for the slope in Figure 3.4 being slightly larger than two could be attributed to the accuracy of the time iteration in LSODE, and the fact that the exact solution is determined over a semi-infinite domain, while the numerically determined solution is solved over a finite domain.

3.5.2 Test Case 2: Linear Momentum Coupled with Displacement

A more general exact solution can be found to the system by coupling the linear momentum equation with the displacement relation. This is achieved by inserting

Equation (3.51) into Equation (3.49):

$$\frac{\partial^2 u^*}{\partial t^{*2}} = \hat{\alpha}\frac{\partial}{\partial z^*}\left[\left(\frac{\partial u^*}{\partial z^*}\right)^{\eta}\left(\frac{\partial^2 u^*}{\partial z^* \partial t^*}\right)^{\mu}\right]. \tag{3.56}$$

One assumes a solution to Equation (3.56) of the form:

$$u^* = e^{st^*} f\left(z^*\right), \tag{3.57}$$

where s is a constant. Substitution into Equation (3.56) yields:

$$s^2 e^{st^*} f = \hat{\alpha}\frac{\partial}{\partial z^*}\left[\left(e^{st^*} f'\right)^{\eta}\left(s\, e^{st^*} f'\right)^{\mu}\right] \tag{3.58}$$

$$= \alpha\, e^{st^*(\eta+\mu)} s^{\mu}\left[\eta f'^{(\eta-1)} f'' f'^{\mu} + \mu f'^{\eta} f'^{(\mu-1)} f''\right] \tag{3.59}$$

$$= \alpha e^{st^*(\eta+\mu)} s^{\mu} f'^{(\eta+\mu-1)} f''\left(\eta+\mu\right) . \tag{3.60}$$

Now, if one chooses $\eta + \mu = 1$ and rearranges the equation, one gets:

$$f'' - \frac{s^{2-\mu}}{\hat{\alpha}} f = 0. \tag{3.61}$$

The solution to this equation is:

$$f\left(z\right) = C_1 \cosh\left(k_n z\right) + C_2 \sinh\left(k_n z\right), \tag{3.62}$$

where C_1 and C_2 are constants, and s is expressed in terms of the wave number, k_n, as follows:

$$s = \left(\alpha k_n^2\right)^{\frac{1}{2-\mu}} . \tag{3.63}$$

The solution to Equation (3.56), under the above specified conditions, is therefore:

$$u^* = \exp\left[\left(\hat{\alpha} k_n^2\right)^{\frac{1}{2-\mu}} t^*\right]\left[C_1 \cosh\left(k_n z^*\right) + C_2 \sinh\left(k_n z^*\right)\right]. \tag{3.64}$$

One now sets $C_1 = 0$ in order to satisfy the condition $u^*(0,t^*) = 0$. The initial condition and condition at $u^*(1,t^*)$ are chosen to match the exact solution. The solution, boundary, and initial conditions, are summarized below:

$$u^*(z^*,t^*) = C_2 \exp\left[\left(\hat{\alpha}k_n^2\right)^{\frac{1}{2-\mu}} t^*\right] \sinh(k_n z^*) \ ,$$

$$u^*(0,t^*) = 0 \ , \qquad u^*(1,t^*) = C_2 \ \exp\left[\left(\hat{\alpha}k_n^2\right)^{\frac{1}{2-\mu}} t^*\right] \sinh(k_n) \ , \tag{3.65}$$

$$u^*(z^*,0) = C_2 \sinh(k_n z^*) \ .$$

The computer code is then used to solve the displacement field for this problem at $t^* = 0$, 1.25×10^{-2}, and 2.5×10^{-2}, with $\Delta z^* = 0.05$. Figure 3.5 shows the displacement versus position as time progresses with the following parameter values: $k_n = 1000$ and $C_2 = 1 \times 10^{-3}$. The rate of convergence at $t^* = 2.5 \times 10^{-3}$ is plotted in Figure 3.6. The slope is determined to be 2.30.

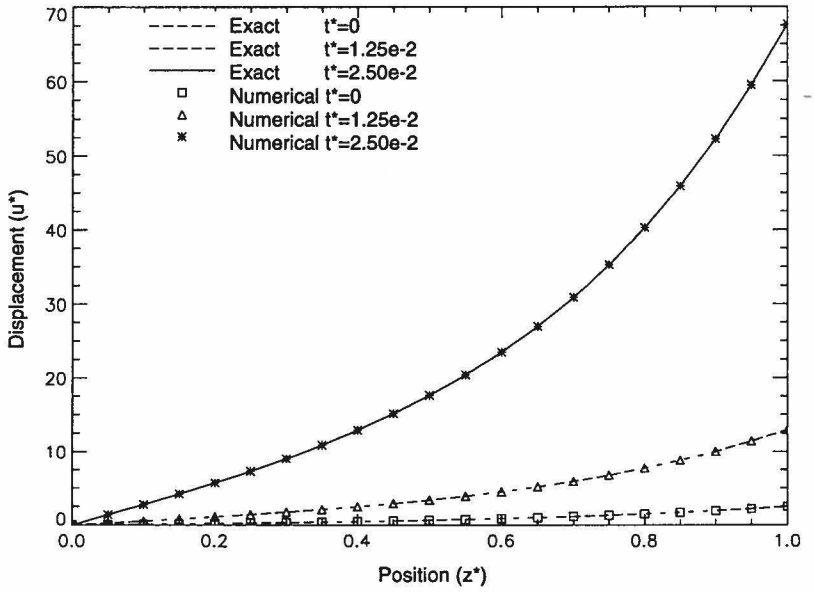

Figure 3.5: Comparison of the exact and numerically determined solutions for test case 2, $\Delta z^* = 0.05$.

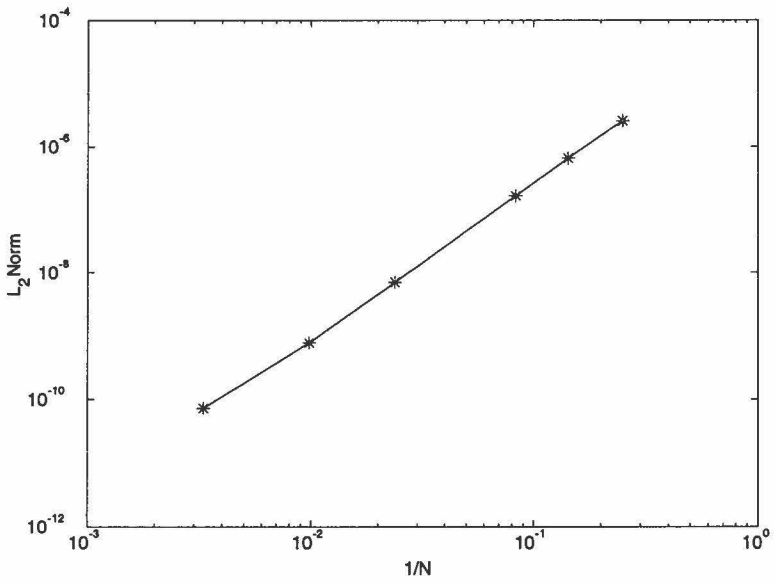

Figure 3.6: Rate of convergence for test case 2, $t^* = 2.5 \times 10^{-3}$.

3.5.3 Test Case 3: Energy Equation

It is also desired to determine an exact solution to a simplified form of the energy equation. If the initial and boundary conditions on v^* are such that they are always equal to zero:

$$v^*(0, z^*) = v^*(t^*, 0) = v^*(t^*, 1) = 0, \tag{3.66}$$

then $\frac{\partial v^*}{\partial z^*}$ will equal zero initially, resulting in a zero stress. With a zero boundary condition on v^*, the stress will remain zero and the velocity profile will never change. The energy equation is therefore decoupled, resulting in the following:

$$\frac{\partial T^*}{\partial t^*} = \frac{1}{Pe}\frac{\partial^2 T^*}{\partial z^{*2}}. \tag{3.67}$$

It can be easily verified by substitution that the following is a solution to this equation.

$$T^* = 1 - \omega \sin(n\pi z^*) \exp\left(\frac{-n^2\pi^2}{Pe} t^*\right) , \tag{3.68}$$

where ω is a constant and n is any integer. The boundary conditions are $T^*(t^*, 0) = T^*(t^*, 1) = 1$, and the initial condition is:

$$T^* = 1 - \omega \sin(n\pi z^*) . \tag{3.69}$$

Figure 3.7 shows the exact and numerically determined solutions for $t^* = 0,\ 2.5,$ and 12.5 with $n = 5$, $\omega = \frac{1}{2}$ and $\Delta z^* = 0.02$. The rate of convergence is determined at $t^* = 2.5$, and is seen in Figure 3.8. The slope is determined to be 2.48.

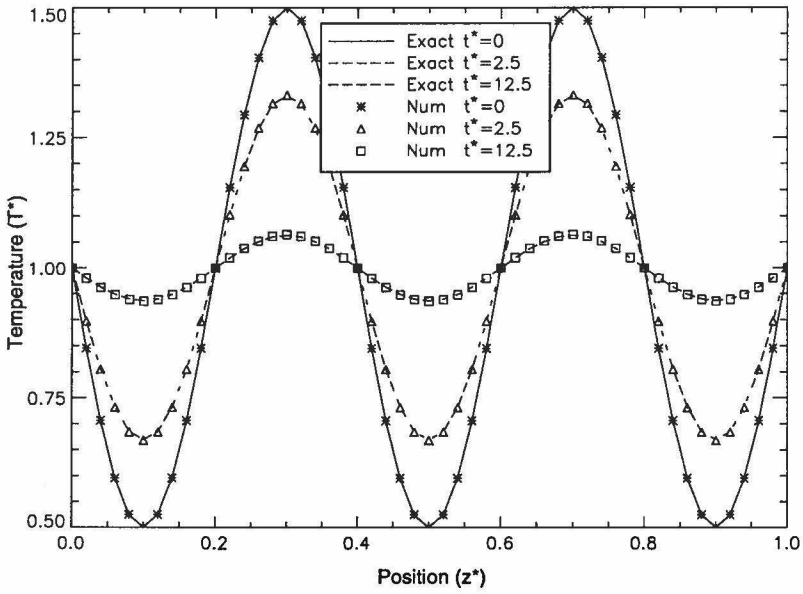

Figure 3.7: Comparison of the exact and numerically determined solutions for test case 3, $\Delta z^* = 0.02$.

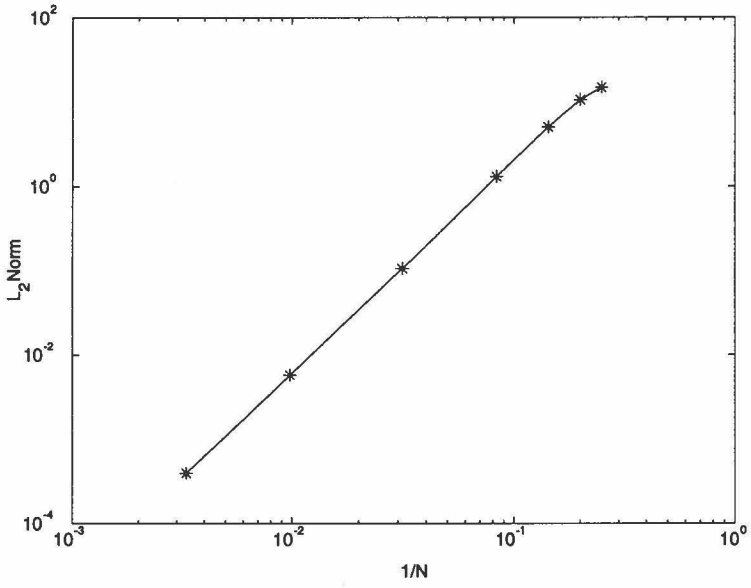

Figure 3.8: Rate of convergence for test case 3, $t^* = 2.5$.

CHAPTER 4

RESULTS

This chapter will present results determined from the TSHB as well as those from the theoretical model. Experimental results for tests on S-7 tool steel (TS) will first be presented, with comparisons drawn between the numerical and experimental results, as well as with results determined from other researchers. Results will then be presented for tests on the following explosive simulants: a PBX cure cast simulant, a PBX pressed simulant, and a melt cast simulant known as Filler-E. These simulants are used to approximate the material properties of PBXN 109, PBX 9501, and tritonal, respectively. The results of these tests will be used to determine approximate parameters for the constitutive law for stress used in this thesis. Finally, numerical simulations will be run on 1018 CRS, and S-7 tool steel to compare with previously determined results, and simulations will be run on the aforementioned explosives.

4.1 Experimental Results on Explosive Simulants

In this section, results determined from the TSHB on tests of the explosive simulants are presented. The strain and strain rate hardening parameters from the constitutive law for stress are then determined from the data. It is important to note that, to our knowledge, no researchers have tested any of these materials in torsion. The results presented in this section are thus previously unrecorded.

4.1.1 Tests on the PBX Cure Cast Simulant

The results of tests performed at various shear strain rates on the PBX cure cast simulant are included in Figure 4.1. The reported results are characteristic of a few tests performed at each strain rate. In this figure, test 40 was performed at a shear strain rate of 415 s^{-1} and lasted for 700 μs, the full length of the loading

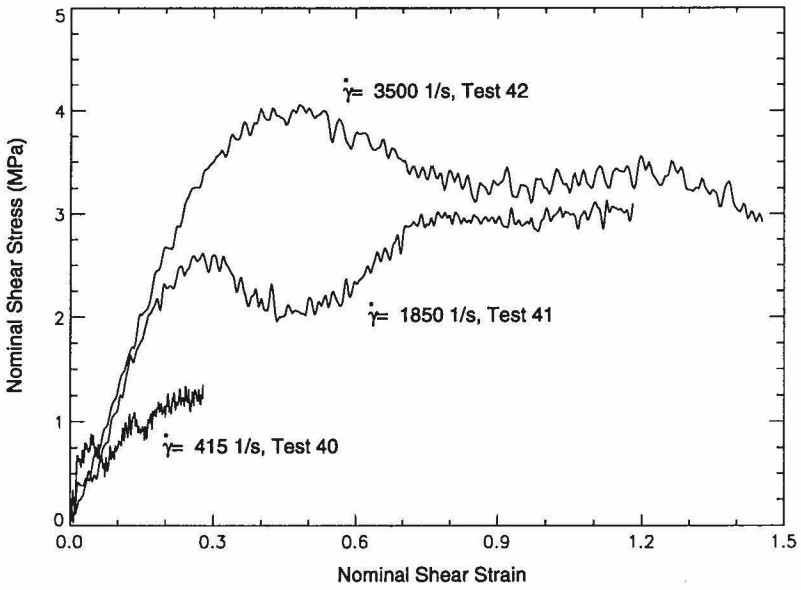

Figure 4.1: Results from TSHB tests on the PBX cure cast simulant.

pulse. The cause for the initial overshoot in shear stress at a shear strain of 0.05 is unknown, but it could be a material characteristic, or due to the loading geometry. Zener and Hollomon (1944) have stated that a maximum in the stress-strain graph is indicative of the formation of an instability in the deformation. The specimen in this test never failed, and since the shear stress-shear strain curve never reached a maximum, it is assumed that no instability was reached. This test thus provides an accurate measurement of the strain hardening in this material. Prior to performing this test, a line was drawn axially across the specimen. Post test examination of

this line revealed no permanent deformation in the specimen. It is thus concluded that this material behaves in a nonlinearly elastic manner over the shear strain rates tested.

Test 41, which was performed at a shear strain rate of 1850 s^{-1}, also lasted for 700 μs. The initial peak in the shear stress at a shear strain of 0.28 is a result of the overshoot, as seen in Test 40. Upon post-test examination of the specimen, a small tear was noticed in the circumferential direction within the gage length. This is the consequence of an instability, which could thus account for the decrease in the slope of the shear stress-shear strain curve after a shear strain of 0.75. This test would thus provide an inaccurate measurement of the material's strain hardening characteristic. In addition, it was noticed that even with the onset of instability, the deformation was recovered, indicating purely elastic deformation.

Test 42, which was tested at a shear strain rate of 3500 s^{-1}, lasted for about 400 μs. The peak in the shear stress at a shear strain of 0.5 is believed to be a result of the stress overshoot. The specimen in this test failed, with an instability thought to occur around a shear stress of 0.8. This instability prevented the material from further hardening, hence making the overshoot appear to be the occurrence of the instability, instead of where it is actually thought to occur. Examination of the failure surface revealed voids visible to the naked eye. In addition it was observed that failure did not occur along a single plane, but along an irregular surface, as if the material were torn apart. It is thus doubtful that this material demonstrates shear localization under the given loading conditions.

The data determined herein was then used to calibrate the constitutive law, Equation (3.6). It is important to note, however, that it is necessary to perform more tests on this material in order to more accurately calibrate the constitutive law. This constitutive law introduces the strain hardening parameter, η, and the strain rate hardening parameter, μ. Since it is believed that test 40 results in the most accurate characterization of the strain hardening, η was chosen by trial and error, such that the slope determined from the constitutive model approximately matched the slope of the shear stress-shear strain curve determined from this test. Due to the onset of instability, the results from tests 41 and 42 are unreliable once a maximum shear stress is attained. The results up to the maximum shear stress are accurate, however, and were used to determine the strain rate hardening parameter, μ, by trial and error. These values are tabulated in a later section.

4.1.2 Tests on the PBX Pressed Simulant

Figure 4.2 shows the results from tests performed by the TSHB on the PBX pressed simulant, where the reported results are characteristic of a few tests performed at each strain rate. Referring to this figure, test 29, which was performed at a shear strain rate of 300 s^{-1}, lasted for about 350 μs. This material in this test also exhibited a stress overshoot, occurring at a shear strain of 0.15. Observation of the post test specimen revealed a planar failure with a rough failure surface including small voids. This is as would be expected in microvoid nucleation induced shear localization. The instability which caused failure is assumed to account for the peak in the shear stress-shear strain curve at a shear strain of 0.065. Test 38, which was performed at a shear

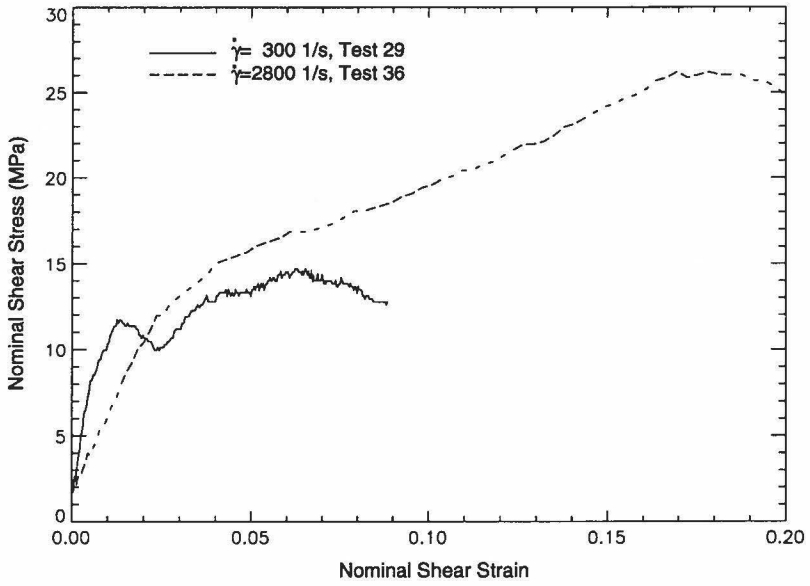

Figure 4.2: Results from TSHB tests on the PBX pressed simulant.

strain rate of 2800 s^{-1} lasted only 75 μs, due to the high strain rate deformation. No overshoot was observed in this test. Examination of the post-test specimen revealed fragmentation of the gage length as well as the flanges. Due to this catastrophic failure, these results may not be truly indicative of the material. By a fractographic study of the fragments, it was determined that cracks initiated in the gage length and propagated outward into the flanges at an angle to the axis of the cylinder, which is indicative of brittle failure.

In order to more accurately determine the order of events in the failure of this specimen, high speed photographs were taken of the deformation experienced by one of these simulants. In the test during which photographs were taken, the shear strain rate was 2850 s^{-1}. A plot of the transmitted shear strain for this test, which is proportional to the shear stress in the specimen, is included in Figure 4.3. High speed photographs of the specimen deformation in this test are included in Figure 4.4. In

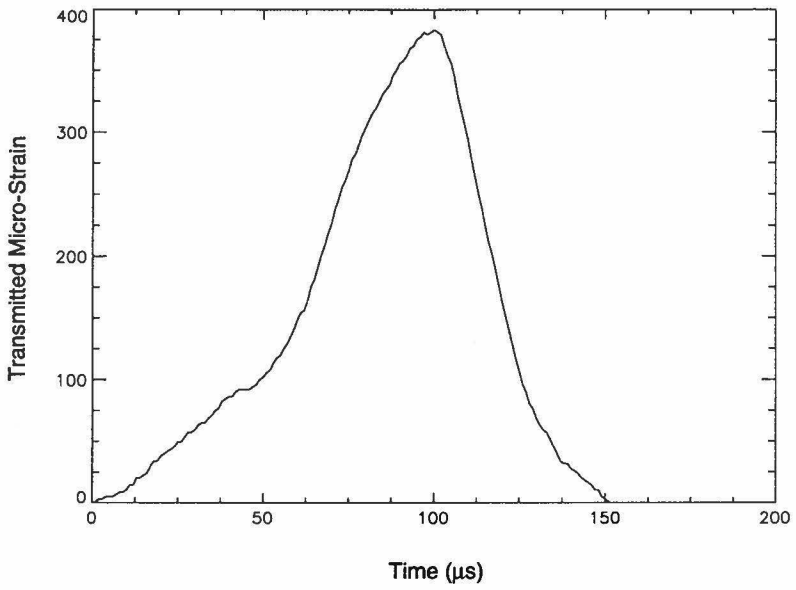

Figure 4.3: A plot of the transmitted shear strain for Test 49 on the PBX pressed simulant, $\dot{\gamma} = 2850\ s^{-1}$.

these photographs, the vertical black line to the right of the gage length is a result of the camera removing a strip of light from each frame for other purposes. In Figure 4.4, the photograph labeled $t = 0\ \mu s$ was taken when the incident pulse first reached the specimen. The photograph labeled $t = 167\ \mu s$ was taken some time after the transmitted strain, as depicted in Figure 4.3, reached a maximum. In the center of the gage length of the specimen in this picture, a small crack is visible. From the complete photographic record, not included in this thesis, this crack formed at approximately $t = 113\ \mu s$, which is just after the transmitted shear strain reaches a maximum, as seen in Figure 4.3, which indicates that the drop in the transmitted strain is the result of this failure mechanism. From the photograph labeled $t = 227\ \mu s$, it is seen that the crack has increased in size, and that other faint cracks have formed below it. Finally, the photograph labeled $t = 520\ \mu s$, which was taken of a separate test performed at a comparable shear strain rate, reveals the ultimate fragmentation

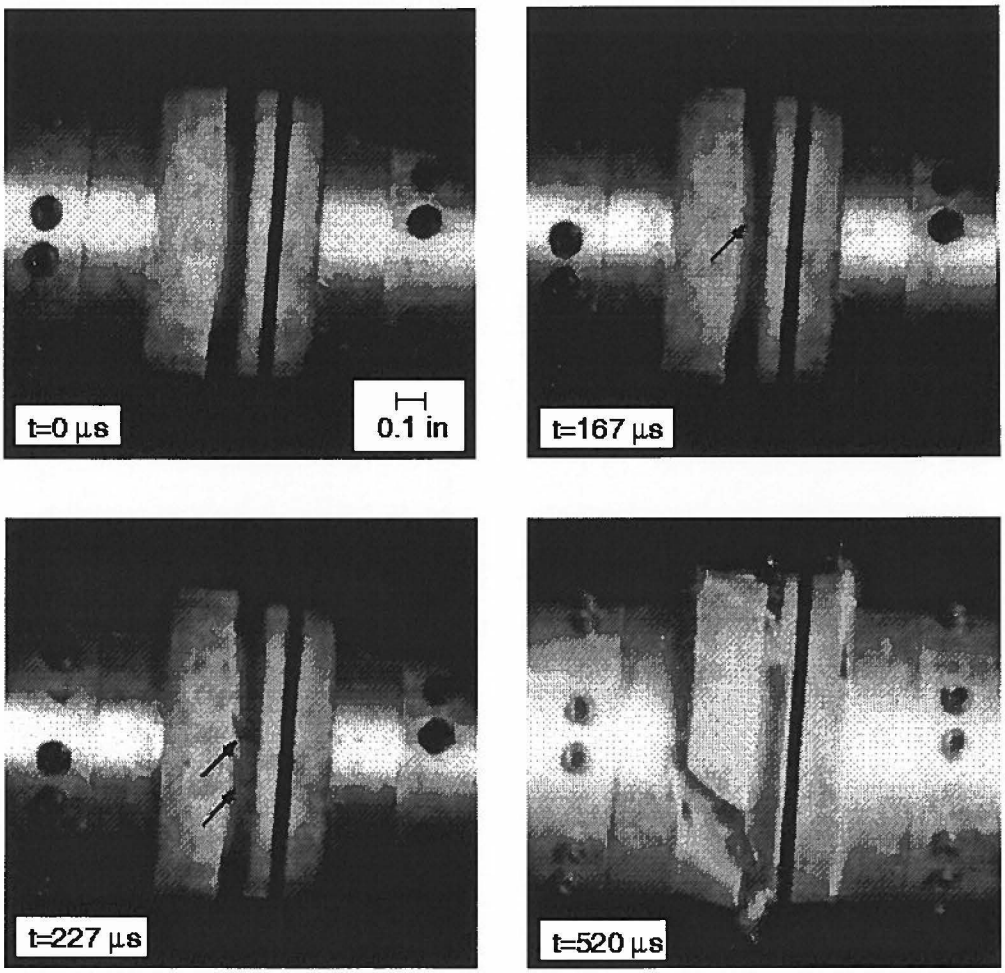

Figure 4.4: High speed photographs of the failure of a PBX pressed simulant, Test 49.

of the specimen. It is thus confirmed that cracks initiate in the gage length and propagate outward through the flanges. In comparison with the failure of the lower strain rate test, Test 29, it is concluded that the type of failure for this material is dependent on the loading rate.

In order to develop a constitutive model for this material, the parameters from Equation (3.6) are again approximated to match the constitutive law to this data. The value of η was determined from test 29, since the material in this test exhibited a greater amount of strain hardening prior to the onset of instability. The strain rate

hardening parameter, μ, was determined such that the constitutive model matched the peak stress obtained in test 38.

4.1.3 Tests on Filler-E

Figure 4.5 shows the results from tests on Filler-E, where the reported results are characteristics of a few tests performed at each strain rate. In this figure, Test 30,

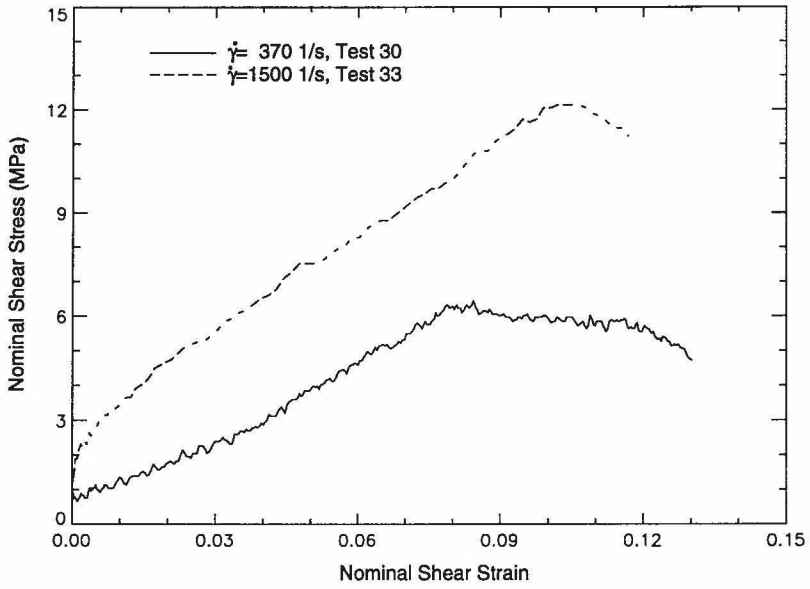

Figure 4.5: Results from TSHB tests on Filler-E.

which was performed at a shear strain rate of 370 s^{-1}, lasted 375 μs. Fragmentation of the Filler-E specimen occurred in much the same way as did in the high strain rate test on the PBX pressed simulant. Cracks appear to have begun in the gage length and propagated through the specimen at 45° to the axis of the specimen. On tests when there was minimal fragmentation, it was possible to observe the failure surface, which was irregular, not at all indicative of shear localization. On test 33, which was performed at a shear strain rate of 1500 s^{-1}, deformation lasted 120 μs.

From Figure 4.5, it is seen that this material has a high sensitivity to strain rate. Tests at this strain rate caused significant fragmentation, with failure similar to that for the low strain rate test. Although Filler-E demonstrates strain and strain rate hardening, the constitutive law could not be fit to a significant portion of the shear stress-shear strain curves seen in Figure 4.5. This is due to the fact that Filler-E does not demonstrate strain hardening that can be represented in the form of a power law.

4.2 Comparison of Experimental Results with Numerical Predictions

This section presents the results from experimental tests on 1018 CRS and S-7 tool steel, with comparisons to results from numerical simulations of these tests. The constitutive and material parameters used in these numerical simulations, as well as in those in a later section, are included in Table 4.1. The parameters for 1018 CRS were taken from Hartley *et al.* (1987), who determined the constitutive parameters

Material	Constitutive Parameters				Material Parameters		
	α $\left(MPa\frac{s^m}{K^\nu}\right)$	ν	η	μ	ρ $\left(\frac{kg}{m^3}\right)$	c_A $\left(\frac{J}{kg \cdot K}\right)$	k $\left(\frac{W}{m \cdot K}\right)$
1018 CRS[1]	3,458	-0.38	0.015	0.019	7800	500	54
S-7 TS[2]	6,700	-0.31	0.030	0.012	7750	477	40
PBX 9501	33,000	-1.28	0.320	0.080	1840	1130	0.454
PBXN-109	800	-1.38	0.400	0.320	1670	1260	0.104
Tritonal	-	-9.68	-	-	1690	960	0.460

Table 4.1: Constitutive and material parameters used in the numerical calculations. (1) Johnson and Cook (1983). (2) Hartley *et al.* (1987).

from a least squares fit of the experimental results of Costin *et al.* (1979). The constitutive parameters for S-7 tool steel were determined from an approximate fit of the constitutive law for stress used in this thesis to the Johnson-Cook law (1983), over the following calibration conditions: shear strain ranging from $0 - 100\%$, shear strain rate ranging from $1 \times 10^{-3} - 5 \times 10^{2}\ s^{-1}$, and temperature ranging from $298 - 537\ K$. The material parameters for S-7 tool steel were taken from Johnson and Cook. The material parameters for PBX 9501 were taken from Dobratz and Crawford (1985), and the material parameters for PBXN-109 and tritonal were taken from Hall and Holden (1988). The thermal conductivity for PBXN-109 was not found, so the value for PBXW-114, a material of similar composition, was used. In order to determine the thermal softening function for some of the materials they tested, Johnson and Cook assumed a linear decrease in the stress as a function of temperature, with the stress reaching zero at the melting point. Since PBX 9501 and PBXN-109 react before melting, their thermal softening parameters are estimated such that the stress is decreased by 50% at the reaction initiation temperature. From Dobratz and Crawford, PBX 9501 reacts at $240°C$, and from Hall and Holden, PBXN-109 reacts at $220°C$. The thermal softening parameter for tritonal was estimated such that the stress is decreased by 90% at the melting temperature of $80°C$. The remaining constitutive parameters were determined from the experimental results on the explosive simulants, as described in the previous section.

4.2.1 Tests on S-7 Tool Steel

In order to determine the effects which heat treating can have on material properties, tests using the TSHB were performed on S-7 tool steel at a shear strain rate of 1500 s^{-1}, with the material tested in the condition in which it was received and also at a hardness of Rockwell C-51. Figure 4.6 shows the results of these tests. From

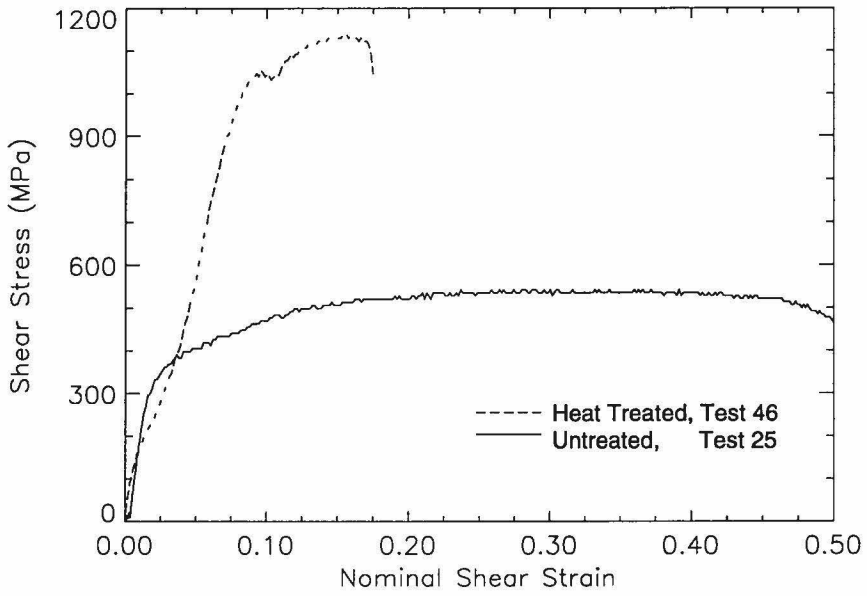

Figure 4.6: Comparison of heat treated and untreated material characteristics for S-7 tool steel, $\dot{\gamma} = 1500\ s^{-1}$.

this figure, it is seen how drastic an effect this heat treatment had on the material properties. The untreated material fails at a shear strain 2.9 times as large as the treated material, and the treated material reaches a maximum shear strain 2.1 times as large as the untreated material. It is thus determined that the heat treatment of a material can have a significant effect on the material characteristics.

Next, in order to compare the experimental and numerical results, a simulation was performed on S-7 tool steel at a shear strain rate of 1500 s^{-1}. The parameters for this simulation were determined from an approximate fit to the shear stress-shear

strain curve determined from the Johnson-Cook law for S-7 tool steel. The Johnson-Cook law parameters for S-7 tool steel were determined from a fit to the experimental data determined by Johnson *et al.* (1983), who reported the material to have a hardness of Rockwell C-50. The physical constants for the numerical simulation, included in Table 4.2 under simulation #1, were chosen to match the experimental conditions. Figure 4.7 shows the experimentally determined shear stress-shear strain curves for S-7 tool steel as well as the results from the numerical simulation. Although it is not

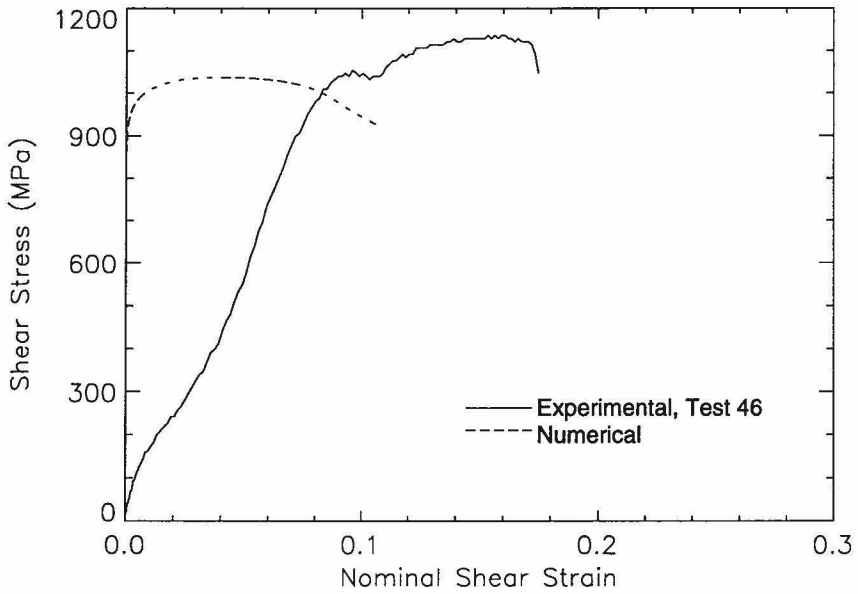

Figure 4.7: Comparison of experimentally and numerically determined material characteristics for S-7 tool steel, $\dot{\gamma} = 1500\ s^{-1}$.

evident from this figure, the numerical results provide detailed information about the low shear strain behavior, with the shear stress dropping to zero at a shear strain of zero. From observation of this figure, it is first noticed that there is a difference in the initial slope of the shear stress-shear strain curves. This was also observed in the earlier testing of 1018 CRS, which was reported in Section 2.5. The reasons for this difference have already been discussed.

The maximum shear stress reached by the simulation is, however, a good approximation of the experimentally determined stress, with the value from the simulation 8% less than the experimental result. The shear strain at failure, is not as good a match with the value from the simulation 40% less. However, if the amount of straining in the purely plastic range is compared, results are fairly accurate. This is accomplished by comparing the difference in shear strain from the value when the stress increases to 90% of its maximum value to the value when the stress falls to 90% of its maximum value. It is determined that the experimental results predict only 10% less straining than the numerical results. It is important to note that the experiments performed by Johnson *et al.* were only performed up to shear strain rates of $10^2\ s^{-1}$, thus the constitutive law was calibrated at a much lower shear strain rate. In addition, although the hardness of the material in their tests was reported, the exact heat treatment is unknown. Since the effect of heat treating on the material properties has been shown to be drastic, it is surprising that the numerical simulation, which was calibrated to different data, provided results that are this accurate.

4.2.2 Test on 1018 CRS

Tests were also run on 1018 CRS, at a shear strain rate of $1500\ s^{-1}$, with comparisons drawn to a numerical simulation of the test and to results by other researchers. The physical constants for the numerical simulation are included in Table 4.2 under simulation #2. Experimental and numerical results from these tests can be seen in Figure 4.8. The numerical simulation predicted a maximum shear stress 23% less than that achieved in Test 22, and the ultimate shear strain about 9% greater than

Simulation Number	v_1 (m/s)	L_s (mm)	t_1 (μs)	w_0 (mm)	h_p	v_0 (m/s)
1	3.75	2.50	33.33	0.38	0.10	3.75×10^{-2}
2	3.75	2.50	33.33	0.38	0.10	3.75×10^{-2}
3	12.50	2.50	20.00	0.38	0.10	1.25×10^{-1}
4	4.77	3.18	6.67	0.81	0.05	4.77×10^{-2}
5	7.00	2.50	32.14	2.50	0.10	7.00×10^{-2}
6	6.25	2.50	32.00	2.50	0.10	6.25×10^{-2}

Table 4.2: Physical constants used in the numerical simulations reported within this thesis.

the experiment. In comparison of the numerical results with the experimental results of Duffy and Chi (1992), it is noticed that the numerical results in the current study are much more accurate in predicting Duffy and Chi's experimental results, with a maximum shear stress only 8% less than Duffy and Chi's. It is important to note that the parameters used in the numerical simulation were determined by Hartley *et al.* (1987), who may have used a material with a different heat treatment. Since the actual heat treatment of Duffy and Chi's 1018 CRS is unknown, and since the heat treatment has been shown to significantly affect material properties, it is believed that the differences in the results can be attributed to different heat treatments.

4.3 Numerical Simulations on Nonreactive Materials

This section presents the results from numerical simulations on S-7 tool steel, and PBXN-109 and PBX 9501 with the effects of reaction excluded. The results for

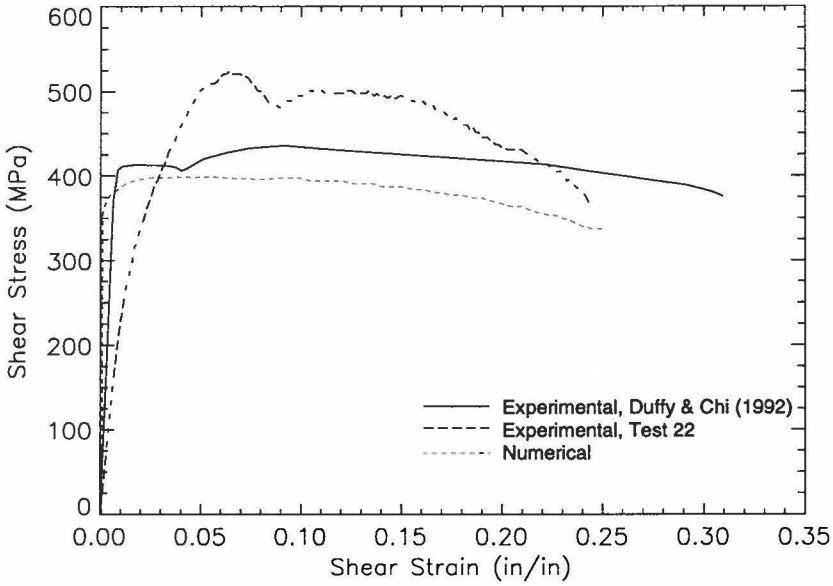

Figure 4.8: Comparison of experimental and numerical characteristics for 1018 CRS at a shear strain rate of 1500 s^{-1}.

the simulations on S-7 tool steel are presented in comparison with numerical results of other researchers.

4.3.1 Comparison of Results for S-7 Tool Steel

Batra *et al.* (1995) used the Johnson-Cook constitutive law, with parameters reported by Rajendran (1992), to model the torque required to deform a thin walled tube of S-7 tool steel, among other materials. As mentioned previously, Equation (3.6) was calibrated so as to match the Johnson-Cook law. In order to match the physical conditions used in their test, the constants reported in Table 4.2 under simulation #3 were used. This test corresponds to deforming a tube with an inner diameter of 9.5 mm at a shear strain rate of 5000 s^{-1}. From Figure 4.9, which gives the results of this simulation along with the results from Batra *et al.*, it is seen that the results are very similar. The magnitude of the torque predicted in the current study is within

4% of that predicted by Batra *et al.*, and the failure strain is predicted to within 0.5%. The similarities between these results are impressive, considering the fact that different constitutive models for stress were used. These results further justify those reported by Wright (1987) and Batra and Kim (1991), as discussed in Section 1.3.2, who concluded that the choice of constitutive models is not significant.

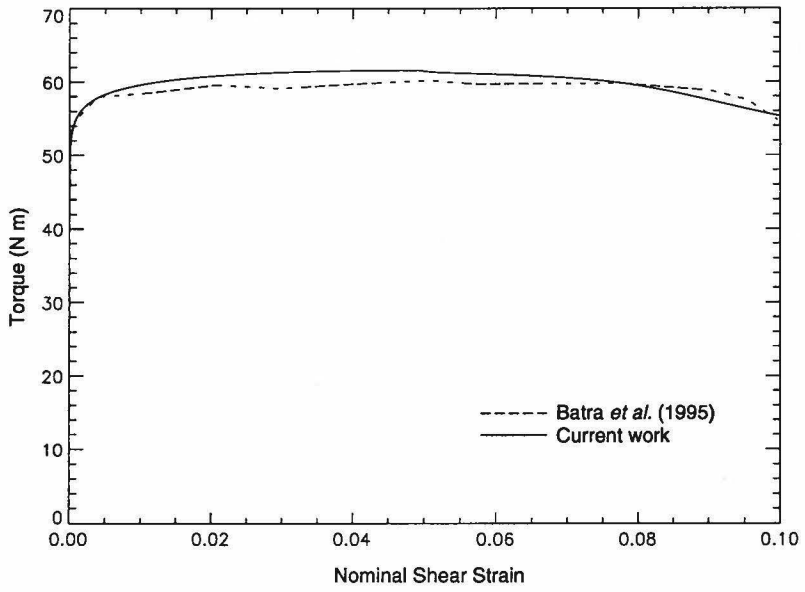

Figure 4.9: Comparison of the results determined by numerically testing S-7 tool steel at a shear strain rate of 5000 s^{-1} with those by Batra *et al.* (1995).

4.3.2 Further Comparison of Results for S-7 Tool Steel

Batra and Kim (1992) performed a similar study to Batra *et al.* (1995), in which they modeled the velocity, temperature and shear stress across the length of the specimen. In this thesis, simulations were again performed on S-7 tool steel, with the physical parameters chosen to match the test conditions of Batra and Kim (see simulation #4 in Table 4.2). Figure 4.10 shows the evolution of the velocity profile for S-7 tool steel with an imposed shear strain rate of 1500 s^{-1}. This figure can then

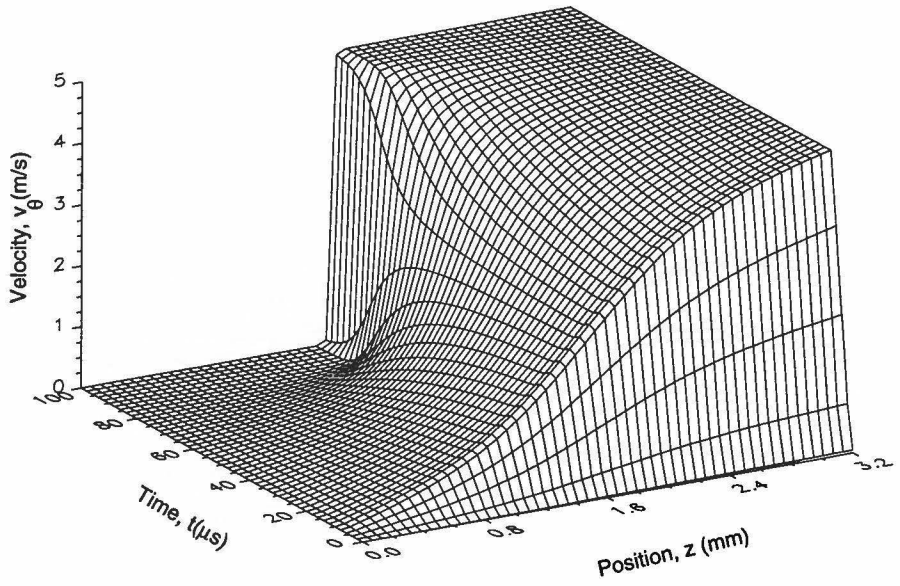

Figure 4.10: Evolution of the velocity field for S-7 tool steel being deformed at a shear strain rate of 1500 s^{-1}.

be compared with the results determined by Batra and Kim, reported in Figure 1.10, where a shear strain of 0.16 is reached following localization. The results in this thesis achieved a shear strain of 0.145 following localization, a difference of approximately 10%. Batra and Kim also report that the ratio of the average strain when a shear band initiates to the average strain at which the shear stress attains its peak value is 1.7 for S-7 tool steel. If it is assumed that a shear band forms when the stress drops to 95% of the maximum stress (as stated by Batra and Kim), the value of the ratio as determined in this thesis is 2.0, a difference of about 17% from Batra and Kim's value. It is important to note that this value is consistent with S-7 tool steel, since other materials tested by Batra and Kim achieve ratios up to 3.03. Batra and Kim also found that the temperature at the center of the shear band just after it formed was approximately twice as large as the ambient temperature. This thesis confirms that result, as is seen in Figure 4.11, which is very similar to Figure 4b in Batra and

Kim (1992). The differences in these results could be attributed to the difference in the constitutive law for stress, or perhaps to the difference in grid size. Batra and Kim used a variable grid size with the greatest number of elements at the center. As can be seen in Figure 4.11, the current grid size is not fully effective in resolving the behavior in the shear band. Since the temperatures, shear strains and shear strain rates achieved in the shear bands are far in excess of the calibration conditions, it isn't expected that any constitutive law will be extremely accurate at predicting behavior following localization. Hence, the similarities between these studies are impressive.

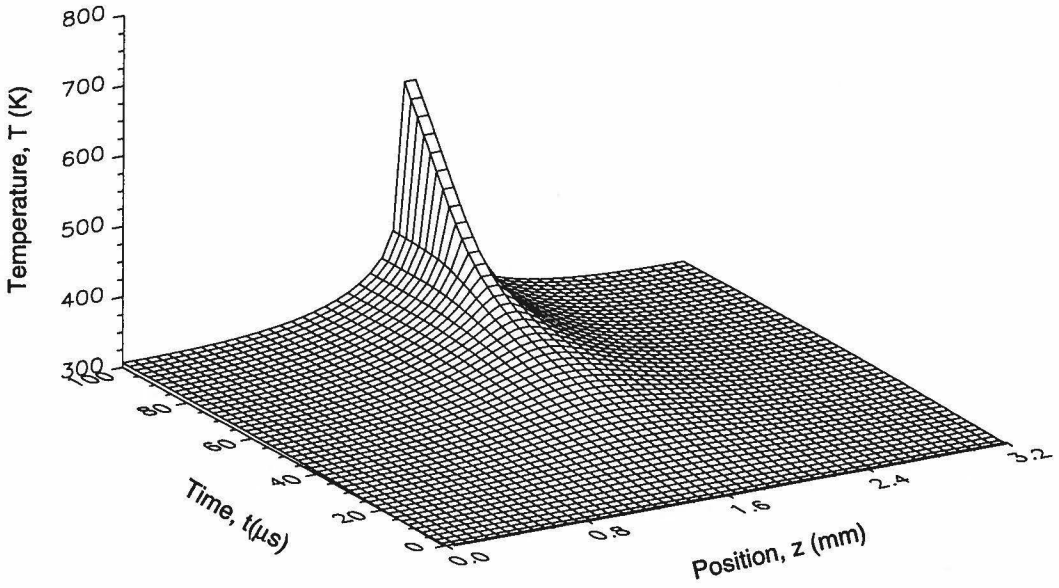

Figure 4.11: Evolution of the temperature field for S-7 tool steel being deformed at a shear strain rate of 1500 s^{-1}.

4.3.3 PBX 9501 Without Reaction

Next, numerical simulations were performed for the deformation of PBX 9501, with the effects of reaction excluded. This was studied in order to compare with the experimental results on the PBX pressed simulant and to determine the material's

susceptibility to localization. Reaction was excluded by setting Z equal to zero in the computer code. The physical constants, included in Table 4.2 under simulation #5, were chosen to match the experimental conditions. For this case, the test was performed at a shear strain rate of 2800 s^{-1}. In order to determine the onset of localization, the localization criterion, Equation (3.33), is evaluated at the center of the specimen. The right hand side, Φ, and left hand side, Ψ, of this criterion are plotted as functions of time in Figure 4.12. In this criterion, Ψ is a combined measure of the strain and strain rate hardening effects, while the Φ is a measure of the thermal softening. It is seen that both Φ and Ψ are always positive, indicating

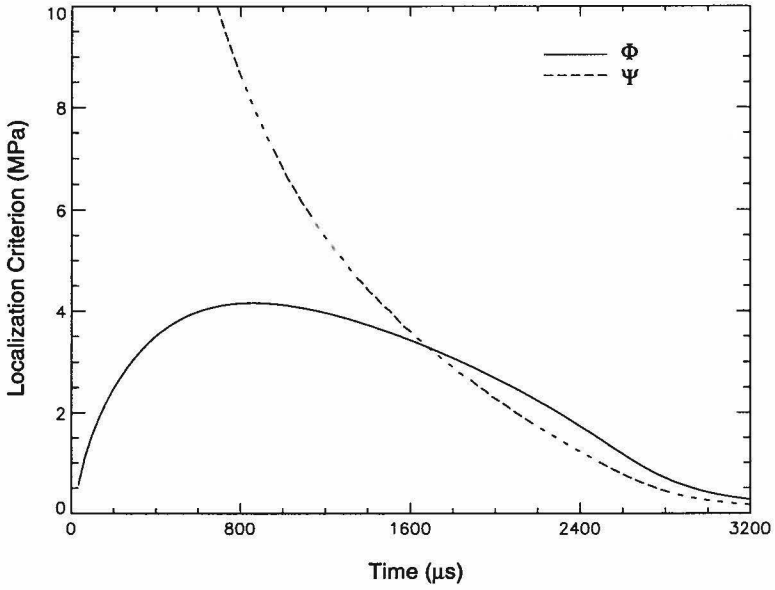

Figure 4.12: Localization criterion for PBX 9501 without reaction, where Φ represents thermal softening and Ψ represents strain and strain rate hardening.

that the material is experiencing strain and strain rate hardening as well as thermal softening, as expected. When Ψ is less than or equal to Φ, this criterion predicts that localization will begin. For this test, the onset of localization is reached after 1.67 *ms*.

The effects of localization are readily seen by studying the evolution of the velocity and temperature profile, as seen in Figures 4.13 and 4.14. Figure 4.13 shows the three stage localization process, which was initially observed experimentally by Marchand and Duffy (1988). After the velocity at $z = L$ reaches its final value, the profile essentially forms a linear distribution in space, which is called homogeneous deformation. Marchand and Duffy have termed this Stage I of the localization pro-

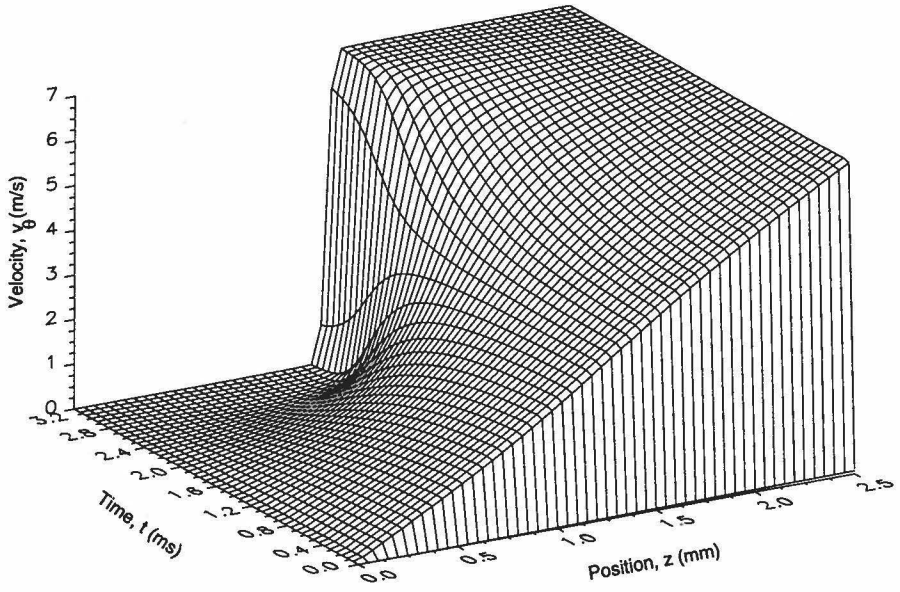

Figure 4.13: Evolution of the velocity field for PBX 9501 without reaction.

cess. Since the specimen is thinnest at its center, it is also weakest at that point. The material is thus locally less resistant to deformation, hence developing an inhomogeneous velocity profile with the greatest slope at the center. This is referred to as Stage II. The Stage II localization is very subtle in this test and is not readily observed. Now, the shear strain rate is equal to the slope of the velocity profile, so, as it increases, it causes the stress to increase. The combined effect of the increased shear stress and shear strain rate cause the temperature to increase, as is seen in Fig-

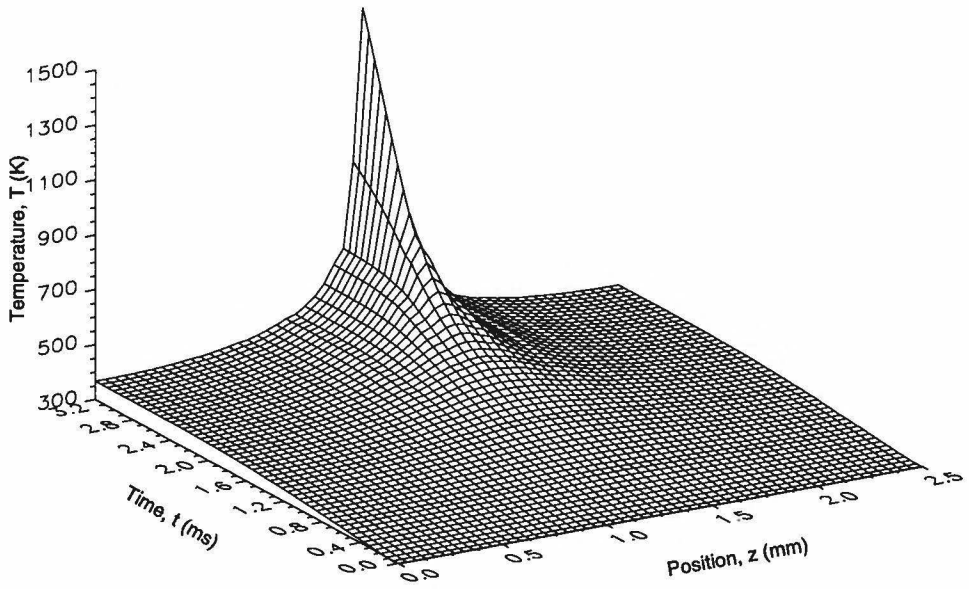

Figure 4.14: Evolution of the temperature field for PBX 9501 without reaction.

ure 4.14. The rise in temperature causes the stress to drop, which results in further straining and further heating. This interaction continues until, after 1.67 ms, the thermal softening dominates over the strain and strain rate hardening. Consequently, deformation rapidly localizes to a narrow region, referred to as Stage III localization.

It is this final stage of localization that is termed shear localization, or shear banding. At this time, the rate of change in the temperature increases dramatically at the center of the shear band, resulting in a pronounced spike in temperature. The temperature at the center of the shear band at the onset of localization is 458 K. After 3.2 ms, the temperature at this point has increased to 1590 K. It is interesting to note that the temperature of the material at the onset of localization has already almost reached its initiation temperature of 513 K, and that following localization the temperature far surpasses this value. Hence, it is expected that shear localization in PBX 9501 would produce initiation of reaction.

These numerical results are now compared to the experimental results determined from the PBX pressed simulant. Figure 4.15 compares the experimental and numerical shear stress and shear strain characteristics. From this figure, it is seen that the

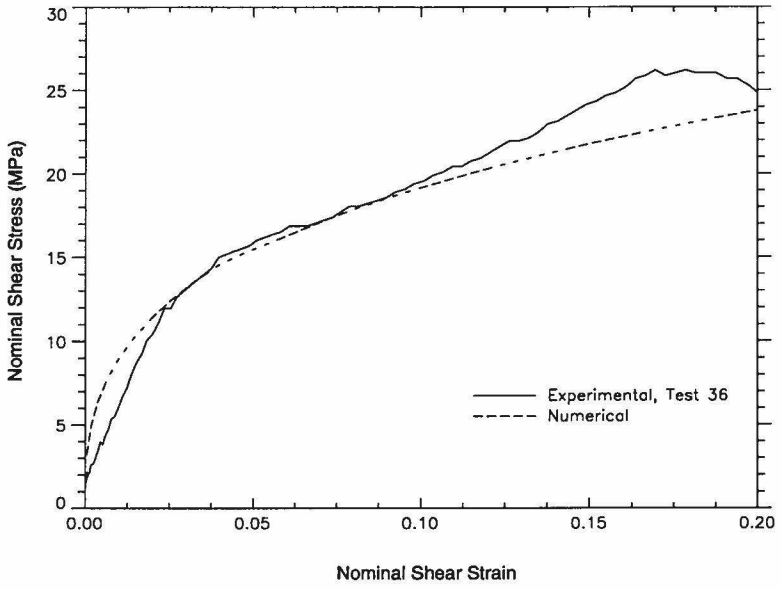

Figure 4.15: A comparison of the experimental and numerical results for the PBX pressed simulant.

computer code predicts the shear stress and shear strain characteristics fairly accurately until just before failure. The code, however, does not predict localization to begin until a nominal shear strain of 4.63 is reached, as compared with the experimental failure at 0.20 shear strain. The full numerically determined shear stress-shear strain curve is included in Figure 4.16. It is thus concluded that the PBX pressed simulant does not fail due to shear localization, but instead due to some other mechanism. This does agree with experimental observations, which suggested that failure could have occurred due to microvoid nucleation and growth, crack propagation or fragmentation. Since these failure mechanisms were not built into the numerical model, the code can not accurately predict this form of failure.

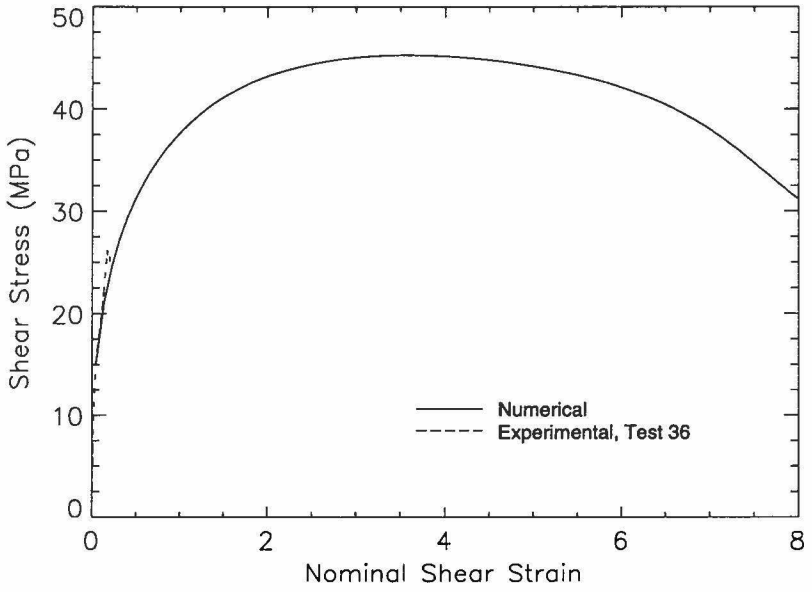

Figure 4.16: Experimental and numerical shear stress-shear strain curves up to failure for the PBX pressed simulant.

4.3.4 PBXN-109 Without Reaction

Numerical simulations were then performed on PBXN-109, with the effects of reaction excluded. The physical constants, included in Table 4.2 under simulation #6, were chosen to match the experimental conditions of test 42, with a shear strain rate of 2500 s^{-1}. Since it is believed that the PBX cure cast simulant demonstrates nonlinear elastic deformation, it is questionable whether it can be accurately modeled by the numerical method, which assumes viscoplastic heating. Despite this fact, simulations were performed on this material, with the assumption of visco-plastic heating, in order to learn more about the shear localization and thermal initiation processes. The localization criterion for this test is included in Figure 4.17, which predicts the onset of localization after 272 ms. It is noticed, however, that by the time Φ becomes greater than Ψ, the parameters have essentially ceased changing. The shear strain and shear strain rate hardening effects have thus reached a balance

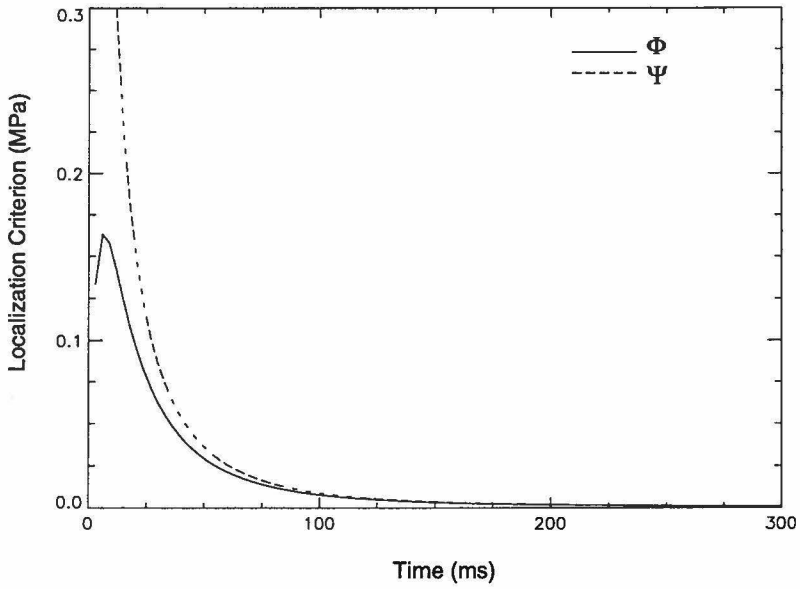

Figure 4.17: Localization criterion for PBXN-109 without reaction.

with the thermal softening effect. Figure 4.18 shows the evolution of the velocity profile for this test. From this figure, it is seen that Stage II is reached, but that transition into localization does not occur. In comparison with PBX 9501, it is seen that PBXN-109 develops a greater inhomogeneity in Stage II, but that PBX 9501 is more susceptible to eventual localization. Further iteration in time reveals that the velocity profile begins to return to a homogeneous state, rather than localizing. Figure 4.19 shows the evolution of the temperature profile, which shows temperature to increase in an inhomogeneous manner. It is interesting to notice that the temperature exceeds the reaction temperature of 493 K after about 10 ms. It is thus concluded that shear localization is not necessary for initiation to occur in this material; an inhomogeneous growth in temperature can eventually lead to significant increases in its value. However, the time over which this process occurs is significantly longer than the experimentally recorded time to failure of 350 μs. It is hence determined that the

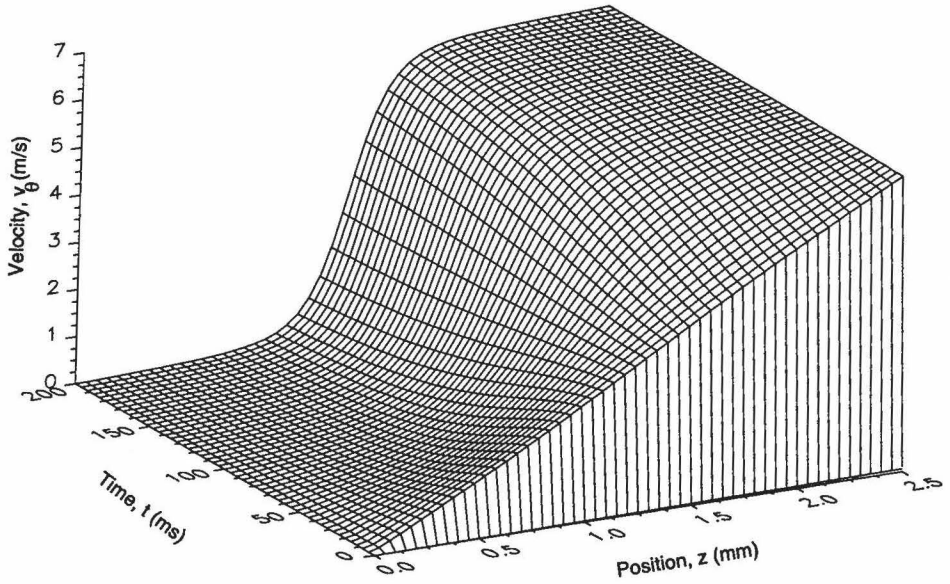

Figure 4.18: Evolution of the velocity field for PBXN-109 without reaction.

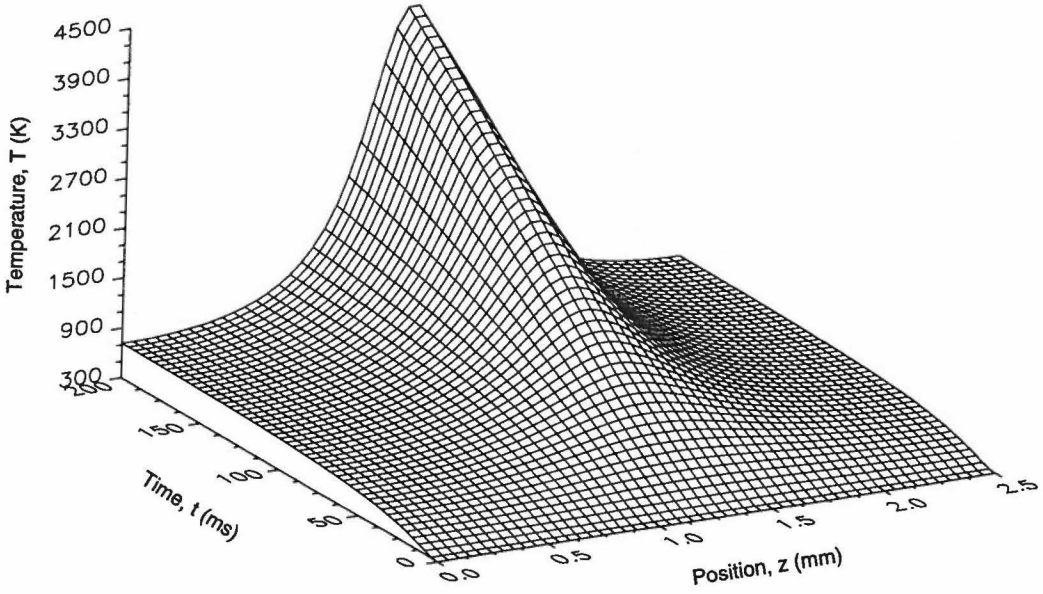

Figure 4.19: Evolution of the temperature field for PBXN-109 without reaction.

PBXN-109 simulant, as did the PBX 9501 simulant, failed experimentally by mechanisms which are not included in this model. Furthermore, it is not expected that deformation in this material can be sustained long enough to increase temperatures into the reactive range.

4.4 Numerical Simulations on Reactive Materials

Results are next presented for numerical simulations on reactive materials. The reactive parameters for PBX 9501, PBXN-109 and tritonal are included in Table 4.3. Dobratz and Crawford (1985) list maximum calculated and experimentally determined values of Q for various explosives. They also tabulate values of Z and E for various explosives, but not for any of those tested herein. For PBX 9501, Dobratz and Crawford only list the maximum calculated value of Q. For PBX 9404, a similar explosive, the experimental value is 88.5% of the maximum, hence, the Q value for PBX 9501 is chosen to be 88.5% of its maximum calculated value. Since PBX 9501 is 95% by weight HMX, the values of Z and E for HMX were used. Neither PBXN-109 nor tritonal are included in Dobratz and Crawford's handbook. Since PBXN-109 is 64% RDX, the experimentally determined value of Q and the values of A and E for RDX were used to simulate this explosive. Likewise, as tritonal is 80% TNT, the values of Q, Z, and E for TNT were used to simulate tritonal.

4.4.1 PBX 9501 With Reaction

Results are now presented for simulations of PBXN-109 with the effects of reaction included. The same parameters were used in this simulation as in the nonreactive

Material	Z (s^{-1})	Q (kJ/kg)	E (kJ/mol)	R $(J/mol \cdot K)$
PBX 9501	5.00×10^{19}	5891	220.6	8.314
PBXN-109	2.02×10^{18}	6320	197.1	8.314
Tritonal	2.51×10^{11}	4560	143.9	8.314

Table 4.3: Reactive constants used in the numerical code.

case. The effects of including reaction proved to have little effect on the results prior to initiation. The localization criterion predicted localization after 1.682 ms, a difference of only 0.3% from the nonreactive case. The temperature at the center of the specimen at this time was within 0.1% of the corresponding nonreactive temperature. As was anticipated by the nonreactive case, reaction in the reactive test did occur shortly following the onset of localization. The evolution of the velocity and temperature profiles for this material appeared very similar to those of the nonreactive case. Computation was stopped in this simulation shortly following the start of reaction, since the reaction proceeded so quickly that the time step rapidly approached zero.

As can be seen from Figure 4.20, which plots the temperature distribution up to initiation, reaction occurred prior to severe development of the temperature spike. By comparing this figure with the evolution of the reaction progress variable, Figure 4.21, it is seen how sensitive initiation is to temperature. Appreciable reaction did not begin until the reaction temperature was reached, at which time reaction quickly initiates in the localized hot spot. Bowden and Yoffe (1985) have discussed initiation in the context of localized hot spots, shear localization being only one of the mechanisms by

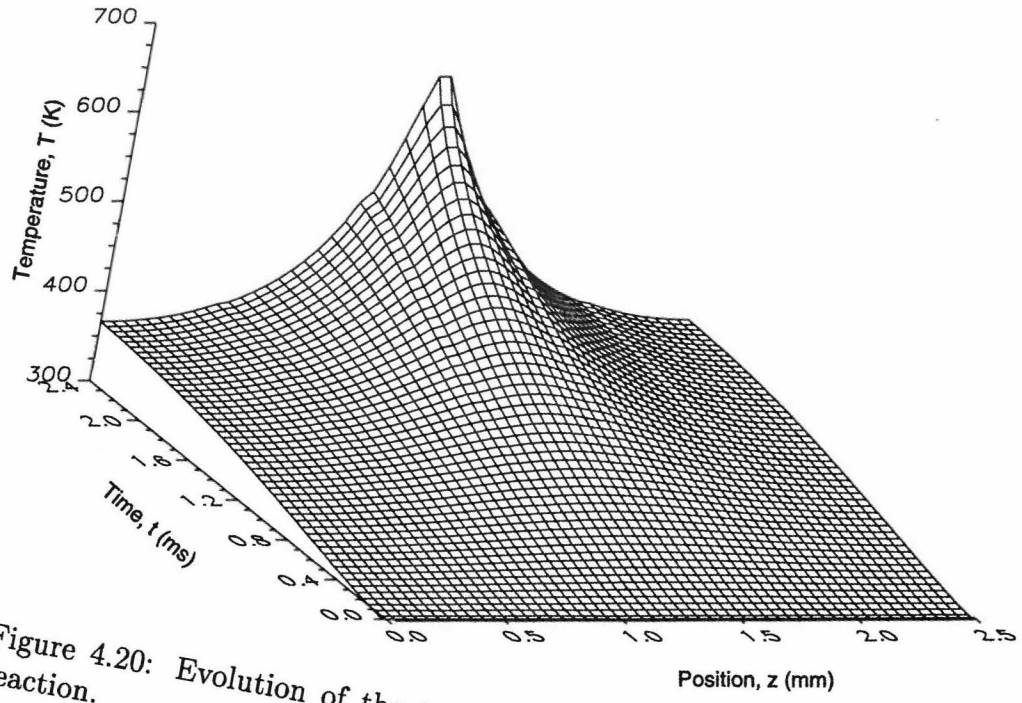

Figure 4.20: Evolution of the temperature field for PBX 9501 with reaction.

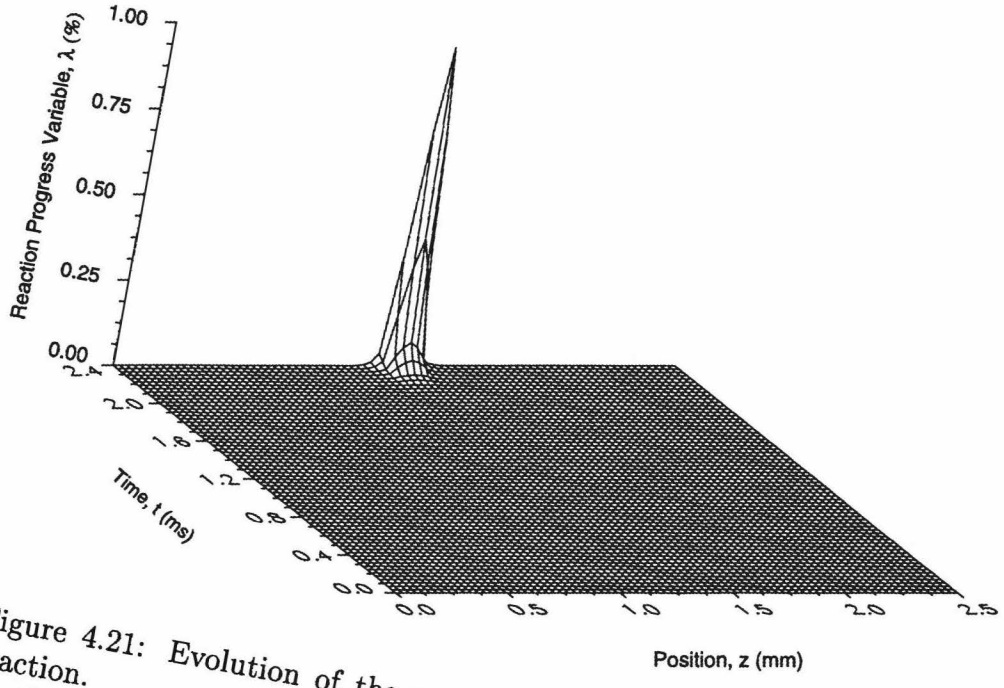

Figure 4.21: Evolution of the reaction progress for PBX 9501 with reaction.

which hot spots are generated. Also, it is observed how quickly reaction proceeds, with the reaction increasing over 10 times its value in the last 25 μs, to achieve approximately 1.0% completion at the center of the specimen. It is important, however, to state that the nominal shear strain reached at initiation is approximately 6.4, whereas the simulant failed after a shear strain of 0.2 experimentally. As stated previously, experimental observations suggested failure by other mechanisms, which are not included in this numerical code.

4.4.2 PBXN-109 With Reaction

The final material studied in this thesis is PBXN-109 with reaction effects included. Again, the same parameters were used in this simulation as in the nonreactive case. The velocity and temperature profiles, which are included in Figures 4.22 and 4.23, respectively, are plotted up to the initiation of reaction, at which time the com-

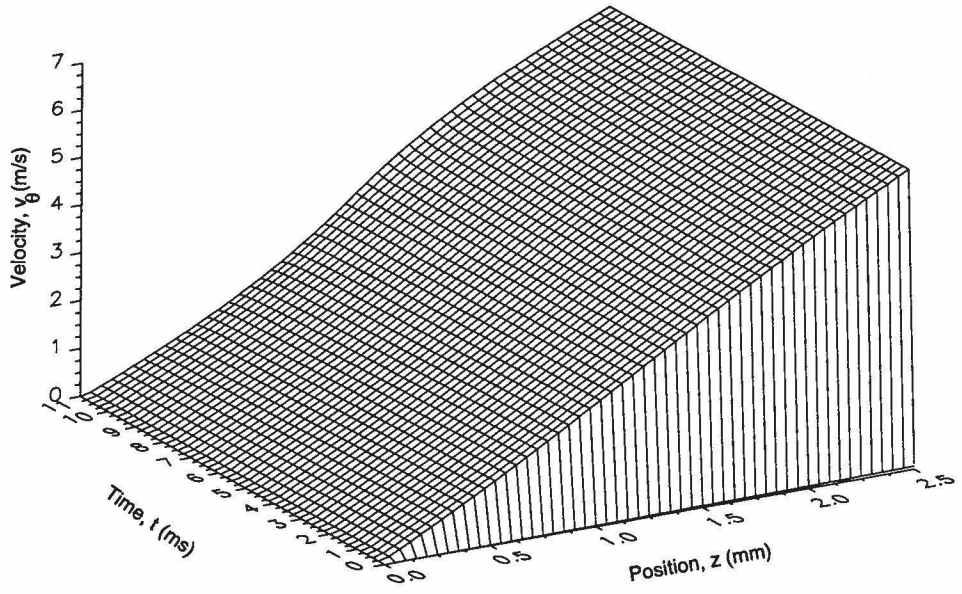

Figure 4.22: Evolution of the velocity field for PBXN-109 with reaction.

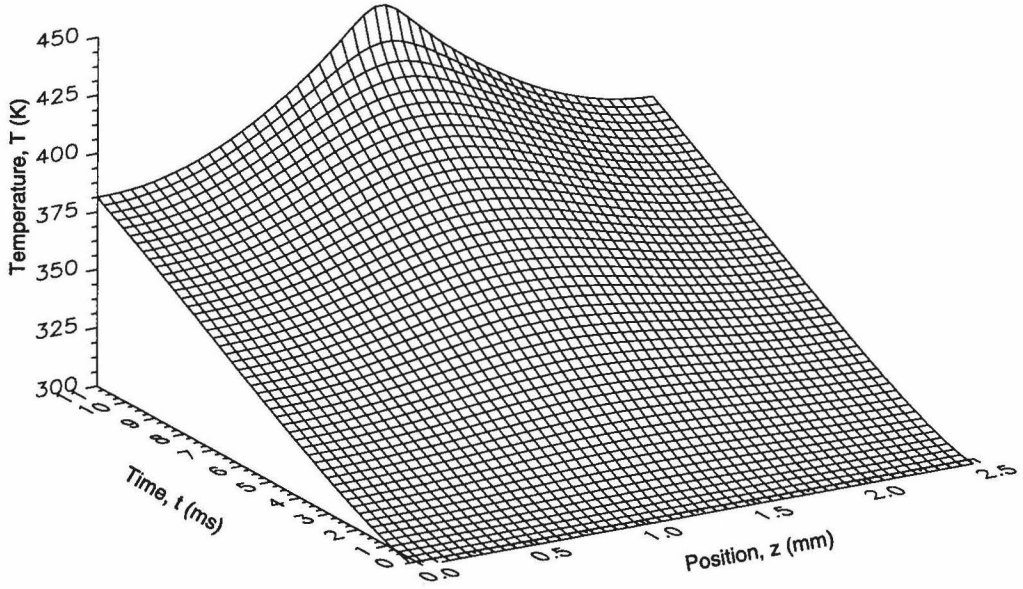

Figure 4.23: Evolution of the temperature profile for PBXN-109 with reaction.

puter code stopped computation since the time step approached zero. The velocity profile shows that no significant inhomogeneity has yet to develop, yet the temperature profile has developed an inhomogeneity. In fact, this inhomogeneity has grown enough to reach the reaction temperature. The plot of the reaction progress variable profile (Figure 4.24) reveals, as expected from the nonreactive case, that reaction has occurred prior to the onset of localization. In comparison with the results from PBX 9501, however, it is seen that reaction occurs over a much larger spatial region. This is due to the fact that the temperature is not severely localized when it reaches the initiation temperature. Computations were stopped after reaction reached approximately 1.3% completion, due to the explosive growth in reaction and consequent decrease in time step to zero. It is thus concluded that shear localization is not necessary to produce initiation. A mere inhomogeneity, if allowed to grow long enough, can result in the initiation of reaction. For this to occur, however, all other forms of

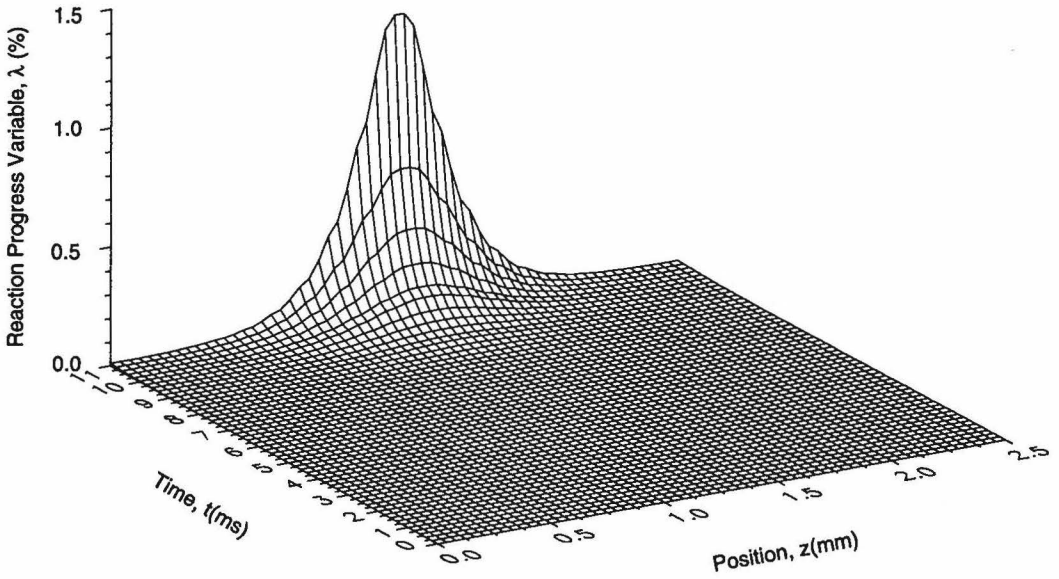

Figure 4.24: Evolution of the reaction progress variable profile for PBXN-109 with reaction.

failure would have to be suppressed. The nominal shear strain reached at initiation in this simulation, was 26.7, far in excess of the experimentally determined nominal shear strain of 1.5, which was reached at failure. As was the case in the simulation on PBX 9501, it is determined that the current analytical method is insufficient for modeling failure in PBXN-109.

4.5 Nondimensional Analysis

The results of the previous sections have demonstrated that under the current geometry, the explosives studied in this thesis do not appear to be susceptible to shear localization or thermal initiation. In this section, a study of the nondimensional parameters is performed in order to determine their influence on shear localization and initiation. Table 4.4 lists the values of the nondimensional parameters found in the simulations performed in the previous sections. For simulations #5 and #6,

the reactive constant are reported for the corresponding simulations in which reaction was included. Appropriate ranges in these parameters can be determined from this table. These parameters can then be varied, with comparisons made based on the nondimensional shear localization onset time, t^*_{loc}, predicted by the localization criterion, Equation (3.33). For these comparisons, simulations are based on the parameters for PBX 9501, due to its susceptibility to localization. The value of t^*_{loc} in the unperturbed simulation on PBX 9501, as determined in Section 4.4.1, was 4.710.

Simulation Number	Material	$\hat{\alpha}$	$\hat{\alpha}Ec$	Pe	$\hat{Q}$	$\hat{Z}$	$\hat{E}$
1	S-7 TS	11476.69	1.135	866.43	-	0	-
2	1018 CRS	4157.30	0.392	677.08	-	0	-
3	S-7 TS	1047.93	1.152	2888.09	-	0	-
4	S-7 TS	7093.20	1.135	1401.86	-	0	-
5	PBX 9501	470.19	0.068	80145.37	17.28	1.79×10^{16}	88.80
6	PBXN-109	57.75	0.00601	316135.82	16.83	8.08×10^{14}	58.08

Table 4.4: Nondimensional parameter values for the simulations in Sections 4.2-4.4.

From a comparison of the nondimensional stress constant values, $\hat{\alpha}$, listed in Table 4.4, it is determined that values of $\hat{\alpha}$ for the steels simulated are as much as 24 times as large as the value for the simulation on PBX 9501. A simulation was thus performed by increasing the value of $\hat{\alpha}$ for PBX 9501 by 10 times, while holding the parameter $\hat{\alpha}EC$ constant. It was found that this simulation had little effect on t^*_{loc}, with an increase of 0.1% to a value of 4.713, as compared to the unperturbed

value. To further study the effect of $\hat{\alpha}$ on localization, its value was then decreased by a factor of 10 from its unperturbed value, with $\hat{\alpha}Ec$ again held constant. This simulation also yielded little change in the localization onset time, with a decrease of 0.1% to $t^*_{loc} = 4.707$.

Next, simulations were performed by varying the value of the parameter $\hat{\alpha}Ec$. In comparing the values for this parameter reported in Table 4.4, it is determined that values for the steels simulated vary as much as 17 times greater than the value for PBX 9501. By increasing the value of $\hat{\alpha}Ec$ by a factor of 10, it is found that this parameter has a significant effect on the onset time, with the value decreasing by a factor of 5.5 to $t^*_{loc} = 0.857$. A simulation performed with $\hat{\alpha}Ec$ decreased by a factor of 10 also had a significant effect on the onset time, with its value increased by a factor of 4.67 to $t^*_{loc} = 26.703$.

Simulations were also performed by varying the Peclet number, Pe. It is determined from Table 4.4 that the values of Pe for the steels simulated previously are significantly less than that for the PBX 9501 simulation, with values as much as 118 times smaller. By decreasing the value of Pe for PBX 9501 by a 100 times, as compared to the unperturbed value, t^*_{loc} was delayed by a mere 1.7%, to a value of 4.791. An infinite value in this parameter would remove all the effects of conduction and hence render deformation adiabatic. By increasing Pe by a factor of 10^4, t^*_{loc} increased by only 0.06% to a value of 4.707. As the value of Pe is even greater for PBXN-109, it is surmised that deformation in solid explosives is essentially adiabatic. However, an explosive with a significantly larger value of Pe could negate this conclusion.

In order to determine the effect of the ratio of specific heats, $\hat{c}$, it was first desired to determine an appropriate range of values. In their study, Chou *et al.* (1991) used a $\hat{c}$ value of 2.07 for PBX-9404. It was thus decided to vary the current value of 1.0 by a factor of two. These variations proved to have little effect on the nondimensional onset time, with an increase in $\hat{c}$ by a factor of two resulting in a decrease in the onset time by 0.1%, and a decrease in $\hat{c}$ by a factor of two resulting in an increase in the onset time by 0.1%. In addition, changes in the temperature and reaction progress variable after $t^* = 6.25$ were studied, with less than 0.01% change in temperature and 0.3% change in λ. It is not surprising that $\hat{c}$ had such a little effect on the results, since computations are stopped prior to significant reaction. Without significant reaction, only a small portion of the material will have been converted to product and hence there will be little overall change in the specific heat. If computations were carried past the point of initiation, changes in $\hat{c}$ could produce significant differences in the results.

Next, the material parameters, η, μ, and ν are varied in order to determine their effect on shear localization and initiation. To determine the effect of the strain hardening parameter, η, the values in Table 4.1 were referenced in order to determine a realistic range to vary η. To reduce the strain hardening to that of steels, the value of η for PBX-9501 was decreased by a factor of ten to 0.032. This variation resulted in a decrease in t^*_{loc} to a value of 1.311, 3.6 times less than the unperturbed value. To compare with PBXN-109, the value of η was then increased by a factor of two to 0.64. This simulation decreased t^*_{loc} enough for initiation to occur prior to localization. Initiation thus occurred at $t^* = 7.27$. When the effects of reaction were

neglected, t^*_{loc} was determined to be 7.656, 1.6 times greater than the unperturbed value. In comparison, a decrease in η by a factor of two to 0.16 resulted in an onset time of 4.056, 1.16 times less than the unperturbed value. It is thus determined that the strain hardening parameter has a significant effect on the time necessary to reach shear localization.

The strain rate hardening parameter, μ, was then varied, with appropriate values determined from Table 4.1. For comparison with steels, μ was first decreased by a factor of four to 0.02, resulting in $t^*_{loc} = 2.954$, 1.6 times less than the unperturbed simulation. To compare with PBXN-109, μ was then increased by a factor of four to 0.32. As occurred when η was increased, this simulation resulted in initiation occurring prior to the onset of localization, with initiation occurring at $t^* = 11.16$. When reaction effects were excluded, results were very similar to those obtained in the simulation of PBNX-109 without reaction, Section 4.3.4. It was found that, although the localization criterion predicted $t^*_{loc} = 143.109$, shear localization failed to occur, as the effects of strain and strain rate hardening had essentially balanced thermal softening. A summary of the effect of the previous six parameters on the localization onset time is included in Figure 4.25.

Next, the thermal softening parameter, ν, was varied in order to determine its effect on localization and initiation. Through a comparison of the values listed in Table 4.1, it was decided to decrease ν by a factor of four to -0.345, in order to reduce its value to that of steels. By decreasing the rate of thermal softening, initiation occurred prior to reaching localization, with reaction initiating at $t^* = 9.075$. When

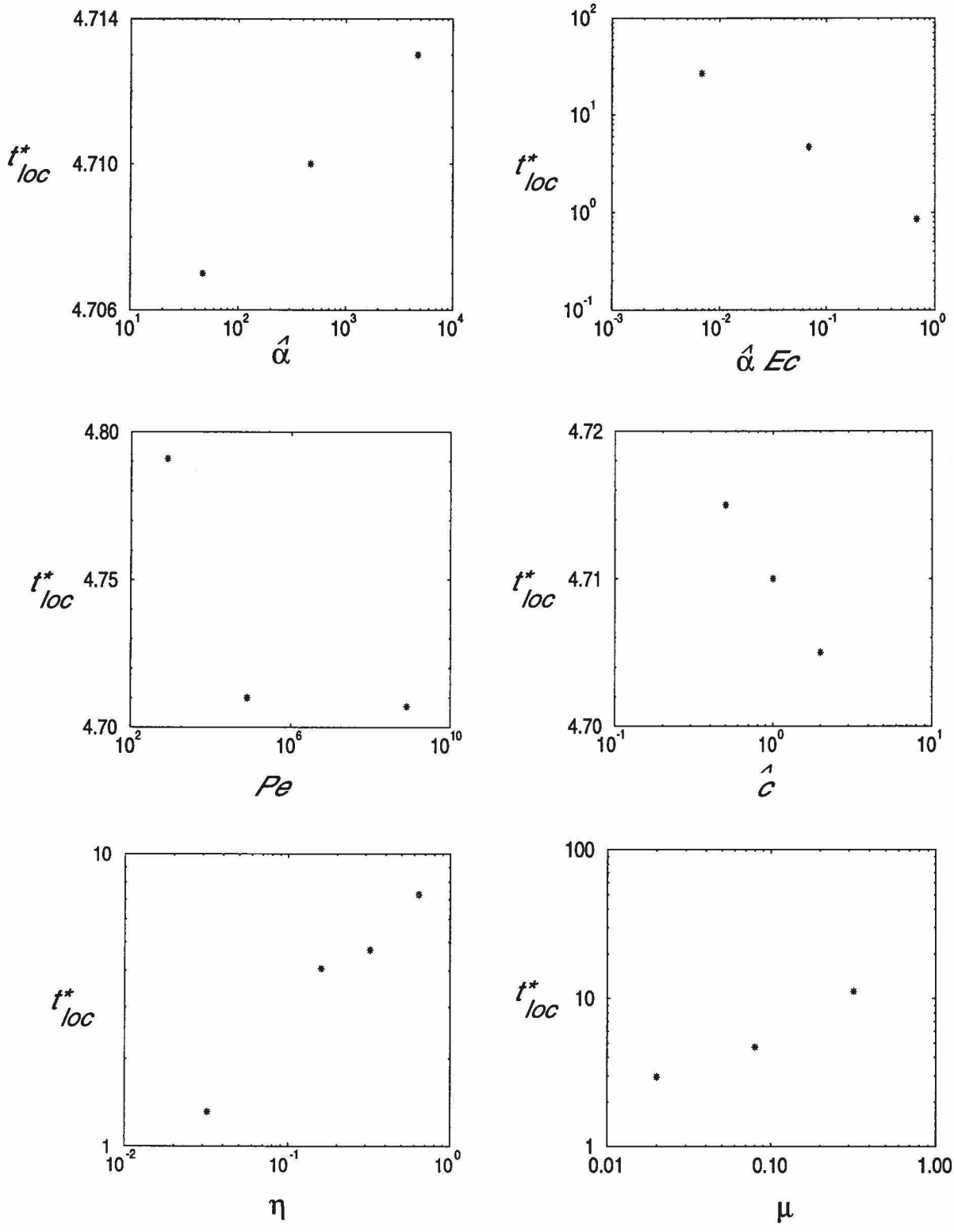

Figure 4.25: Summary of the effects of certain nondimensional parameters on the localization onset time.

the effects of reaction were excluded, it was found that the onset in shear localization was never reached–thermal softening never overpowered strain and strain rate hardening.

It is also desired to determine the effect of the nondimensional reactive parameters on localization and initiation. From an analysis of the reactive parameters for various explosives tabulated in Dobratz and Crawford (1985), it was determined that realistic values of the nondimensional heat of reaction, $\hat{Q}$, range from a maximum near the value for PBX 9501 and a minimum about two times less. Simulations on PBX 9501 with $\hat{Q}$ decreased by a factor of two result in $t^*_{loc} = 4.701$, only 0.2% less than the unperturbed case. For further study, $\hat{Q}$ was increased by a factor of two, resulting in $t^*_{loc} = 4.713$, an increase of a mere 0.06% from the unperturbed value. In addition, it was determined that, at $t^* = 6.25$, these variations in $\hat{Q}$ produced less than 0.2% variation in the temperature at the center of the shear band, and less than 4% variation in the corresponding value of the reaction progress variable. Changes in the initiation time were also negligible. It is thus concluded that realistic values of $\hat{Q}$ have little effect on the localization onset time and the proceeding collapse of deformation, or on initiation. It is expected, however, that larger values of $\hat{Q}$ would increase the growth in temperature during reaction, but since the machine precision is insufficient to model sufficient reaction growth, this supposition has not been validated.

In studying the effects of the nondimensional activation energy, $\hat{E}$, it was determined that this parameter has a significant effect on the results. From Dobratz and Crawford (1985), it was determined that realistic values of $\hat{E}$ range from a maximum

near the value for PBX 9501 and a minimum about two times less. When a simulation was performed with $\hat{E}$ decreased by a factor of two, it was found that initiation occurred prior to localization, at $t^* = 0.72$. From a calculation at $t^* = 0.70$, it was determined that the temperature had only increased by 7.3% as compared to the unperturbed value. The reaction progress variable, however, had increased from the unperturbed value of 1.84×10^{-22} to a value of 4.3×10^{-3}. It is thus seen that $\hat{E}$ has a drastic effect in the initiation of reaction, but little effect on other characteristics of the solution.

Next, the nondimensional kinetic rate constant, $\hat{Z}$, is studied. From Dobratz and Crawford (1985) it is determined that realistic values of $\hat{Z}$ range from a maximum near the value for PBX 9501 and a minimum about ten orders of magnitude less. Simulations were thus performed in which $\hat{Z}$ is decreased by five and ten orders of magnitude from the unperturbed value. For each test, t^*_{loc} is increased to 4.712, an increase of only 0.2%. However, these simulations produced a significant difference in the time to reach reaction. For the case where $\hat{Z}$ is five orders of magnitude less, the nondimensional time to reaction is increased from 6.53 to 7.47, and for the case where $\hat{Z}$ is 10 orders of magnitude less, the nondimensional time to reaction is increased to 8.91. For each case, the temperature at the center of the shear band after $t^* = 6.5$ is decreased by only 3.7% from the unperturbed value. The corresponding value of the reaction progress variable, however, changes significantly. The values of the reaction progress variable for the unperturbed, five and ten order of magnitude decreases in $\hat{Z}$ are, respectively: 4.0×10^{-3}, 2.0×10^{-8}, and 2.0×10^{-13}. It is thus determined that changes in $\hat{Z}$ do not significantly affect the material behavior prior to initiation,

but have a significant effect in the time necessary to reach initiation. A summary of the effect of the previous four parameters on the localization onset time and reaction initiation time, t^*_{react}, is included in Figure 4.26.

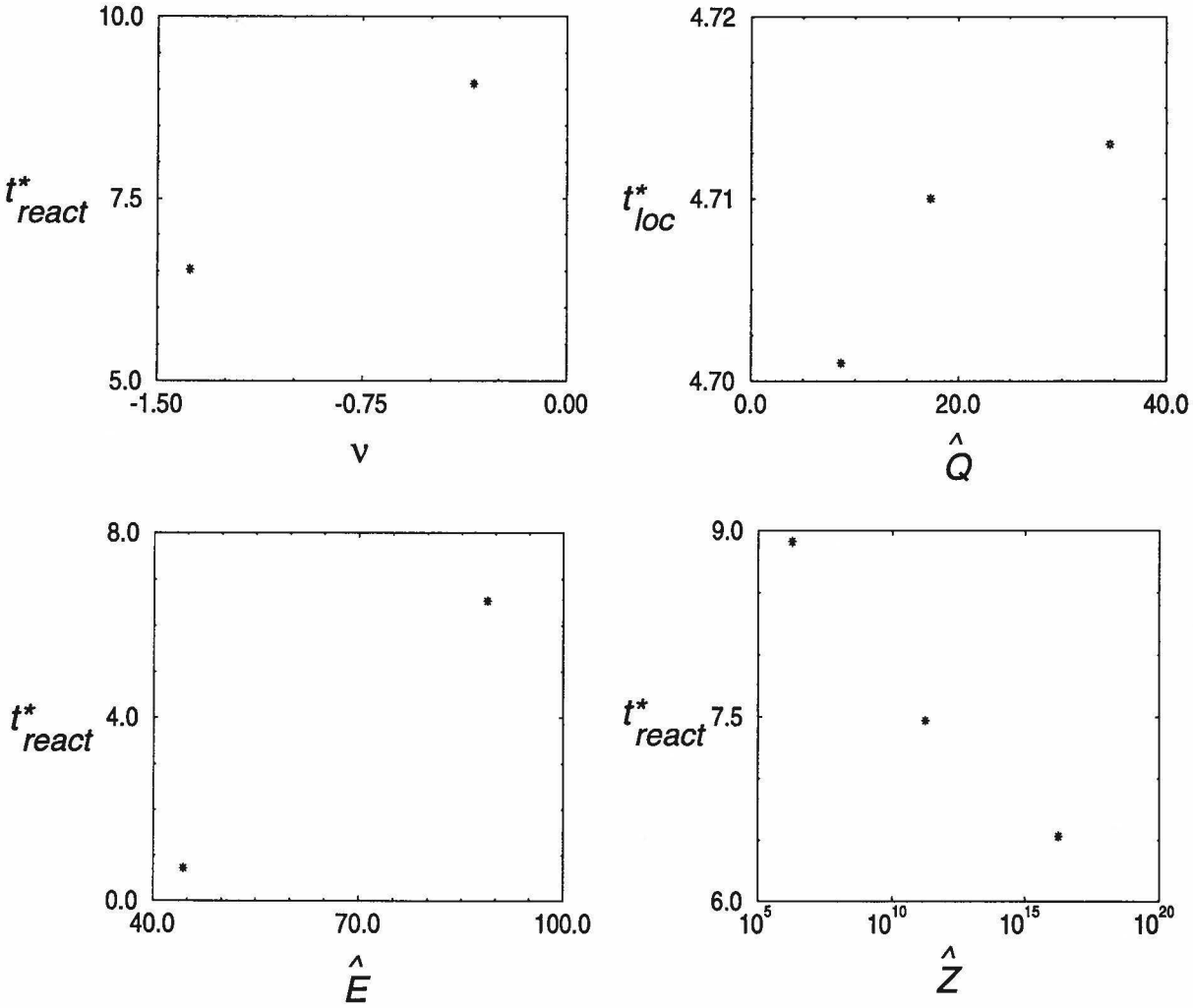

Figure 4.26: Summary of the effects of certain nondimensional parameters on the localization onset time and the reaction initiation time.

CHAPTER 5

CONCLUSIONS

The results included herein first present constitutive behavior in the form of shear stress-shear strain curves for a PBX cure cast simulant, a PBX pressed simulant, and a melt cast simulant known as Filler-E. These simulants are used to approximate the material properties of PBXN 109, PBX 9501, and tritonal, respectively. Results from these tests revealed significant dependencies of the shear stress on shear strain and shear strain rate, as compared with the corresponding dependencies of steels. Observation of the failure surface of the various explosive simulants revealed evidence of tearing, microvoid nucleation and growth, crack propagation and fragmentation. The data from these tests can be used to calibrate various constitutive laws which are used to input experimental data into analytical codes. The data from the PBX cure cast and pressed simulants has been used to calibrate the following constitutive law, proposed by Clifton, *et al.* (1984):

$$\tau = \alpha \, T^{\nu} \, \gamma^{\eta} \left| \frac{\partial \gamma}{\partial t} \right|^{\mu - 1} \frac{\partial \gamma}{\partial t} \, , \tag{5.1}$$

which models shear stress by including the effects of strain and strain rate hardening as well as thermal softening. The corresponding constitutive parameters for these materials are found in Table 4.1.

Experimental tests performed on S-7 tool steel in the condition in which it was received, as well as after heat treating it to Rockwell C-51, show that heat treating can have a drastic effect on the material properties of a specimen. By a comparison of experimental tests and numerical simulations on 1018 CRS and S-7 tool steel with results from previous researchers, it is concluded that the numerical code accurately models the deformation undergone by metal specimens in the torsional split-Hopkinson bar.

From numerical simulations on PBX 9501 without the effects of reaction, the three stage localization process observed experimentally by Marchand and Duffy (1988) was predicted, with the onset of localization predicted after a nominal shear strain of 4.63. In addition, the subsequent rise in temperature quickly exceeding the reaction temperature of the material. When the effects of reaction were included, initiation of reaction began after a nominal shear strain of 6.4. From simulations on PBXN-109 without the effects of reaction, it was determined that this material is not susceptible to localization. With the inclusion of reaction effects, however, it was determined that reaction could occur without localization. Due to a mere growth in the inhomogeneous temperature field, reaction initiating after a nominal shear strain of 26.7.

Since localization is assumed to be followed by failure or initiation, numerical results agreed with experimental results in predicting that PBX 9501 would fail at a lower strain than PBXN-109. Experimentally, the corresponding simulants failed after nominal shear strains of 0.2 and 1.5, respectively. In comparison of the experimental and numerical values, however, it is seen that the experimental tests failed at significantly lower shear strains. This is not surprising, since experimental observations indicated that failure could have occurred as a result of the combined mechanisms of

microvoid nucleation and growth, crack propagation and fragmentation. These mechanisms are not included in the current analytical study and hence it is not possible for their results to be predicted.

It is, however, concluded that if these other mechanisms were suppressed, localization and/or initiation would occur in the tested materials. Chou *et al.* (1991) stated that brittle materials become more ductile under the application of hydrostatic stresses. In addition, Frey (1981) concluded that explosives under compressive stresses generate more heat when being deformed, hence decreasing the time necessary for initiation to occur. Furthermore, Chou *et al.* concluded that localization becomes significant in covered explosives. Finally, Dodd and Atkins (1983) and Osakada *et al.* (1977) concluded that increased hydrostatic stresses tended to decrease microvoid nucleation. The explosives in deep earth penetrators are contained and subject to an unknown amount of hydrostatic stress. Deformation under these circumstances could thus result in the suppression of failure mechanisms and hence increase the susceptibility to localization and initiation. As a result, it is desired to perform future tests under the application of hydrostatic stresses, in order to determine the subsequent effect on localization and initiation.

An analysis of the nondimensional parameters in the model was also performed in order to determine their influence on localization and initiation. It is concluded that the Peclet number, Pe, the ratio of specific heats of the reacted and unreacted material, $\hat{c}$, and the nondimensional heat of reaction, $\hat{Q}$, have little effect on the results. Since the Pe parameter is primarily influenced by the thermal conductivity, it is concluded that deformation in the tested energetic solids is essentially adiabatic.

This is an assumption commonly made by researchers in the tests of metals [Batra *et al.*, 1995], and since the thermal conductivity of the explosives tested is significantly lower than that of steels, this result is not surprising. In addition, the effect of $\hat{c}$ was not expected to be dominant in the tested regime since its influence would become significant following the initiation of reaction. This parameter, $\hat{Q}$, like $\hat{c}$, is thought to reach significance following the initiation of reaction.

As with the previously mentioned constant, changes in the nondimensional kinetic rate constant, $\hat{Z}$, proved to have little effect on the onset of localization. These changes did, however, significantly alter the time at which appreciable reaction began, with decreases in $\hat{Z}$ causing a reduction in the rate of increase of the reaction progress variable, λ. This effect is also as expected since $\hat{Z}$ determines the speed by which a reaction will progress.

It was then determined that the combination of the nondimensional stress constant and the Eckert number, $\hat{\alpha}Ec$, proved to significantly alter the results, with increases in $\hat{\alpha}Ec$ resulting in a decrease in the time necessary to reach localization. This parameter is primarily affected by the strength of the material. Hence, stronger materials are more susceptible to localization. Changes in the strain and strain rate hardening parameters, η, and μ, respectively, also proved to be significant. Increases in these parameters delayed localization, as expected. Interestingly, the effect of realistic variations in the strain rate hardening exponent was found to be more significant than the effect of the strain hardening exponent. This is in contrast with the results reached by Clifton *et al.* (1984) and Wright and Batra (1985), who concluded that the strain rate susceptibility plays little role on the critical strain at localiza-

tion. However, this discrepancy could be explained by Chou *et al.*, who stated that PBX bonded explosives are particularly sensitive to strain rate effects. The thermal softening parameter, ν, also proved to be significant, with significant decreases in its value resulting in the elimination of shear localization. Finally, increases in the nondimensional activation energy, $\hat{E}$, proved to significantly increase the susceptibility to initiation. This is also expected since $\hat{E}$ essentially determines the reaction temperature.

It is thus concluded that the most important parameters in the study of shear localization for a given material are the constitutive parameters and the activation energy. In order to increase the mass, and hence momentum, of reactive devices, studies are being performed at Eglin Air Force Base on an explosive unofficially termed TUNG-5. This explosive uses tungsten as a binder for the explosive crystals. Due to its high strength, it is concluded in this thesis that such a material would be particularly susceptible to shear localization and hence reaction. This material would have the material characteristics of a metal and the reactive characteristics of an explosive. Since it is known that metals are particularly susceptible to localization, and since this thesis has shown that localization is quickly proceeded by initiation, significant precautions should be taken in the development of munitions containing this material.

For future work, several ideas are presented which may obtain more accurate results from the TSHB. First, the incident and transmission bars will be ground straight. This will reduce any bending and axial pulses, as well as decrease inhomogeneous deformation in the specimen. It is also desired to develop a better method

for aligning the bars. Currently, delrin bearings are used to support the bars. With harder bearings, the bars can be restrained from bending motion; in addition, it will be easier to determine proper alignment of the bars by observing the amount of resistance when the bars are rotated by hand. Finally, since preliminary results with new strain gages revealed up to 8% difference in transmitted strain, it is desired to apply new strain gages to the bars. Finally, it is desired to calibrate the amplifiers in order to determine a measure of their accuracy.

APPENDIX A

This appendix determines the character of the model equations. First, using Equations (3.1)-(3.12), the model equations are stated as follows:

$$\rho w \frac{\partial v_\theta}{\partial t} = \frac{\partial}{\partial z}(w\tau) \,, \tag{A.1}$$

$$\rho w \left[c_A(1-\lambda) + c_B\lambda\right] \frac{\partial T}{\partial t} = w\tau \frac{\partial v_\theta}{\partial z} - \frac{\partial}{\partial z}(wq_z) + \rho\left[Q + (c_A - c_B)T\right] \frac{\partial \lambda}{\partial t} \,, \tag{A.2}$$

$$\frac{\partial \gamma}{\partial t} = \frac{\partial v_\theta}{\partial z} \,, \tag{A.3}$$

$$\frac{\partial \lambda}{\partial t} = Z(1-\lambda)\exp\left(-\frac{E}{RT}\right) \,, \tag{A.4}$$

$$\tau = \alpha\, T^\nu\, \gamma^\eta \left(\frac{\partial \gamma}{\partial t}\right)^\mu \,, \tag{A.5}$$

$$q_z = -k\frac{\partial T}{\partial z} \,. \tag{A.6}$$

It is now necessary to state these equations into the following form:

$$\bar{A}\,\frac{\partial \tilde{y}}{\partial t} + \bar{B}\,\frac{\partial \tilde{y}}{\partial z} = \bar{C} \,, \tag{A.7}$$

where $\bar{A}$, $\bar{B}$, and $\bar{C}$ are matrices, and $\tilde{y}$ is the vector of unknowns. In order to state the equations in this form, one must first perform a local linearization on the expression $\left(\frac{\partial \gamma}{\partial t}\right)^\mu$. This is accomplished by means of a Taylor series expansion to the first order:

$$\begin{aligned} \left(\frac{\partial \gamma}{\partial t}\right)^\mu = \dot{\gamma}^\mu &\cong \dot{\gamma}_o^\mu + \mu\dot{\gamma}_o^{\mu-1}(\dot{\gamma} - \dot{\gamma}_o) \\ &\cong (1-\mu)\,\dot{\gamma}_o^\mu + \mu\dot{\gamma}_o^{\mu-1}\frac{\partial \gamma}{\partial t} \,, \end{aligned} \tag{A.8}$$

where $\dot{\gamma}_o$ is the known solution at a given point. Equation (A.8) is then inserted into Equation (A.5) and the model equations are written as follows:

$$\rho w \frac{\partial v_\theta}{\partial t} = \frac{\partial}{\partial z}(w\tau) \ , \tag{A.9}$$

$$\rho w \left[c_A (1-\lambda) + c_B \lambda\right] \frac{\partial T}{\partial t} = w\tau \frac{\partial v_\theta}{\partial z} - \frac{\partial}{\partial z}(w q_z) + \rho \left[Q + (c_A - c_B) T\right] \frac{\partial \lambda}{\partial t} \ , \tag{A.10}$$

$$\frac{\partial \gamma}{\partial t} = \frac{\partial v_\theta}{\partial z} \ , \tag{A.11}$$

$$\frac{\partial \lambda}{\partial t} = Z (1-\lambda) \exp\left(-\frac{E}{RT}\right) \ , \tag{A.12}$$

$$\tau \cong \alpha \, T^\nu \, \gamma^\eta \left[(1-\mu)\left(\dot{\gamma}^o\right)^\mu + \mu \dot{\gamma}^{o(\mu-1)} \frac{\partial \gamma}{\partial t}\right] \ , \tag{A.13}$$

$$q_z = -k \frac{\partial T}{\partial z} \ . \tag{A.14}$$

This system is then written in the form of Equation (A.7) as follows:

$$\begin{bmatrix} \rho w & 0 & 0 & 0 & 0 & 0 \\ 0 & \rho w \left[c_A (1-\lambda) + c_B \lambda\right] & 0 & -\rho \left[Q + (c_A - c_B) T\right] & 0 & 0 \\ 0 & 0 & 1 & 0 & 0 & 0 \\ 0 & 0 & 0 & 1 & 0 & 0 \\ 0 & 0 & \alpha\mu \, T^\nu \, \gamma^\eta \, \dot{\gamma}^{o(\mu-1)} & 0 & 0 & 0 \\ 0 & 0 & 0 & 0 & 0 & 0 \end{bmatrix} \begin{bmatrix} v_\theta \\ T \\ \gamma \\ \lambda \\ w\tau \\ w q_z \end{bmatrix}_t$$

$$+ \begin{bmatrix} 0 & 0 & 0 & 0 & -1 & 0 \\ -w\tau & 0 & 0 & 0 & 0 & 1 \\ -1 & 0 & 0 & 0 & 0 & 0 \\ 0 & 0 & 0 & 0 & 0 & 0 \\ 0 & 0 & 0 & 0 & 0 & 0 \\ 0 & -k & 0 & 0 & 0 & 0 \end{bmatrix} \begin{bmatrix} v_\theta \\ T \\ \gamma \\ \lambda \\ w\tau \\ w q_z \end{bmatrix}_z = \begin{bmatrix} 0 \\ 0 \\ 0 \\ Z (1-\lambda) \exp\left(-\frac{E}{RT}\right) \\ \tau - \alpha \, T^\nu \, \gamma^\eta \, (1-\mu) \left(\dot{\gamma}^o\right)^\mu \\ q_z \end{bmatrix} \tag{A.15}$$

Whitham (1974) shows that the characteristics of such systems are found from the eigenvalues, ζ, of the characteristic determinant, $\left|\bar{A}+\zeta\bar{B}\right|=0$. For this system, the determinant is stated below:

$$\begin{vmatrix} \rho w & 0 & 0 & 0 & -\zeta & 0 \\ -\zeta w\tau & \rho w\left[c_A\left(1-\lambda\right)+c_B\lambda\right] & 0 & -\rho\left[Q+\left(c_A-c_B\right)T\right] & 0 & \zeta \\ -\zeta & 0 & 1 & 0 & 0 & 0 \\ 0 & 0 & 0 & 1 & 0 & 0 \\ 0 & 0 & \alpha\mu\, T^{\nu}\,\gamma^{\eta}\,\dot{\gamma}^{o(\mu-1)} & 0 & 0 & 0 \\ 0 & -\zeta k & 0 & 0 & 0 & 0 \end{vmatrix}$$

$$= -k\;\alpha\;\mu\;T^{\nu}\;\gamma^{\eta}\;\dot{\gamma}^{o(\mu-1)}\zeta^{4}=0\;. \qquad \text{(A.16)}$$

If all eigenvalues are real, the system is hyperbolic; if any eigenvalue is zero, the system is parabolic; and if any eigenvalue is imaginary, the system is elliptic. From Equation (A.16), it is easily seen that all the eigenvalues are zero, which is indicative of a parabolic system.

BIBLIOGRAPHY

[1] L. Anand, K. H. Kim and T. G. Shawki (1987), "Onset of Shear Localization in Viscoplastic Solids," *J. Mech. Phys. Solids*, Vol. 35, No. 4, pp. 407-429.

[2] W. W. Baker and C. H. Yew (1966), "Strain Rate Effects in the Propagation of Torsional Plastic Waves," *J. Appl. Mech.*, Vol. 33, pp. 917-923.

[3] R. C. Batra and X. S. Jin (1994), "Analysis of Dynamic Shear Bands in Porous Thermally Softening Viscoplastic Materials," *Arch. Mech.*, Vol. 46, 1-2, pp. 13-36.

[4] R. C. Batra and C. H. Kim (1991), "The Effect of Thermal Conductivity on the Initiation, Growth, and Band Width of Adiabatic Shear Bands," *Int. J. Eng. Science*, Vol. 29, pp. 949-960.

[5] R. C. Batra and C. H. Kim (1992), "Analysis of Shear Banding in Twelve Materials," *International Journal of Plasticity*, Vol. 8, pp. 425-452.

[6] R. C. Batra, X. Zhang, and T. W. Wright (1995), "Critical Strain Ranking of 12 Materials in Deformations Involving Adiabatic Shear Bands," *Journal of Applied Mechanics*, Vol. 62, pp. 252-255.

[7] F. P. Bowden and Y. D. Yoffe (1985), *Initiation and Growth of Explosives in Liquids and Solids*, Cambridge University Press, Cambridge, Great Britain.

[8] V. Boyle, R. Frey, and O. Blake (1989), "Combined Pressure Shear Ignition of Explosives," *Ninth Symposium (International) on Detonation*, pp. 3-17.

[9] H. P. Cherukuri and T. G. Shawki (1995, a), "An Energy-Based Localization Theory: I. Basic Framework," *Int. J. of Plasticity*, Vol. 11, No. 1, pp. 15-40.

[10] H. P. Cherukuri and T. G. Shawki (1995, b), "An Energy-Based Localization Theory: II. Effects of the Diffusion, Inertia, and Dissipation Numbers," *Int. J. of Plasticity*, Vol. 11, No. 1, pp. 41-64.

[11] P. C. Chou, W. Flis, and D. Jann (1991), "Explosive Response to Unplanned Stimuli," Dyna East Corporation Technical Report DE-TR-91-15.

[12] I. G. Currie (1993), *Fundamental Mechanics of Fluids*, 2nd ed., McGraw-Hill, Inc., New York, pp. 224-228.

[13] R. J. Clifton, J. Duffy, K. A. Hartley, and T. G. Shawki (1984), "On Critical Conditions for Shear Band Formation at High Strain Rates," *Scripta Met.*, Vol. 18, pp. 443-448.

[14] L. S. Costin, E. E. Crisman, R. H. Hawley, and J. Duffy (1979), *2nd Conference on the Mechanical Properties of Materials at High Rates of Strain*, Ed. by J. Harding, The Institute of Physics, London, 90.

[15] B. M. Dobratz and P. C. Crawford (1985), *LLNL Explosives Handbook–Properties of Chemical Explosives and Explosive Simulants*, Lawrence Livermore National Labs., UCRL-52997, National Technical Information Service, DE91–006884.

[16] B. Dodd (1983), "Shear Instabilities in Blanking and Related Processes," *Metals Technology*, Vol. 10, pp. 57-60.

[17] B. Dodd and A. G. Atkins (1983), "Flow Localization in Shear Deformation of Void-Containing and Void-Free Solids," *Acta Metall.*, Vol. 31, pp 9-15.

[18] J. Duffy, J. D. Campbell, and R. H. Hawley (1971), "On the Use of a Torsional Split Hopkinson Bar to Study Rate Effects in 1100-O Aluminum," *J. Appl. Mech.*, Vol. 38, pp. 83-91.

[19] J. Duffy and Y. C. Chi (1992), "On the measurement of local strain and temperature during the formation of adiabatic shear bands," *Materials Science and Engineering*, A157, pp. 195-210.

[20] W. Fickett and W. C. Davis (1979), *Detonation*, University of California Press, Berkeley, CA.

[21] J. E. Field, G. M. Swallowe and S. N. Heavens (1982), "Ignition Mechanisms of Explosives during Mechanical Deformation," *Proc. R. Soc. Lond.* A 382, pp. 231-244.

[22] P. S. Follansbee (1985), "The Hopkinson Bar, High Strain Rate Compression Testing," in "High Strain Rate Testing, Mechanical Testing," *Metal Hand Book*, American Society for Metals, Vol. 8, Edition 9, pp. 198-203.

[23] R. B. Frey (1981), "The Initiation of Explosive Charges by Rapid Shear," *Seventh Symposium (International) on Detonation*, Naval Surface Weapons Center, Annapolis, MD, pp. 36-42.

[24] R. B. Frey (1985), in *Eighth Symposium (International) on Detonation*, Naval Surface Weapons Center, Albuquerque, NM, pp. 68-80.

[25] J. H. Giovanola (1988, a), "Adiabatic Shear Banding Under Pure Shear Loading. Part I: Direct Observation of Strain Localization and Energy Dissipation Measurements," *Mechanics of Materials*, Vol. 7, pp. 59-71.

[26] J. H. Giovanola (1988, b), "Adiabatic Shear Banding Under Pure Shear Loading. Part II: Fractographic and Metallographic Observations," *Mechanics of Materials*, Vol. 7, pp. 73-87.

[27] D. E. Grady (1991), "Dynamics of Adiabatic Shear," *Journal de Physique IV*, Coll. C3, suppl. to Journal de Physique III, Vol. 1, p. C3-653.

[28] D. E. Grady (1992), "Properties of and Adiabatic Shear-Band Process Zone," *J. Mech. Phys. Solids*, Vol. 40, No. 6, pp. 1197-1215.

[29] D. E. Grady (1994), "Dissipation in Adiabatic Shear Bands," *Mechanics of Materials*, Vol. 17, No. 2-3, pp. 289-293.

[30] T. N. Hall and J. R. Holden (1988), *Navy Explosives Handbook. Explosion Effects and Properties–Part III. Properties of Explosives and Explosive Compositions.*, Naval Surface Warfare Center, NSWC MP 88-116, Defense Technical Information Center, AD-B138 762.

[31] J. Harding, E. D. Wood, and J. D. Campbell (1960), "Tensile Testing of Material at Impact Rate of Strain," *J. Mech. Eng. Sci.*, Vol. 2, p. 88.

[32] K. A. Hartley and J. Duffy (1985), "Introduction, High Strain Rate Shear Testing" in "High Strain Rate Testing, Mechanical Testing" *Metal Hand Book*, American Society for Metals, Vol. 8, Edition 9, p. 215.

[33] K. A. Hartley, J. Duffy, and R. H. Hawley (1985), "The Torsional Kolsky (Split-Hopkinson) Bar, High Strain Rate Shear Testing" in "High Strain Rate Testing, Mechanical Testing," *Metal Hand Book*, American Society for Metals, Vol. 8, Edition 9, pp. 218-230.

[34] K. A. Hartley, J. Duffy, and R. H. Hawley (1987), "Measurement of the Temperature Profile During Shear Band Formation in Steels Deforming at High Strain Rates," *J. Mech. Phys. Solids*, Vol. 35, No. 3, pp. 283-301.

[35] A. C. Hindmarsh (1983), "ODEPACK, A Systematized Collection of ODE Solvers," *Scientific Computing*, R. S. Stepleman *et al.*, Eds., IMACS/North-Holland Publishing Company, Amsterdam, pp. 55-64.

[36] W. Johnson (1987), "Henri Tresca as the Originator of Adiabatic Heat Lines," *Int. J. Mech. Sci.*, Vol. 29, pp. 301-310.

[37] G. R. Johnson and W. H. Cook (1983), "A Constitutive Model and Data for Metals Subjected to Large Strains, High Strain Rates and High Temperatures," *Proc. 7th Int. Symp. Ballistics*, The Hague, The Netherlands, pp. 541-548.

[38] J. Kang, P. B. Butler, and M. R. Baer (1992), "A Thermomechanical Analysis of Hot Spot Formation in Condensed-Phase, Energetic Materials," *Combustion and Flame*, Vol. 89, pp. 117-139.

[39] H. Kobayashi and B. Dodd (1989), "A Numerical Analysis for the Formation of Adiabatic Shear Bands Including Void Nucleation and Growth," *Int. J. Impact Engng.*, Vol. 8. No. 1, pp. 1-13.

[40] H. Kolsky (1949), "An Investigation of the Mechanical Properties of Materials at Very High Rates of Loading," *Proc. Phys. Soc. London*, Vol. 62-B, pp. 676-700.

[41] H. Kolsky (1953), *Stress Waves in Solids*, Oxford University Press, London.

[42] J. L. Lewis and J. D. Campbell (1972), "The Development and Use of a Torsional Hopkinson Bar Apparatus," *Exp. Mech.*, Vol. 12, No. 11, pp. 520-524.

[43] U. S. Lindholm (1964), "Some Experiments with the Split Hopkinson Pressure Bar," *J. Mech. Phys. Solids*, Vol. 12, p. 317.

[44] J. Lubliner (1990), *Plasticity Theory*, Macmillan Publishing Co., New York, pp. 69-99.

[45] A. Marchand and J. Duffy (1988), "An Experimental Study of the Formation Process of Adiabatic Shear Bands in a Structural Steel," *J. Mech. Phys. Sol.*, Vol. 36, No. 3, pp. 251-283.

[46] K. G. McConnell and W. F. Riley (1993), "Strain-Gage Instrumentation and Data Analysis," in *Handbook on Experimental Mechanics*, A. S. Kobayashi, Ed., 2nd edition, VCH Publishers, Inc., New York, NY, pp. 79-117.

[47] L. W. Meyer (1992), "Constitutive Equations at High Strain Rates," in *Shock-Wave and High-Strain-Rate Phenomena in Materials*, M. A. Meyers, L. E. Murr, and K. P. Staudhammer, Eds., Marcel Dekker, Inc., New York, NY, pp. 49-68.

[48] M. A. Meyers (1994), *Dynamic Behavior of Materials*, John Wiley & Sons, Inc., New York, NY.

[49] M. A. Meyers, L. E. Murr, K. P. Staudhammer (1992), *Shock-Wave and High-Strain-Rate Phenomena in Materials*, Marcel Dekker, Inc., New York, NY.

[50] T. Nicholas and S. J. Bless (1985), "Split-Hopkinson Bar in Tension, High Strain Rate Tension Testing," in "High Strain Rate Testing, Mechanical Testing," *Metal Hand Book*, American Society for Metals, Vol. 8, p.212.

[51] K. Osakada, A. Watadani and H. Sekiguchi (1977), *Bull. J.S.M.E.*, Vol. 20, p. 1557.

[52] E. P. Popov (1990), *Engineering Mechanics of Solids*, Prentice-Hall, Inc., Englewood Cliffs, NJ, pp. 175-217.

[53] A. M. Rajendran (1992), "High Strain Rate Behavior of Metals, Ceramics and Concrete," Report # WL-TR-92-4006, Wright Patterson Air Force Base.

[54] H. C. Rogers (1979), "Adiabatic Plastic Deformation," *Ann. Rev. Mater. Sci.*, Vol. 9, pp. 283-311.

[55] T. G. Shawki (1994, a), "An Energy Criterion for the Onset of Shear Localization in Thermal Viscoplastic Materials, Part I: Necessary and Sufficient Initiation Conditions," *J. of Applied Mechanics*, Vol. 61, pp. 530-537.

[56] T. G. Shawki (1994, b), "An Energy Criterion for the Onset of Shear Localization in Thermal Viscoplastic Materials, Part II: Applications and Implications," *J. of Applied Mechanics*, Vol. 61, pp. 538-547.

[57] T. Weerasooriya (1990), "The MTL Torsional Split-Hopkinson Bar," U. S. Army Materials Technology Laboratory Report MTL TR 90-27.

[58] G. B. Whitham (1974), *Linear and Nonlinear Waves*, John Wiley & Sons, Inc., New York, NY.

[59] T. W. Wright (1987), "Steady Shearing in a Viscoplastic Solid," *J. Mech. Phys. Solids*, Vol. 35, No. 3, pp. 269-282.

[60] T. W. Wright (1990), "Approximate Analysis for the Formation of Adiabatic Shear Bands," *J. Mech. Phys. Solids*, Vol. 38, No. 4, pp. 515-530.

[61] T. W. Wright (1994), "Toward a Defect Invariant Basis for Susceptibility to Adiabatic Shear Bands," *Mechanics of Materials*, Vol. 17, pp. 215-222.

[62] T. W. Wright and R. C. Batra (1985), "Further Results on the Initiation and Growth of Adiabatic Shear Bands at High Strain Rates," *Journal de Physique*, Coll. C5, suppl. to no. 8, p. C5-323.

[63] T. W. Wright and J. W. Walter (1987), "On Stress Collapse in Adiabatic Shear Bands," *J. Mech. Phys. Solids*, Vol. 35, pp. 701-720.

[64] C. Zener and J. F. Hollomon (1944), "Effect of Strain Rate upon Plastic Flow of Steel," *Journal of Applied Physics*, Vol. 15, pp. 22-32.